ISTANBUL TECHNICAL UNIVERSITY ★ GRADUATE SCHOOL

FROM MEDIA-BASED MODULATION TO RECONFIGURABLE INTELLIGENT SURFACES: NOVEL INDEX MODULATION SOLUTIONS

Ph.D. THESIS

Zehra YİĞİT

Department of Electronics and Communication Engineering

Telecommunication Engineering Programme

NOVEMBER 2022

ISTANBUL TECHNICAL UNIVERSITY ★ GRADUATE SCHOOL

FROM MEDIA-BASED MODULATION TO RECONFIGURABLE INTELLIGENT SURFACES: NOVEL INDEX MODULATION SOLUTIONS

Ph.D. THESIS

Zehra YİĞİT
(504172313)

Department of Electronics and Communication Engineering

Telecommunication Engineering Programme

Thesis Advisor: Prof. Dr. İbrahim ALTUNBAŞ
Thesis Co-Advisor: Assoc. Prof. Dr. Ertuğrul BAŞAR

NOVEMBER 2022

İSTANBUL TEKNİK ÜNİVERSİTESİ ★ LİSANSÜSTÜ EĞİTİM ENSTİTÜSÜ

ORTAM-TABANLI MODÜLASYON'DAN UYARLANABİLİR AKILLI YÜZEYLERE: ÖZGÜN İNDİS MODÜLASYON ÇÖZÜMLERİ

DOKTORA TEZİ

Zehra YİĞİT
(504172313)

Elektronik ve Haberleşme Mühendisliği Anabilim Dalı

Telekomünikasyon Mühendisliği Programı

Tez Danışmanı: Prof. Dr. İbrahim ALTUNBAŞ
Eş Danışman: Doç. Dr. Ertuğrul BAŞAR

KASIM 2022

Zehra YİĞİT, a Ph.D. student of ITU Graduate School student ID 504172313, successfully defended the dissertation entitled "FROM MEDIA-BASED MODULATION TO RECONFIGURABLE INTELLIGENT SURFACES: NOVEL INDEX MODULATION SOLUTIONS", which she prepared after fulfilling the requirements specified in the associated legislations, before the jury whose signatures are below.

Thesis Advisor :	**Prof. Dr. İbrahim ALTUNBAŞ** Istanbul Technical University	.....
Co-advisor :	**Assoc. Prof. Dr. Ertuğrul BAŞAR** Koç University	.....
Jury Members :	**Prof. Dr. Güneş KARABULUT KURT** Istanbul Technical University	.....
	Prof. Dr. Ali Emre PUSANE Boğaziçi University	.....
	Prof. Dr. Hakan Ali ÇIRPAN Istanbul Technical University	.....
	Assist. Prof. Dr. Semiha TEDİK BAŞARAN Istanbul Technical University	.....
	Assoc. Prof. Dr. Eylem ERDOĞAN Istanbul Medeniyet University	.....

Date of Submission : September 30, 2022
Date of Defense : November 11, 2022

To my dear family,

FOREWORD

First and foremost, I would like to take this opportunity to express my sincere gratitude to my supervisor Assoc. Prof. Dr. Ertuğrul BAŞAR, of the Department of Electrical and Electronics Engineering, Koç University, Istanbul. I fully appreciate his continuous guidance, support, encouragement and constructive feedback in every aspect of this journey. His hard work and great enthusiasm for research have always inspired me. Also, I always feel fortunate to have had the opportunity to work with him during my master's and PhD studies. Likewise, I would like to acknowledge my co-advisor Prof. Dr. İbrahim ALTUNBAŞ for his profound experience, insightful comments and suggestions. Without their patience and great motivation, this thesis would never have been completed.

I would like also to give my sincere thanks to the rest of my thesis committee, Prof. Dr. Güneş KARABULUT KURT, Prof. Dr. Ali Emre PUSANE and Prof. Dr. Hakan Ali ÇIRPAN for their time and effort, constructive comments, words of encouragement.

Also, I would like to offer my warmest thanks to my friends and colleagues for their support and motivation in completing my thesis.

I would like to extent my special thanks to the Scientific and Technological Research Council of Turkey (TÜBİTAK) for its financial support in the projects with grant numbers 117E869 and 120E401.

Last but not least, this thesis is dedicated to my family. They deserve a special mention for their unfailing love and endless support throughout my life. It would not have been possible to complete this thesis without their care, encouragement and moral support during this journey.

September 2022

Zehra YİĞİT
(Research Assistant)

TABLE OF CONTENTS

Page

ABBREVIATIONS

ABEP	: Average bit error probability
AF	: Amplify-and-forward
AoA	: Angle of arrival
AoD	: Angle of departure
AS	: Angular spread
ASK	: Amplitude-shift keying
AWGN	: Additive white Gaussian noise
BER	: Bit error rate
bps	: Bits per second
CPEP	: Conditional pairwise error probability
CSI	: Channel state information
CSTBC	: Circular space-time block codes
dB	: Decibel
DS	: Delay spread
eMBB	: Enhanced mobile broadband
HRM	: Hybrid reflection modulation
i.i.d.	: Independent and identically distributed
IM	: Index modulation
IMT-Advanced	: International Mobile Telecommunications-Advanced
InH	: Indoor hotspot
IoT	: Internet-of-things
LOS	: Line-of-sight
LTE	: Long-Term Evolution
M2M	: Machine-to-machine
MBM	: Media-based modulation
MGF	: Moment generating function
MIMO	: Multiple-input multiple-output
ML	: Maximum likelihood
mMTC	: Massive machine-type communications
mmWave	: Millimeter-wave
NLOS	: Non-line-of-sight
QAM	: Quadrature amplitude modulation
QCQP	: Quadratically-constrained quadratic programming
PEP	: Pairwise error probability
PSK	: Phase-shift keying
RA	: Reconfigurable antenna
RF	: Radio frequency
RIS	: Reconfigurable intelligent surface
RIS-R	: RIS-to-receiver
RM	: Reflection modulation

SDR : Semi-definite relaxation
SF : Shadowing fading
SINR : Signal-to-interference-plus-noise ratio
SISO : Single-input single-output
SM : Spatial modulation
SNR : Signal-to-noise ratio
SSK : Space-shift keying
STBC : Space-time block codes
THz : Terahertz
T-R : Transmitter-to-receiver
T-RIS : Transmitter-to-RIS
UMa : Urban macro
UMi : Urban micro
ULA : Uniform linear array
URLLC : Ultra-reliable low-latency communications
ZF : Zero-forcing

LIST OF TABLES

Page

LIST OF FIGURES

Page

FROM MEDIA-BASED MODULATION TO RECONFIGURABLE INTELLIGENT SURFACES: NOVEL INDEX MODULATION SOLUTIONS

SUMMARY

According to the Cisco Annual Internet Report, by 2023, 5G speeds are expected to reach 575 megabits per second (Mbps), 13 times faster than the speed of average mobile connections. It is also estimated that more than 10 percent of the 13.1 billion mobile devices/connections will be 5G-enabled and 50 percent of global devices will support machine-to-machine (M2M) connectivity. These advancement towards future communication networks has led to develop enabling technologies that are defined in three different use cases: enhanced mobile broadband (eMBB), massive machine-type communication (mMTC) and ultra-reliable low-latency communication (URLLC). In 5G and beyond networks, mMTC and URLLC technologies will enable effective wireless connectivity for massive number of machine-type devices with ultra-low-latency, at the sub-millisecond level, which exceeds the capabilities of today's technologies. On the other hand, eMBB aims to achieve high spectral efficiency values with high reliability. These demanding performance requirements drive the need for more flexible physical layer solutions rather than the existing power-hungry and hardware-complex designs. In recent years, to address these needs, researchers have envisioned novel and effective paradigms towards future wireless networks through diverse aspects: index modulation (IM), reconfigurable intelligent surfaces (RISs), internet-of-things (IoT), visible light communications, millimeter wave (mmWave) and terahertz (THz) communications, etc.

Over the past decade, there has been a growing interest towards IM-based system designs that enhance the data rate by conveying additional information bits through the building blocks of a wireless transmission network. Compared to the early designs, with their considerably lower transceiver complexity and higher energy efficiency, IM schemes have been considered as alternative solutions for 5G and beyond wireless networks.

More specifically, media-based modulation (MBM), one of the commonly encountered transmission schemes in the IM literature, embeds the information into the selection of a particular transmission path from a multitude of channel states created by integrating parasitic elements such as radio frequency (RF) mirrors and PIN diodes into the transmit antenna(s). Therefore, the corresponding receiver perceives a unique signature of the specified channel state. This peculiar manner in the transmission information that randomizes the wireless channel offers novel insights in shaping future networks.

On the other hand, in recent years, RIS-empowered communication technology, which adapts the propagation environment in a favorable manner via deploying low-cost

reflecting elements, is regarded as a revolutionary technique to build next-generation networks. Similar to the external parasitic elements in MBM, smart reflecting elements at RISs enrich the propagation environment besides, they induce proper phase shifts to manipulate the channel for improving the overall signal quality by exploiting low-cost PIN diodes or varactors. Apparently, the MBM and RIS are based on similar constructions. However, while MBM aims to transmit additional information bits, RIS, in addition, enables to increase in the overall system reliability. Therefore, due to this additive contribution, RIS can be regarded as an enhanced form of the MBM transmission technique.

In this thesis, in order to meet demanding requirements of future generation networks that aim to attain ultimate data rate, we explore the potential of the IM systems and put forward novel solutions with solid theoretical foundations from MBM to RIS-aided systems via applying to a variety of unique tools as follows.

In the first study of this thesis, exploiting the statistics of a real reconfigurable antenna (RA) in realistic International Mobile Telecommunications-Advanced (IMT-Advanced) indoor and outdoor channel conditions for the sub-6 gigahertz (GHz) spectrum, we interpret the MBM transmission principle with and without RIS cases. In this study, contrary to existing MBM schemes that consider independent and uncorrelated channel states, we aim to investigate the performance of the MBM scheme under realistic channel conditions using radiation parameters of a real RA that creates a reasonably correlated set of channel states. In that sense, we extend our implementations and introduce an open-source physical channel simulator, *SimMBM*, that enables to perform different MBM systems for varying localizations, scenarios and RA adaptations.

In a multipath environment, since each channel state constitutes a point in the MBM constellation, from the receiver point of view, the arrived signal is perceived as an independent and identically distributed (i.i.d.) Gaussian random variable, which is, according to the Shannon capacity theorem, a desired way to attain higher capacity gains. Thus, unlike conventional MIMO systems, this inherent capacity-achieving characteristic plays an important role to understand the reason behind the improved error performance of MBM schemes with the increasing number of channel state realizations. In the next two studies of this thesis, combining this unique property of MBM with the classical space-time block coding (STBC) techniques, we aim to attain further capacity improvements via achieving transmit diversity gains. In these studies, we adapt the classical Hurwitz-Radon family of matrices and the new circular matrix-based STBC design to MBM in order to achieve various orders of transmission diversity gains over a single RF chain. Moreover, through extensive analyses, we obtain the theoretical bit error rate (BER) and capacity performance of the proposed schemes, which are supported via comprehensive computer simulations.

In the subsequent study, we deploy an RIS with passive reflecting elements, which are capable of inducing plain phase shifts to assist the classical multiple-input multiple-output (MIMO) and IM-based MIMO transmission systems. In this study, in order to maximize the signal-to-noise (SNR) of the overall cascaded system, without applying computationally complex beamforming techniques, we propose a cosine similarity theorem-based low-complexity algorithm for adapting the phase shifts of the RIS reflecting elements. Moreover, a semi-analytical probabilistic approach is developed to derive the theoretical average bit error probability (ABEP) of the system.

Furthermore, the validity of the theoretical analysis is supported through extensive computer simulations.

Although a massive literature has grown up around passive RIS-aided studies, most recently, the potential of active RISs that are capable of achieving ultimate capacity gains at the expense of additional power constraints stimulates novel research domains. In that sense, we develop a novel IM scheme in which a hybrid RIS with both active and passive reflecting elements acts as a transmit information unit. In this study, according to incoming information bits, the corresponding RIS is divided into sub-groups which consist of either passive elements with simple phase shifts or active elements with adjustable amplitudes and phases in a way that each RIS realization creates a signal with clearly distinguishable magnitude. In other words, the proposed scheme constitutes a virtual amplitude shift keying (ASK) modulation. Moreover, through comprehensive theoretical analyses and computer simulations, the BER, achievable rate and energy efficiency performance of the proposed scheme are compared with existing fully passive RIS, fully active RIS and reflection modulation (RM) systems.

In the last study of this thesis, in order to simplify transceiver complexity of classical multi-user transmission schemes, we propose a new over-the-air beamforming concept that completely transfers the inter-user interference cancellation duties of the transmitter to an active RIS. In the proposed concept without resorting to any hardware-complex pre/post signal processing techniques at the transmitter and the receiver, the amplitudes and phases of the active reflecting elements at the RIS are optimized to maximize sum-rate gains of a multi-user downlink transmission system. Moreover, taking inspiration from this over-the-air beamforming concept, a new receive IM scheme that transmits additional information bits to specify the index of the effective received antenna is also proposed. Contrary to the existing receive IM system designs that conduct transmit beamforming to steer the overall information to the specified received antenna, in the proposed receive IM scheme, without applying any transmit beamforming techniques, the reflection coefficients of the active RIS are adjusted to orient the overall reflected signal in direction of the effective received antenna. In these proposed over-the-air beamforming concepts, to optimize the reflection coefficients of the active RISs, two distinct semidefinite relaxation (SDR)-based optimization problems are formulated, which can be effectively solved through the CVX convex optimization toolbox. Moreover, through comprehensive simulation results, the sum-rate and BER performance of the proposed designs are investigated.

In summary, this thesis presents novel IM-based physical layer solutions for future generation networks in various facets starting from the classical MBM to the emerging RIS-aided systems. Through this process, we resort to different approaches including STBC techniques, low-complexity algorithms, convex optimization, physical channel models, etc. Moreover, in order to demonstrate the performance of the systems, through comprehensive computer simulations, we compare our all system designs with the classical systems and their state-of-the-art competitors. Then, in order to support these results, we attempt to derive theoretical performance analyses.

ORTAM-TABANLI MODÜLASYON'DAN UYARLANABİLİR AKILLI YÜZEYLERE: ÖZGÜN İNDİS MODÜLASYON ÇÖZÜMLERİ

ÖZET

Cisco yıllık internet raporuna göre, 2023 yılı itibariyle 5G hızının ortalama mobil bağlantı hızının 13 katına çıkarak, 575 megabit/saniye (Megabits per second, Mbps)'ye ulaşması beklenmektedir. Bunun yanında, 13.1 milyar civarında olan mobil cihaz sayısının yüzde 10'unun 5G bağlantısına sahip olacağı ve küresel cihazların yüzde 50'sinin makineler arası bağlantıyı destekler düzeyde olacağı öngörülmektedir. Diğer yandan, gelecek nesil haberleşme sistemlerindeki bütün bu gelişmeler, araştırmacıları üç farklı kategoride etkili sistem tasarımları geliştirmeye yönlendirmiştir. Bunlar; gelişmiş mobil bant (enhanced mobile broadband, eMBB), geniş ölçekli makine haberleşmesi (massive machine-type communications, mMTC) ve ultra-güvenilir düşük gecikmeli haberleşme (ultra reliable low-latency communications, URLLC) olarak adlandırılmaktadır. 5G ötesi haberleşme sistemlerinde, mMTC ve URLLC tabanlı teknolojilerin milisaniye mertebesindeki çok düşük gecikmelerle, çok sayıda cihazın birbiri ile haberleşmesinin sağlanması amaçlanırken, eMBB teknolojileri ile yüksek güvenirlikli ve yüksek veri hızlı sistemlerin tasarlanması amaçlanmaktadır. Bu zorlayıcı kriterler, mevcut sistemler ile gerçeklendiğinde, çok yüksek güç tüketimi ve karmaşık donanımlar gerektireceğinden, gelecek nesil sistemler için daha esnek ve kolay uyarlanabilir sistem tasarımlarına olan ihtiyaç artmıştır. Bu amaçla, son yıllarda araştırmacılar, indis modülasyonu (index modulation, IM), uyarlanabilir akıllı yüzey (reconfigurable intelligent surface, RIS), nesnelerin interneti (internet-of-thing, IoT), görünür ışık haberleşmesi, milimetre dalga (millimeter-wave, mmWave), terahertz haberleşme gibi özgün ve etkili fiziksel katman çözümleri geliştirmektedirler.

Geçtiğimiz on yıldan beri, bir haberleşme sisteminin yapı taşlarını bilgi iletiminde kullanarak daha yüksek bant verimliliğine ulaşmayı hedefleyen IM-tabanlı sistemler, araştırmacılar tarafından büyük bir ilgi görmektedir. Klasik sistemler ile karşılaştırıldığında düşük karmaşıklıklı alıcı-verici tasarımları ve yüksek enerji verimliliği sağlayan yapıları ile IM-tabanlı sistemler, yüksek bant ve enerji verimliliği gerektiren gelecek nesil haberleşme sistemleri için alternatif çözüm yolları sunmaktadır.

IM literatüründe yaygın olarak karşımıza çıkan, ortam-tabanlı modülasyon (media-based modulation, MBM) sisteminde, verici anten(ler) üzerine radio frekans (radio frequency, RF) aynası ya da PIN diyotlar entegre edilerek, iletim kanalında, çoklu kanal durumlarının oluşması sağlanmakta ve oluşan bu çok yollu kanal üzerinden ek bilgi bitleri iletilmektedir. Böylece, alıcıda gelen bilgi bitlerine göre belirlenen kanal durum bilgisine ait işaretler ulaşmaktadır. Telsiz iletim kanalının

rastgeleşmesini sağlayan bu özgün iletim tekniği, gelecek nesil ağların şekillenmesine yönelik yeni öngörüler sunmaktadır.

5G ötesi ağlara umut verici çözümler sağlayan bir diğer yöntem ise üzerindeki düşük maliyetli yansıtıcı elemanlar ile yayılım ortamını avantajlı yönde uyarlayabilen RIS-tabanlı sistem tasarımlarıdır. MBM tekniğinde, verici anten üzerine entegre edilen parazitik elemanlar gibi, RIS'teki akıllı yansıtıcı elemanlar da saçılım ortamını zenginleştirmekte ve buna ek olarak da, yansıma, güçlendirme ve soğurma gibi işlevleriyle ile işaret kalitesini daha da iyileştirmektedirler. Bu anlamda, iletim kanalının farklı durumları üzerinden ek bilgi iletimi sağlayan MBM, RIS iletiminin özel bir durumu olarak görülmektedir.

Bu tezde, tüm bu gelişmeler göz önüne alınarak, gelecek nesil haberleşme ağları için IM-tabanlı sistemlerin potansiyeli incelenerek, MBM iletim tekniğinden RIS'e kadar geniş bir yelpazede, özgün IM sistemleri önerilmiştir.

Bu tezde, ilk olarak, vericide gerçek bir uyarlanabilir anten (reconfigurable antenna, RA)'nin ışıma parametreleri kullanılarak, 6 gigahertz (GHz)-altı iletim bandı için, gelişmiş uluslararası mobil haberleşme (International Mobile Telecommunications-Advanced, IMT-Advanced) standartlarına göre oluşturulan gerçekçi bir kanal modeli üzerinden MBM sistemi tasarlanmıştır. Bu çalışmada, literatürdeki çoklu kanal durumlarının birbirinden bağımsız ve ilişkisiz olduğu varsayılan mevcut MBM sistemlerinin aksine, gerçek bir RA'nın ışıma parametreleri kullanılarak, birbirleriyle makul düzeyde ilişkili kanal durumlarının oluştuğu gerçekçi bir iletim ortamında, MBM sistemin başarımının incelenmesi amaçlanmıştır. Daha sonra ise, yapılan analizler genişletilerek, farklı konumlandırma, iç/dış mekan iletim ortamları ve farklı RA kullanımlarına elverişli, çeşitli MBM senaryolarının uygulanabileceği açık kaynaklı bir kanal simülatörü (*SimMBM*) oluşturulmuştur.

Çok yollu bir iletim ortamında, her bir kanal durumu, MBM işaret kümesinin bir elemanına karşılık geldiğinden, alıcıya ulaşan işaret, bağımsız ve özdeş dağılmış (independent and identically distributed, i.i.d.) Gauss rastlantı değişkenleri olarak algılanmaktadır. Alıcıdaki bu rastgelelik, Shannon kapasite kuramına göre, yüksek kapasitelere ulaşmak için bir yöntem olarak görülmektedir. Bu durum, klasik MIMO iletimin aksine, klasik uzay-kaydırmalı anahtarlama (space-shift keying, SSK) ve MBM sistemlerinde, artan kanal durum sayısının hata başarımını iyileştirme sebebini ortaya koymaktadır. Bu tezdeki ilerleyen çalışmalarda, MBM'in bu avantajlı özelliğini, klasik uzay-zaman blok kodlama (space-time block coding, STBC) iletim teknikleri ile birleştirerek, MBM'e verici anten çeşitlemesi kazandırarak daha da yüksek kapasite değerlerine ulaşılabilmesini amaçlayan iki farklı MBM-tabanlı STBC tekniği geliştirilmiştir: ST-MBM ve dairesel STBC-IM (circular STBC-IM, CSTBC-IM). Bu sistemlerde, klasik SSK iletimi uzay-zaman yöntemlerinden biri olan Hurwitz-Radon matrisleri ile ve dairesel matris-tabanlı STBC teknikleri kullanılarak, tek bir RF zinciri ile çeşitli mertebeden verici çeşitlemesi kazancı sağlanmıştır. Tüm bunlara ek olarak, kapsamlı teorik analizler sonucunda, bu sistemler için bit hata oranı (bit error rate, BER) ve kapasite başarımları elde edilmiş ve bu sonuçlar, bilgisayar benzetimleri ile desteklenmiştir.

Bir sonraki çalışmada, klasik çok-girişli çok-çıkışlı (multiple-input multiple-output, MIMO) ve IM-tabanlı MIMO sistemleri desteklemek üzere, alıcı ve verici arasında, sadece yalın faz kaymaları oluşturabilen pasif RIS yansıtıcı yüzeylerin konum-

landırıldığı varsayılmıştır. Bu çalışmada, kosinüs benzerlik teoremi kullanılarak, hesaplama karmaşıklığı yüksek herhangi bir hüzmeleme tekniğine başvurmadan, RIS yansıtıcı yüzeylerinin fazları, sistemin işaret-gürültü oranını (signal-to-noise, SNR) enbüyükleyecek şekilde düzenleyen, düşük-karmaşıklıklı bir algoritma geliştirilmiştir. Bunun yanı sıra, yarı-analitik bir yolla, RIS-tabanlı MIMO ve RIS-tabanlı IM sistemler için teorik ortalama bit hata olasılığı (average bir error probability, ABEP) elde edilerek, bu sonuçlar, kapsamlı bilgisayar benzetimleri ile desteklenmiştir.

RIS-tabanlı sistemlerde, RIS yansıtıcı elemanlarının fazlarının yanı sıra, ek güç tüketimi karşılığında, genliklerinin de ayarlanabilir olması, daha da yüksek kapasite değerlerine ulaşabilmesinin önünü açmaktadır. Bu amaçla, bütün yansıtıcı yüzeyleri ek güçlendiriciler ile desteklenen bir RIS'in doğrudan bilgi iletiminde kullanıldığı, yeni bir IM tekniği geliştirilmiştir. Bu çalışmada, vericide kullanılan modülasyonsuz bir taşıyıcıyı, gelen bilgi bitlerine göre, kolaylıkla ayırt edilebilir, birbirinden farklı genlik düzeylerine sahip işaretlere dönüştürmek üzere, RIS yansıtıcı yüzeyleri, sadece fazı ayarlanabilen pasif elemanlar veya hem genliği hem fazı ayarlanabilen aktif elemanlardan oluşan alt-gruplara ayrılmaktadır. Böylece, hem aktif hem de pasif elemanlardan oluşan hibrit RIS yapısı, herhangi bir RF zincirine gerek duyulmaksızın, vericide iletilen taşıyıcı işaret ve farklı RIS kombinasyonları üzerinden, sanal bir genlik kaydırmalı anahtarlama (amplitude shift keying, ASK) modülasyon kümesi oluşturulmaktadır. Bu özgün çalışmada, kapsamlı teorik analizler ve bilgisayar benzetimleri sonucunda, önerilen sistemin mevcut pasif RIS, aktif RIS ve yansıma modülasyonu (reflection modulation, RM) sistemlerine ile BER, kapasite ve enerji verimliliği karşılaştırmaları yapılmıştır.

Son bir kaç yılda, pasif RIS-tabanlı sistem tasarımları üzerine geniş bir literatür oluşsa da, aktif RIS-tabanlı sistemlerin yüksek kapasitelere ulaştıklarına dair yapılan ilk çalışmalar, yeni araştırma alanlarının yolunu açmıştır. Bu bağlamda, bu tezde, çok kullanıcılı sistemlerde, vericinin kullanıcılar arası girişimi giderme görevini tamamen aktif RIS'e taşıyan yeni bir havadan hüzmeleme (over-the-air beamforming) tekniği önerilmektedir. Önerilen sistemde, alıcı ve verici tarafta herhangi bir karmaşık donanıma sahip işaret işleme tekniğine başvurmadan, RIS yardımıyla aşağı-yönlü iletim yapan çok kullanıcılı bir sistemin toplam-hızını (sum-rate) enbüyükleyecek şekilde, aktif yansıtıcı yüzeylerin genlik ve faz değerleri ayarlanmaktadır. Bununla birlikte, bu havadan hüzmeleme tekniğinden esinlenerek, yukarı yönde iletim yapan tek-kullanıcılı MIMO bir iletim sisteminde, mevcut alıcı antenlerden biri etkinleştirerek, bu etkin antenin indisi üzerinden ek bilgi biti ileten yeni bir alıcı IM (receive IM) tekniği geliştirilmiştir. Önerilen bu sistemde, gönderilen işareti, gelen bilgi biti ile belirlenen alıcı antene yöneltmek üzere vericide ön kodlama yapan klasik alıcı IM tekniklerinden farklı olarak, aktif yansıtıcı yüzeylerin katsayıları, gönderilen bilgiyi sadece ilgili alıcı antene yönlendirmek üzere ayarlanmaktadır. Önerilen bu iki havadan hüzmeleme tekniğinde, aktif yansıtıcı yüzeylerinin en uygun katsayılarını belirlemek için yarı-kesin rahatlatma yöntemi (semi-definite relaxation, SDR)'ne başvurarak iki farklı optimizasyon problemi oluşturulmuş ve bu problemler CVX konveks optimizasyon çözücüleri yardımı ile çözülmüştür. Bunun yanı sıra, kapsamlı bilgisayar benzetimleri sonucunda, klasik verici ön kodlama tekniklerine karşılık, önerilen havadan hüzmeleme tekniklerinin başarım üstünlüğü vurgulanmıştır.

Özetle, bu tez çalışmasında, klasik MBM'den başlanarak, güncel RIS-tabanlı araştırmaları da kapsayan geniş bir yelpazede, gelecek nesil haberleşme sistemleri

için özgün IM çözümleri önerilmektedir. Bu tez sürecince, STBC iletim tekniği, düşük karmaşıklıklı algoritmalar, optimizasyon teknikleri, fiziksel kanal modelleme gibi bir çok farklı alanda çalışmalar yapılmıştır. Önerilen sistemlerin başarımlarını incelemek üzere, bu sistemlerin klasik ve güncel iletim teknikleri ile başarım karşılaştırmaları kapsamlı bilgisayar benzetimleri ile yapılarak, bu sonuçlar, teorik analizlerle desteklenmiştir.

1. INTRODUCTION

This chapter presents the motivation and contribution of the undertaken research topics of the thesis and concludes with the organization layout and the mathematical notations considered throughout the thesis.

1.1 Motivation and Contribution

The fifth generation (5G) technology has enabled numerous new applications with diverse characteristics including low-latency, high reliability, high data rate, energy efficiency and security under three core use cases: ultra-reliable low-latency communications (uRLLC), enhanced mobile broadband (eMBB) and massive machine type communications (mMTC) [1]. While mMTC aims to provide connectivity of the massive number of devices that intermittently send or receive a small amount of data, uRLLC applications are anticipated to deal with the stringent requirements on ultra-reliability and ultra low-latency for mission-critical transmissions. On the other hand, eMBB targets extended coverage, extreme data rates and huge amount of data transfer. To address these requirements, novel physical layer solutions, such as millimeter wave (mm-Wave), terahertz (THz), massive multiple-input multiple-output (mMIMO), and Internet of things (IoT) communications, have been developed. However, since the traditional MIMO transmission fails to support higher energy-efficiency requirement of next-generation networks, the emerging concept of index modulation (IM) has regarded as a groundbreaking paradigm that offers significant potential for attaining higher data rates in a cost-efficient manner [2]. In particular, the IM technique exploits the indices of main pillars of a basic communication system, such as antennas [3, 4], antenna patterns [5], time slots [6], etc., in a clever manner to convey extra information.

Media-based modulation (MBM) is a relatively new IM concept that offers novel insights into future communication systems by generating different radiation patterns of a single reconfigurable antenna (RA) via tunable parasitic elements such as radio

frequency (RF) mirrors or PIN diodes [5]. Indeed, exploiting rich scattering properties of transmission environments, MBM creates a signal constellation from different realizations of a wireless channel itself which brings a whole new dimension to the traditional wireless networks.

One step further towards shaping beyond 5G networks is to modify the propagation environment in a customized way via deploying reconfigurable intelligent surfaces (RISs), which are considered as a potential game-changer technology to evolve future wireless networks into smart radio environments [7]. Particularly, RISs are planar metasurfaces that enable the modification of propagation environments via integrated smart programmable elements in favor of enhancing signal quality. By adjusting impinging signals, these elements are able to perform unique functions, such as controlled reflection, amplification, absorption, etc. to boost the signal strength, alleviate the inter-channel interference and thus enhance the channel capacity gains [7]. Therefore, in a broader perspective, MBM can be regarded as a special case of RIS, as both the parasitic elements in MBM and smart reflecting elements of RIS are utilized to create and shape a dense propagation environment.

In this thesis, taking inspiration from these promising developments, we have explored the potential of the IM principle for future generation systems, and developed novel high-rate transmission system designs ranging from integration MBM with space-time codes to the RIS-aided multi-user transmission schemes. The major contributions of this thesis are:

- Considering the International Mobile Telecommunications-Advanced (IMT-Advanced) channel statistics, we introduce a realistic two-dimensional (2D) physical channel simulator for an RIS-aided MBM transmission scheme by utilizing a real reconfigurable antenna (RA) with four radiation patterns [8].

- We present a general framework for MBM from the perspective of space-time coding and introduce two novel space-time coded IM concepts considering Hurwitz Radon [9] and circular matrices [10] that achieve a various number of transmit diversity gains.

- In order to avoid computationally intensive algorithms for optimizing the reflection phases of a passive RIS, considering the cosine similarity theorem, we design a

low-complexity algorithm for the RIS-aided MIMO and RIS-aided IM transmission schemes [11].

- We introduce a new IM transmission scheme that directly uses an RIS with passive and active reflecting elements as a transmit information unit [12].
- Leveraging the capability of an RIS on manipulating the magnitude of the incident wave, we propose a novel over-the-air beamforming concept for multi-user transmission, which customizes the RIS to achieve maximum sum-rate gains. Additionally, adapting the over-the-air beamforming approach, we develop a novel receive IM scheme [13].

1.2 Organization of Thesis

The rest of the thesis is organized as follows:

In Chapter 2, a comprehensive literature review of IM-based systems is presented. This chapter starts with an overview of the IM systems, then the existing related works on the classical MBM and the RIS-aided systems are summarized.

In Chapter 3, the open source *SimMBM* channel simulator is developed that leverages the parameters of a real RA to apply the MBM principle to a RIS-aided transmission scheme under realistic indoor and outdoor channel conditions for sub-6 GHz spectrum.

In Chapter 4, considering the space-time transmission principle, a novel space-time MBM (ST-MBM) scheme is presented. The proposed system is based on one of the prominent IM solutions, space shift keying (SSK), along with the Hurwitz-Radon family of matrices in order to achieve transmit diversity gains with a single RF chain by utilizing the unique RF mirror activation principle of MBM. Moreover, the theoretical pairwise error probability (PEP) of the ST-MBM scheme for correlated and uncorrelated channel states is derived and its theoretical average bit error probability (ABEP) is obtained. Additionally, a lower bound is derived for the mutual information of the ST-MBM scheme to gain insights into the information theoretical bounds of the proposed scheme. Furthermore, extensive computer simulations are provided to show the superior error performance of the ST-MBM scheme over the state-of-the-art MIMO transmission systems.

In Chapter 5, a circular STBC-based IM technique (CSTBC-IM) is introduced, in which a circular matrix is designed as an STBC matrix and integrated with the MBM transmission principle to achieve transmission diversity gain. Unlike traditional STBC-based IM concepts, the proposed technique provides various orders of transmit diversity gains and attains higher spectral efficiency values with a single RF chain. The bit error rate (BER) performance of the proposed system is theoretically analyzed and an upper bound expression for the ABEP is derived. Moreover, via comprehensive computer simulations, the improved BER performance of the proposed CSTBC-IM is demonstrated over the-state-of-the-art IM schemes.

In Chapter 6, taking MBM one step further, the contribution of RIS technology to emerging transmission systems is investigated. For this purpose, a cosine similarity theorem-based low-complexity algorithm for adapting the phase shifts of an RIS that assists a MIMO transmission system is introduced. Moreover, the proposed algorithm is generalized for the RIS-aided spatial modulation (RIS-SM) scheme that conveys additional information via activating a single transmit antenna at the transmitter. Furthermore, considering a semi-analytical probabilistic approach, the theoretical ABEP of the systems are derived, which are supported through extensive computer simulations.

In Chapter 7, a novel IM transmission scheme called hybrid reflection modulation (HRM), which deploys a hybrid RIS including both active and passive reflecting elements to convey information without using any RF chains, is presented. In the HRM scheme, the active reflecting elements using additional power amplifiers are able to amplify and reflect the incoming signal, while the remaining passive elements can simply reflect the signals with appropriate phase shifts. Based on this novel transmission model, we obtain an upper bound for the ABEP, and derive the achievable rate of the system using an information theoretic approach. Moreover, comprehensive computer simulations are performed to prove the superiority of the proposed HRM scheme over existing fully passive, fully active, and reflection modulation (RM) systems.

In Chapter 8, the potential of active RIS is further investigated from a different perspective. Deploying an active RIS, a novel beamforming concept, over-the-air beamforming, for RIS-aided multi-user multiple-input single-output

(MISO) transmission schemes without requiring any pre/post signal processing hardware designs at the transmitter and receiver sides is developed. In the proposed over-the-air beamforming-based transmission scheme, the reflection coefficients of the active RIS elements are customized to maximize the sum-rate gain. To tackle this issue, first, a non-convex quadratically constrained quadratic programming (QCQP) problem is formulated. Then, using the semidefinite relaxation (SDR) approach, this optimization problem is converted to a convex feasibility problem, which is efficiently solved using the CVX optimization toolbox. Moreover, taking inspiration from this beamforming technique, a novel high-rate receive IM scheme with a low-complexity sub-optimal detector is developed. Through comprehensive simulation results, the sum-rate and BER performance of the proposed designs are investigated.

In Chapter 9, the conclusions of this thesis are given.

***Notation**:* Throughout this thesis, bold capital and lowercase letters are used for matrices and vectors, respectively. Transposition and Hermitian transposition operators are denoted by $(\cdot)^T$ and $(\cdot)^H$, respectively. $\mathrm{Tr}(\cdot)$, $\mathrm{rank}(\cdot)$ and $\det(\cdot)$ respectively stand for the trace, the rank and the determinant of a matrix. $\|\cdot\|$ stands for the Euclidean/Frobenius norm and $\mathrm{vec}(\cdot)$ represents the vectorization operator. The complex Gaussian distribution of a random variable x with μ mean and σ^2 variance is denoted by $\mathcal{CN}(\mu,\sigma^2)$. $P_r(\cdot)$ stands for the probability of an event and $\mathbb{E}\{\cdot\}$ denotes expectation. Gaussian Q-function, the entropy function and the Kronecker product are represented by $Q(\cdot)$, $H(\cdot)$ and $\otimes$, respectively. $\mathbf{I}_m$ denotes the $m \times m$ identity matrix, $\mathbb{C}^{m\times n}$ represents the set of complex-valued matrices with dimensions of $m \times n$, while $\mathcal{O}(\cdot)$ denotes big $\mathcal{O}$ notation.

2. LITERATURE REVIEW

In this chapter, a literature review for IM-based systems is given. The chapter starts with an overview of the IM transmission principle and proceeds with the related works of the MBM and RIS-aided studies.

2.1 Index Modulation: A Historical Perspective

The evolution of MIMO technology has boosted the overall performance of traditional communication systems from many different aspects. The capability of the MIMO systems to meet the growing demand for higher data rates and higher capacity significantly accelerates the development of today's wireless technologies. Consequently, MIMO techniques have been widely used in wireless standards including Long Term Evolution (LTE), IEEE 802.11x (Wi-Fi) and IEEE 802.16 (WiMAX). According to the conventional MIMO transmission concept [14], since all transmit antennas are used for signaling, an increasing number of transmit antennas leads to a higher data rate and, at the same time, remarkably increases the transceiver complexity, which is considered as the main drawback of these early designs.

Over the past decade, there has been a growing trend towards increasing the data rate by conveying additional information bits through the building blocks of a MIMO transmission system by the novel concept of IM [2]. Compared to the early hardware-complex multi-antenna systems [14], the IM systems are considered as potential solutions for future networks, with their advantageous attributes such as low-complexity and energy-efficient hardware designs [2].

2.1.1 Spatial modulation

SM [3], which utilizes the indices of the available transmit antennas of a MIMO system to convey extra information bits besides the conventional modulation bits, has been regarded as the pioneer of IM techniques. As given in Figure 2.1, in the SM transmission scheme, in addition to selecting a modulated symbol from a phase

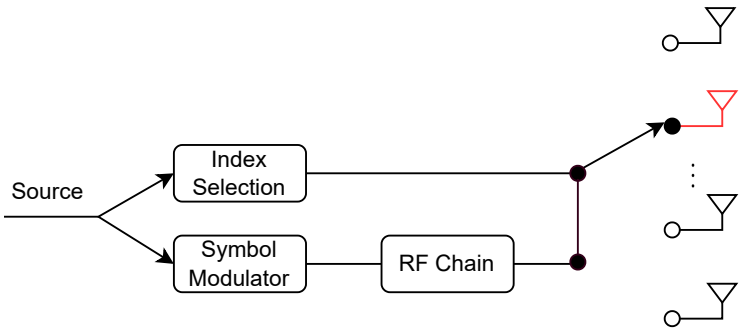

Figure 2.1 : Transmitter diagram of spatial modulation.

shift keying (PSK) or a quadrature amplitude modulation (QAM) constellation, the incoming information bits also determine the index of the transmit antenna to be activated through which the communication is established. Therefore, unlike the classical multi-antenna transmitters [14], in SM, a considerable spectral efficiency improvement is achieved in a more energy-efficient manner via employing a single RF chain. Afterwards, this innovative concept has been developed and numerous follow-up studies on SM have been performed under diverse research fields [15]. In [16], SSK scheme, which only transmits information bits by specifying the index of the active transmit antenna is introduced. Later, in order to attain significant spectral efficiency improvement, the SM transmission scheme is generalized for activating multiple transmit antennas in each transmission interval [17, 18]. Subsequently, in [19, 20], SM-based multi-carrier communication systems are developed, while [21] offers novel insights in SM-based spread spectrum communication. Further, SM is adapted into optical wireless communications [22,23], mmWave [24], spread spectrum [25] and visible light communication systems [26], and so on.

2.1.2 Media-based modulation

MBM [5] is a distinctive IM transmission scheme that transmits information via a multitude of different channel states. In the MBM scheme, a transmit antenna is equipped with external parasitic elements such as RF mirrors or PIN diodes to create different channel fade realizations from the perspective of the receiver. Then, according to incoming information bits, a particular transmission path is selected from these multiple-channel paths. Therefore, unlike the classical digital modulation schemes that transmit information over the basic characteristics of an incident wave

such as phase, amplitude, frequency, etc., in the MBM scheme, different channel state realizations constitute the MBM signal constellation.

This creative transmission technique has attracted a growing interest in the literature. In [27], the authors emphasize the significant gains of the MBM system using RF mirrors for practical channel realizations compared to classical single-input multiple-output (SIMO) and MIMO systems. In the follow-up studies, different STBC techniques are integrated with the MBM transmission scheme to achieve numerous orders of transmit diversity gains [9, 28]. Also, multi-user and massive MIMO implementations of the MBM system are reported in [29]. Further, traditional SM [3] and quadrature SM (QSM) [4] systems are adapted to the MBM concept in [30] and [31], respectively. Afterwards, the works of [28] and [32] integrated MBM with Alamouti's STBC [33] and uncoded space-time labeling diversity (USTLD) [34], respectively. Also, MBM-based multi-user networks [35] and uplink massive MBM-MIMO systems [29, 36] are proposed. To decrease the receiver complexity, iterative interference cancellation [37], constrained linear programming [38] and message passing-based [39] suboptimal detectors are designed, and the performance of the MBM scheme is investigated in the presence of imperfect channel estimation [40]. Later, MBM-based full-duplex [41] and secrecy communication [42, 43] systems are developed.

2.2 From Media-based Modulation to Reconfigurable Intelligent Surfaces

Above this immense literature, as being the first study of manipulating the transmission environment in order to attain higher data rates, MBM has paved the way toward next-generation networks that build programmable wireless environments.

Recently, RIS-enhanced technology, which constructively adapts the propagation environment of a communication system through controllable electromagnetic materials, is dominating the wireless communications literature. As in the MBM transmission, these controllable electromagnetic elements at RIS enrich the scattering environment. Moreover, the unique functions of the reflecting elements such as reflection, amplification, absorption, etc., enable the RIS to provide a further contribution toward improving transmission quality. Therefore, the RIS technology

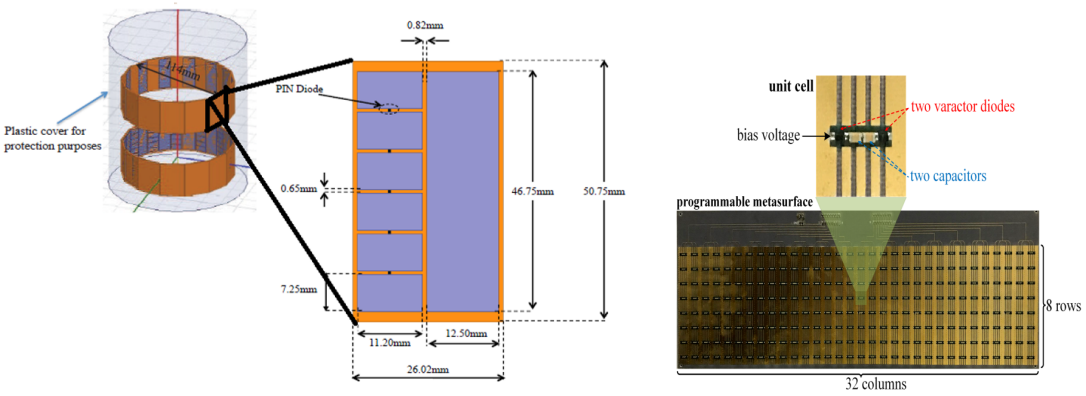

a) b)

Figure 2.2 : Prototypes for a) MBM and b) RIS exploiting PIN diodes and varactors for each cell, respectively.

exploiting smart controllable elements can be considered as an improved version of the MBM transmission.

In order to better assess the transition between MBM and RIS, their prototypes [44,45] are given in Figure 2.2. The prototype given in Figure 2.2a) is from one of the early MBM designs that surrounds a transmit antenna with two sets of vertically stacked PIN diodes creating various numbers of channel realizations [44]. On the other hand, an RIS prototype with 256 unit cells, each controlled through two varactor diodes for a proper phase adjustment, is given in Figure 2.2b) [45]. Therefore, it is apparent that the MBM and RIS are two family technologies based on the same foundations. However, while the core idea of MBM is to achieve a higher data rate, RIS enables to customize the transmission medium in a constructive manner.

2.2.1 RIS-aided transmission schemes

The unprecedented potential of RISs on the signal quality of a communication system has led researchers to use the RIS technology in various frontiers. In early RIS-aided transmission schemes, multi-user systems that optimize the transmit power [46–48], error performance [49–51], and achievable rate [52–55] have been developed in order to achieve major performance gains. Further, an RIS is deployed for improving the physical layer security of target communication systems [56–58], while in [59–61], deep learning-based efficient solutions are developed for channel estimation and reflection-based designs. Recently, leveraging RIS, realistic millimeter wave (mmWave) channel models [62, 63] are designed and implemented. Even more

recently, to facilitate practical implementation of the RIS aided systems, new path loss models [64, 65], open-source channel models [66, 67] and a practical phase shift model [68] are developed. Above all, unlike the aforementioned systems that consider computer simulations, in [69–71], low-cost RIS prototypes are constructed to obtain more accurate results about the actual performance of the RIS-aided systems through experimental measurements.

The proliferation of literature on RIS technology heightens the need for increasing data rates using IM techniques. Therefore, the combination of RISs with the traditional IM systems has been aroused in [8, 72, 73], where the information is transmitted via indices of transmit/receive antennas, and an RIS is adopted to further enhance transmission performance. Moreover, the performance analysis of the RIS-aided IM (RIS-IM) schemes has been investigated in [74–76] and novel closed-form expressions are obtained in [77]. On the other hand, in recent studies, a novel IM technique, reflection modulation (RM), has been developed to utilize the reflecting elements as information transmitting units [78]. In recent RM systems, using ON/OFF keying mechanism of the passive reflection elements, an RIS has been deployed to carry information [79–82]. Nevertheless, the abovementioned system designs suffer from multiplicative path attenuation due to the inherent drawback of the RIS-aided designs and achieve poor performance gains over the conventional communication systems.

Recently, to tackle the above challenges, the concept of active RIS, which performs simultaneous amplification and reflection on the incident wave, is introduced in [83, 84]. Accordingly, the magnitudes and the phases of the reflecting elements of the active RIS, which are equipped with additional power amplifiers, are properly tuned in a customized way [85]. Therefore, at the cost of additional power consumption, active RIS-aided systems are capable of achieving enhanced capacity gains [84]. In a recent study on designing active RISs, dynamic and fixed hybrid RIS architectures are constructed via leveraging power amplifiers and RF chains as active elements [86]. Further, for improving the data rate, a new RM design, which employs the sub-groups of a hybrid RIS as information transfer units, is presented in [12]. In follow-up studies, the concept of the active RIS is deployed for beamforming optimization of the RIS-aided multi-user systems [87, 88]. Above all, the potential of active RIS-aided

Table 2.1 : Comparison of traditional and state-of-the-art IM systems.

	Refs.	Scheme	Hardware Complexity	Spectral Efficiency
Traditional Systems	[14]	MIMO	High	High
	[3]	SM	Moderate	Moderate
	[16]	SSK	Low	Moderate
	[4]	QSM	Moderate	High
	[27]	MBM	Low	Moderate
RIS-aided Systems	[74–76]	RIS-IM	Moderate	Moderate
	[78–82]	RM	Low	Moderate

systems for achieving enormous performance gains will enable to develop promising solutions for future research.

In conclusion, this chapter presents a detailed literature review of the classical and state-of-the-art IM schemes ranging from early SM-based studies to RIS-aided IM systems. Moreover, the comparison of the hardware complexity and spectral efficiency of the reviewed IM schemes are briefly summarized in Table 2.1. Here, the SSK [16], MBM [27] and RM systems [78–82] with low hardware complexities and high spectral efficiency values offer superior performance achievements over the other IM-based systems.

3. SIMMBM CHANNEL SIMULATOR FOR MBM SYSTEMS

In this chapter, considering IMT-Advanced recommendations [89], *SimMBM* channel simulator is released for simulating realistic and two-dimensional (2D) MBM transmission channels that are pertinent to sub-6 GHz [89] applications of the specific indoor hotspot (InH), urban micro (UMi) and urban macro (UMa) network configurations. Unlike the classical MBM studies [9, 28, 29, 90] that consider RF mirrors around transmit antenna(s) to create questionably independent channel state realizations, in *SimMBM*, we assume that a real RA with four radiation patterns [91] that inherently capable of generating channel variations is utilized, while a generalization to the case of multiple radiation patterns is straightforward. This open-source channel simulator offers different environment types (InH, UMi and UMa), and allows locations variations.

The remainder of this chapter is organized as follows. We present the overall structure of the channel simulator, including the MBM systems and IMT-Advanced channel modeling concepts in Section 3.1. In Section 3.2, the channel correlation and capacity measurements of the MBM systems are provided. Our numerical results are presented in Section 3.3 and conclusions are given in Section 3.4.

3.1 SIMMBM Channel Simulator

In this section, the *SimMBM* channel simulator, which generates the MBM transmission channels characterized by the IMT-Advanced standards at sub-6 GHz frequency band, is introduced.

3.1.1 IMT-Advanced channel modeling

The IMT-Advanced systems proving extensive transmission protocols for mobile communications and broadband connectivity are growingly deployed worldwide in today's wireless communication systems [1]. In this study, the proposed *SimMBM* channel simulator, which produces MBM channels in various indoor and outdoor

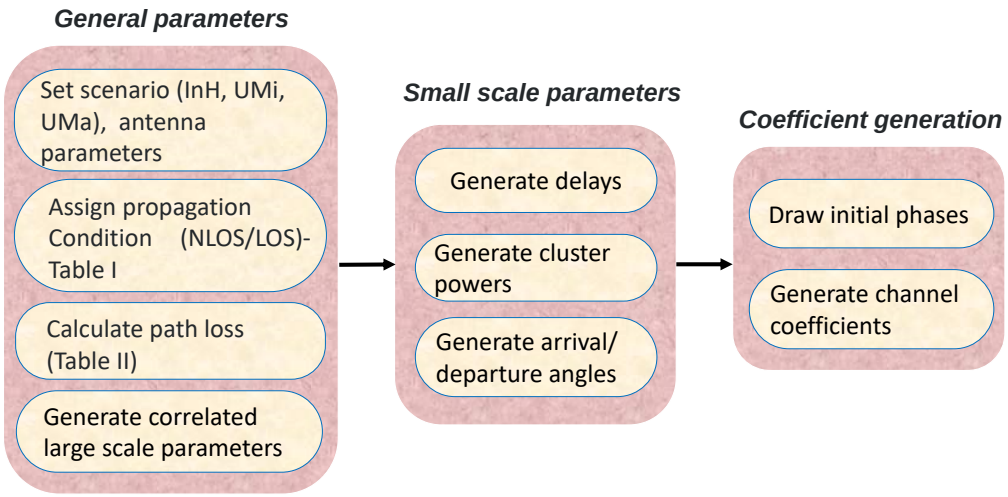

Figure 3.1 : IMT-Advanced channel coefficient generation procedure.

environments, follows IMT-Advanced channel modeling procedure illustrated in Figure 3.1 [89].

In this study, first, we consider a generic single-input single-output (SISO) system whose propagation environment is characterized by IMT-Advanced channel models that consist of multiple clusters, each composing a number of sub-rays with similar characteristics referred to as *scatterers*. Each cluster is characterized by *large scale parameters* which are statistical parameters such as delay spread (DS) and angular spread (AS) that follow the distributions given in Table 3.1 [89]. Then, these parameters are employed to assign delay $\tau_{c,s}$, power $P_{c,s}$, departure $\phi_{c,s}$ and arrival $\varphi_{c,s}$ angles to each path, which are often referred to as *small scale parameters*. where f_c is operating frequency at the sub-6 GHz frequency band.

Accordingly, after specifying a scenario among the available network configurations InH, UMi and UMa, distance-dependent line of sight (LOS) probability $p(d)$, for d being the 2D distance between the transmitter (T) and the receiver (R), is determined as given in Table 3.2 [89]. Please note that throughout this chapter, the terms "T" and "R" will be used to refer transmitter and the receiver, respectively.

After determining whether a LOS propagation link exists between the T and R, the attenuation caused by path loss and shadowing fading (SF), in decibel (dB), is calculated, using the path loss parameters given in Table 3.3 [89], as follows

$$P_L(d)\,[\text{dB}] = -X\log_{10}(d) - Y - Z\log_{10}(f_c) - \sigma_{SF}. \tag{3.1}$$

Table 3.1 : Channel parameters for sub-6 GHz spectrum.

		InH		**UMi**		**UMa**	
		LOS	**NLOS**	**LOS**	**NLOS**	**LOS**	**NLOS**
Delay spread (DS) $\log_{10}(s)$	μ	-7.70	-7.41	-7.19	-6.89	-7.03	-6.44
	σ	0.18	0.14	0.40	0.54	0.66	0.39
AoD spread (ASD) $\log_{10}(^\circ)$	μ	1.60	1.62	1.20	1.41	1.15	1.41
	σ	0.18	0.25	0.43	0.17	0.28	0.28
AoA spread (ASA) $\log_{10}(^\circ)$	μ	1.62	1.77	1.75	1.84	1.81	1.87
	σ	0.22	0.16	0.19	0.15	0.20	0.11
AoA/AoD distribution		Laplacian		Wrapped Gaussian		Wrapped Gaussian	
Number of clusters		15	19	12	19	14	12
Number of rays per cluster		20	20	20	19	20	20
Cluster ASD		5	5	3	10	5	2
Cluster ASA		8	11	17	22	11	15

Table 3.2 : LOS probability.

	LOS Probability
InH	$p(d) = \begin{cases} 1 & d \leq 18 \\ \exp(-(d-18)/27) & 18 < d < 27 \\ 0.5 & d \geq 37 \end{cases}$
UMi	$p(d) = \min(18/d, 1)(1 - \exp(-d/36)) + \exp(-d/36)$
UMa	$p(d) = \min(18/d, 1)(1 - \exp(-d/63)) + \exp(-d/63)$

Assume C and S respectively represent the number of total clusters and number of scatterers within each cluster, and (c, s) denotes the sth scatterer of the cth cluster. Therefore, considering IMT-Advanced channel parameters in Table 3.1 [89], the geometric channel between this generic SISO system is constructed as [89]

$$h = \sum_{c=1}^{C} \sum_{s=1}^{S} \alpha_{c,s} \sqrt{G_t(\phi_{c,s}) G_r(\varphi_{c,s}) P_L(d)} e^{j\theta} + h_{\text{LOS}} \tag{3.2}$$

Table 3.3 : Path loss parameters.

Scenario		X	Y	Z	σ_{SF}
InH	LOS	16.9	32.8	20	3
	NLOS	43.3	11.5	20	4
UMi	LOS	22	28	20	3
	NLOS	36.7	22.7	26	4
UMa	LOS	22	28	20	4

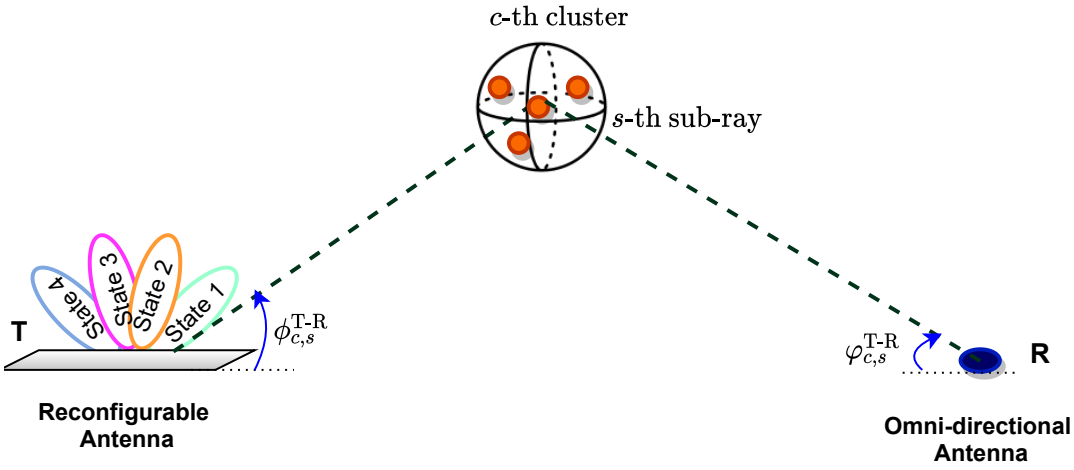

Figure 3.2 : SISO-MBM transmission.

where h_{LOS} is the LOS component, θ is the initial phase uniformly distributed between $[0, 2\pi]$, i.e., $\theta \sim \mathcal{U}(0, 2\pi)$, while $G_t(\phi_{c,s})$ and $G_r(\phi_{c,s})$ are the transmit and receive antenna gains in the direction of the (c, s)th path, respectively. In (3.2), $\alpha_{c,s} \sim \mathcal{CN}(0, P_{c,s})$ is assumed to be independent identically distributed (i.i.d) complex Gaussian random variable with zero mean and $P_{c,s}$ variance for $P_{c,s}$ being the average power of the (c, s) path and $\sum_{c,s} P_{c,s} = 1$, while h_{LOS} is determined as

$$h_{\text{LOS}} = I_{\text{LOS}}(d)\sqrt{G_t(\phi_{\text{LOS}})G_r(\varphi_{\text{LOS}})P_L(d)}e^{j\theta} \tag{3.3}$$

where $I_{\text{LOS}}(d)$ is Bernoulli random variable with $p(d)$ probability, indicating existence of a LOS link between the T and R. $G_t(\phi_{\text{LOS}})$ and $G_r(\varphi_{\text{LOS}})$ are the transmit and the received antenna gain in LOS direction, respectively.

3.1.2 RA-based MBM channels

In this study, considering IMT-Advanced standards for sub-6 GHz applications described above [89], we consider the propagation environment of a SISO system whose schematic diagram is given in Figure 3.2. It is assumed that a single RA with four different directional radiation patterns operating at 2.45 GHz frequency [91] is employed at T, while R is equipped with an omni-directional antenna that collects signals with unit gain in all directions.

The considered RA exploits four arc dipoles as radiating elements and manipulates the radiation direction by ON/OFF status of PIN diodes [91], which create four directional radiation patterns presented in Figure 3.3. It is worth noting that the radiation patterns

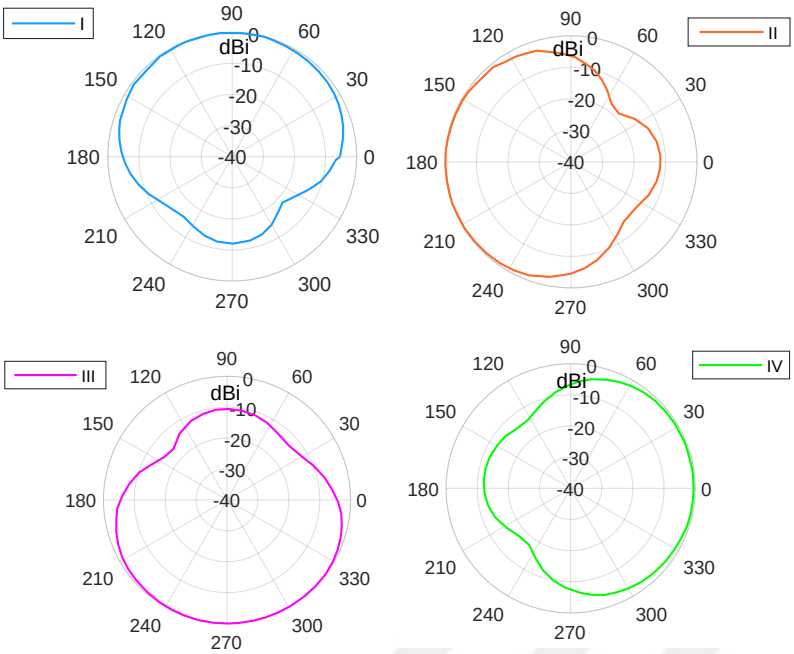

Figure 3.3 : Radiation patterns of the four-state RA in azimuth direction.

of this RA are extracted from 2D polar plots given in [91] by using a software program [92]. Moreover, this RA with pattern diversity can steer 360° in the azimuth plane and allows us to perform the classical MBM concept [90, 93] between T and R. Therefore, considering the above azimuth beam steering RA [91], an RA-based SISO-MBM system is constructed.

In this system, considering the classical MBM transmission principle, the incoming $m = \log_2(4) = 2$ information bits determine one out of four radiation patterns of the RA [91] to be activated in each transmission interval by switching ON/OFF status of the corresponding PIN diode. Therefore, considering the geometry-based IMT-Advanced channels reported in the preceding subsection, the transmission channel of the SISO-MBM system is constructed as

$$h_p = \sum_{c=1}^{C} \sum_{s=1}^{S} \alpha_{c,s} \sqrt{G_p(\phi_{c,s}) P_L(d)} e^{j\theta} + h_{\text{LOS}} \tag{3.4}$$

where $G_p(\phi_{c,s})$ is the antenna gain of the pth state in direction of $\phi_{c,s}$ angle for p denoting the index of the active radiation pattern.

Furthermore, to enhance the spectral efficiency of the SISO-MBM scheme, it is generalized for a MIMO configuration with uniform linear array (ULA) deployment of T_x RA antennas at T and R_x omni-directional antennas at R. Further, in this MIMO-MBM system, by assigning $\log_2(4) = 2$ bits to each RA, all available transmit

RAs are used for transmission through their active radiation patterns which are determined via the incoming $m = T_x \log_2(4) = 2T_x$ bits. Therefore, the channel coefficient between the ith transmit RA and jth received antenna is constructed as follows

$$f_{i,j} = \sum_{c=1}^{C} \sum_{s=1}^{S} \alpha_{c,s} \sqrt{P_L(d_{\text{T-R}})} \sqrt{G_p^i(\phi_{c,s}^{\text{T-R}})} \times e^{jkd_a(i-1)\sin(\phi_{c,s}^{\text{T-R}})} e^{jkd_a(j-1)\sin(\varphi_{c,s}^{\text{T-R}})}. \tag{3.5}$$

In (3.5), for $d_{\text{T-R}}$ being distance between the T and R, $G_p^i(\phi_{c,s}^{\text{T-R}})$ is the gain of the pth pattern corresponding to ith transmit RA, $k = 2\pi/\lambda$, and d_a is the distance between adjacent antennas, which is assumed to be $d_a = \lambda/2$, and λ is the wavelength. Therefore, the overall channel matrix between T and R, $\mathbf{F} \in \mathbb{C}^{R_x \times T_x}$, becomes

$$\mathbf{F} = \sum_{c=1}^{C} \sum_{s=1}^{S} \alpha_{c,s} \sqrt{P_L(d_{\text{T-R}})} \mathbf{a}^{\text{H}}(\phi_{c,s}^{\text{T-R}}) \mathbf{a}(\varphi_{c,s}^{\text{T-R}}) + \mathbf{F}_{\text{LOS}} \tag{3.6}$$

where $\mathbf{F}_{\text{LOS}}$ is the LOS component, $\mathbf{a}(\phi_{c,s}^{\text{T-R}})$ and $\mathbf{a}(\varphi_{c,s}^{\text{T-R}})$ denote the transmit and received array response vectors at the corresponding departure $\phi_{c,s}^{\text{T-R}}$ and arrival $\varphi_{c,s}^{\text{T-R}}$ angles, respectively. In (3.6), the ULA-based RA array response vector $\mathbf{a}(\phi_{c,s}) \in \mathbb{C}^{T_x \times 1}$ (including gains) is

$$\mathbf{a}(\phi_{c,s}^{\text{T-R}}) = \left[\sqrt{G_p^1(\phi_{c,s}^{\text{T-R}})} \;\; \sqrt{G_p^2(\phi_{c,s}^{\text{T-R}})} e^{jkd_a \sin(\phi_{c,s}^{\text{T-R}})} \;\; .. \sqrt{G_p^{T_x}(\phi_{c,s}^{\text{T-R}})} e^{jkd_a(T_x-1)\sin(\phi_{c,s}^{\text{T-R}})} \right]^T \tag{3.7}$$

while ULA-based omni-directional receiver array vector $\mathbf{a}(\varphi_{c,s}^{\text{T-R}}) \in \mathbb{C}^{R_x \times 1}$ is

$$\mathbf{a}(\varphi_{c,s}^{\text{T-R}}) = \left[1 \;\; e^{jkd_a \sin(\varphi_{c,s}^{\text{T-R}})} \;\; \ldots \;\; e^{jkd_a(R_x-1)\sin(\varphi_{c,s}^{\text{T-R}})} \right]^T. \tag{3.8}$$

3.1.3 RIS-aided MBM systems

Since the RIS technology offers cost-effective solutions for future communication systems, there is a growing body of literature on novel RIS-aided transmission system designs [94]. In that sense, in order to enhance the signal quality of the aforementioned MIMO-MBM schemes, an RIS is integrated between T and R. In this new RIS-aided MBM system, to ensure consistency with the above 2D IMT-Advanced channel models, a ULA-based RIS with $d_r = \lambda/2$ spaced N passive reflecting elements is placed between T and R of the $R_x \times T_x$ MIMO-MBM system as illustrated in Figure 3.4. Furthermore, in this system, in order to get a significant gain from the RIS, we

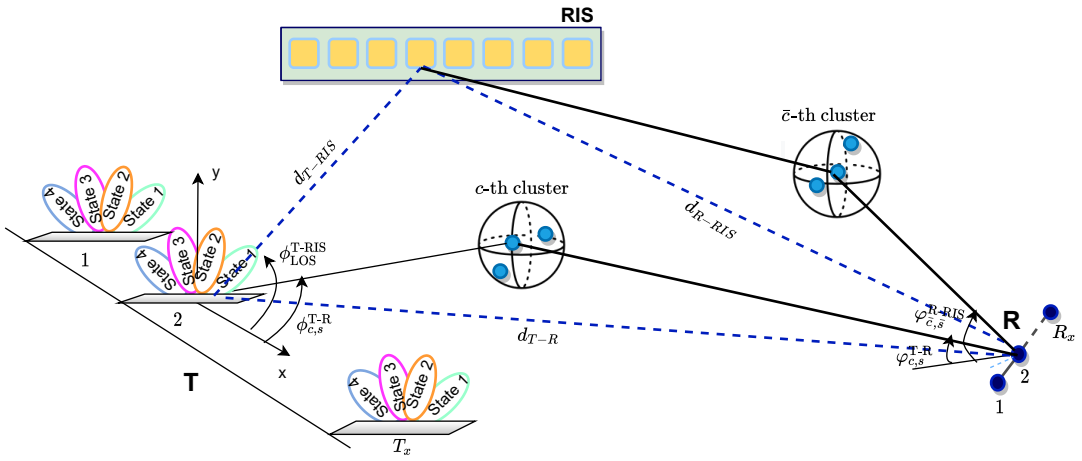

Figure 3.4 : RIS-aided MIMO-MBM system.

assume the RIS to be close enough to T to ensure pure LOS links. On the other hand, R is assumed to be sufficiently far from the RIS and T to allow multi-path propagation in T-R and R-RIS links.

Obviously, the multi-path propagation environment of the T-R link corresponds to the MIMO-MBM channel described in the previous subsection. Therefore, the channel matrix characterizing the T-R link becomes $\mathbf{F} \in \mathbb{C}^{R_x \times T_x}$ as given in (3.6)-(3.8).

Likewise, since we assume pure LOS links in T-RIS link, considering IMT-Advanced models, the LOS channel of T-RIS link is obtained as

$$\mathbf{H} = I_{\text{LOS}}(d_{\text{T-RIS}})\sqrt{P_L(d_{\text{T-RIS}})G_e}e^{j\theta} \times \mathbf{a}(\phi_{\text{LOS}}^{\text{T-RIS}})\mathbf{a}^{\text{H}}(\varphi_{\text{LOS}}^{\text{T-RIS}}) \tag{3.9}$$

where $d_{\text{T-RIS}}$ is the LOS distance of the T-RIS path, and G_e symbolizes the gain of the RIS elements, which is assumed to be $G_e = \pi$ [66]. In addition, $P_L(d_{\text{T-RIS}})$ is the attenuation between T-RIS link that can be calculated from (3.1), while $\mathbf{a}(\phi_{\text{LOS}}^{\text{T-RIS}})$ and $\mathbf{a}(\varphi_{\text{LOS}}^{\text{T-RIS}})$ respectively are the array response vectors of the T and RIS in LOS direction. Thus, $\mathbf{a}(\phi_{\text{LOS}}^{\text{T-RIS}})$ is calculated as in (3.7), $\mathbf{a}(\varphi_{\text{LOS}}^{\text{T-RIS}})$ is obtained as follows

$$\mathbf{a}(\varphi_{\text{LOS}}^{\text{T-RIS}}) = \left[1 \;\; e^{jkd_r \sin(\varphi_{\text{LOS}}^{\text{T-RIS}})} \;\; \dots \;\; e^{jkd_r(N-1)\sin(\varphi_{\text{LOS}}^{\text{T-RIS}})}\right]^T. \tag{3.10}$$

On the other hand, for the R-RIS link, we consider a multi-path propagation environment. Let $\bar{C}$ and $\bar{S}$ respectively symbolize the number of clusters and scatterers within each cluster in R-RIS link. Then, the R-RIS channel matrix is constructed as

$$\mathbf{G} = \sum_{c=1}^{\bar{C}}\sum_{s=1}^{\bar{S}} \alpha_{\bar{c},\bar{s}}\sqrt{G_e P_L(d_{\text{R-RIS}})} \times \mathbf{a}(\phi_{\bar{c},\bar{s}}^{\text{R-RIS}})\mathbf{a}^H(\varphi_{\bar{c},\bar{s}}^{\text{R-RIS}}) + \mathbf{G}_{\text{LOS}} \tag{3.11}$$

where $d_{\text{R-RIS}}$ is the distance from the RIS to R, $\mathbf{G}_{\text{LOS}}$ is the LOS component which is separately obtained from multi-path propagation, and $\mathbf{a}(\phi_{\bar{c},\bar{s}}^{\text{R-RIS}})$ and $\mathbf{a}(\varphi_{\bar{c},\bar{s}}^{\text{R-RIS}})$ respectively are the array response vectors at $\phi_{\bar{c},\bar{s}}^{\text{R-RIS}}$ and $\varphi_{\bar{c},\bar{s}}^{\text{R-RIS}}$ directions.

After all, the composite channel of the RIS-aided MBM system is constructed by combinations of the direct and the reflected paths as $\mathbf{C} \in \mathbb{C}^{R_x \times T_x} = \mathbf{G}\mathbf{\Phi}\mathbf{H} + \mathbf{F}$, where $\mathbf{\Phi} \in \mathbb{C}^{N \times N}$ is the diagonal reflection matrix of the RIS. It is worth stating that diagonal reflecting matrix of $\mathbf{\Phi}$ is constructed considering [95] for SISO-MBM and [96] for MIMO-MBM systems.

Consequently, the received signal of the RIS-aided MIMO-MBM system $\mathbf{y} \in \mathbb{C}^{R_x \times 1}$ becomes

$$\mathbf{y} = \mathbf{C}\mathbf{x} + \mathbf{n} \tag{3.12}$$

for $\mathbf{x} \in \mathbb{C}^{T_x \times 1} = \mathbf{1}$ being the all-one transmission signal vector whose each element corresponds to an unmodulated carrier signal, while $\mathbf{n}$ is additive white Gaussian noise (AWGN) vector composing i.i.d. random variables, where each follows $\mathcal{CN}(0, N_0)$ distribution.

3.2 Correlation and Capacity Analysis

This section provides correlation and capacity analyses of the MBM systems.

3.2.1 Correlation analysis

Although channel correlation is a key factor determining the robustness and efficiency of the MBM systems, there has been little discussion about the realistic correlation models for MBM [90]. In this study, although the same propagation environment is considered, the pattern diversity of the RA in Figure 3.3 [91] which exploits the RF characteristics of the environment, allows signals from different radiation patterns to follow different paths in arriving the receiver.

In this subsection, the channel correlation caused by different radiation patterns of the RA [91] is computed through Monte Carlo simulations. For this reason, the SISO-MBM scheme whose transmit channel coefficient h_p corresponding to the pth RA pattern given in (3.2), is considered. For L being number of total sub-rays, the cross-channel correlation corresponding to p and q modes of the RA can be calculated

from

$$\mathbf{R}_{p,q} = \mathbb{E}\left\{h_p h_q^*\right\} \tag{3.13}$$

$$= \mathbb{E}\left\{\sum_{l=1}^{L}\left\{P_L(d_{\text{T-R}})\sqrt{G_p(\phi_l^{\text{T-R}})G_q(\phi_l^{\text{T-R}})}\right\}\right\} \tag{3.14}$$

where $p, q \in \{1,2,3,4\}$, and $\mathbb{E}\{\cdot\}$ is the expectation.

Above all, considering IMT-Advanced NLOS InH scenario, the cross-correlation matrix of the SISO-MBM scheme is calculated via extensive computer simulations as follows

$$\mathbf{R} = \begin{bmatrix} 1.0000 & 0.7441 & 0.5667 & 0.6573 \\ 0.7441 & 1.0000 & 0.7390 & 0.6645 \\ 0.5667 & 0.7390 & 1.0000 & 0.9696 \\ 0.6573 & 0.6645 & 0.9696 & 1.0000 \end{bmatrix}. \tag{3.15}$$

The resulting $\mathbf{R}$ correlation matrix shows a manageable correlation between the channels generated by the radiation patterns of the RA [91], indicating the compatibility of the reference RA [91] for the MBM transmission.

3.2.2 Capacity analysis

The recent studies indicate that as in the classical MIMO transmission schemes, the channel capacity of IM-based systems is not dependent on the transmit signal constellations [97, 98]. Moreover, in [98], the capacity of the classical MIMO systems is calculated as an upper bound for the capacity of the IM-based MIMO systems. Therefore, considering [98], the capacity of the RIS-aided MIMO-MBM systems can be upper bounded using (3.12) as

$$R_c = \mathbb{E}\left\{\log_2\left[\det\left(\mathbf{I} + \frac{P_t}{N_0}\mathbf{C}\mathbf{C}^{\text{H}}\right)\right]\right\} \quad \text{[bits/s/Hz]} \tag{3.16}$$

where P_t is the transmission power and $\mathbf{I}$ is an identity matrix with R_x dimensions.

3.3 Simulation Results

In this section, to test our new channel simulator, we present a number of numerical results on the capacity of various MBM-based systems at sub-6 GHz band. In all simulations, the noise power is considered to be -100 dBm. Also, it should be noted that for InH scenarios, the 2D coordinates (x, y) of T, R and RIS are given as (30,10), (55,35) and (33,13), in meters (m), respectively. Additionally, for UMi and UMa

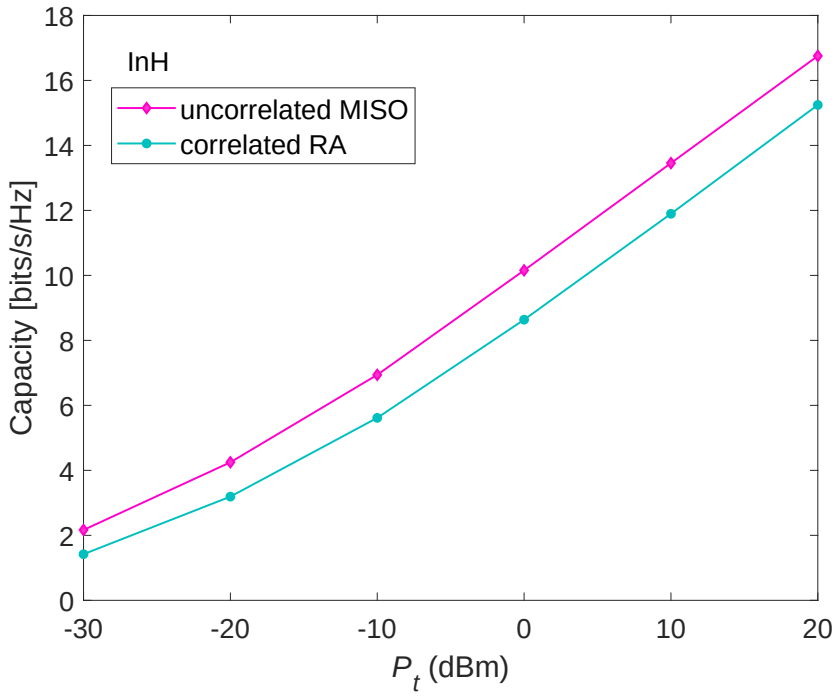

Figure 3.5 : Channel capacity comparison of the correlated 4-state RA and uncorrelated classical MISO systems.

scenarios the coordinates of T, R and RIS are assumed to be (45,15), (125,130) and (48,18) m.

In Figure 3.5, considering IMT-Advanced InH scenario, the capacity of the RA-based system [91] that generates low-correlated channel variations is compared with uncorrelated classical MISO transmission schemes that employ four transmit and a single received omni-directional antennas in transmission. The results indicate that the performance of the four-state RA [91] is slightly behind the uncorrelated multi-antenna system. This comparison is significant in understanding the effect of low channel correlations on the performance of MBM systems.

In Figure 3.6, the capacity of the SISO-MBM with/without the assistance of the RIS is investigated in different environments. It is clear from the results that since outdoor environments (UMi, UMa) experience higher attenuation in the direct T-R link, they require a higher number of reflecting elements in RIS to tackle this performance degradation.

In Figure 3.7, the capacity results of the MIMO-MBM systems in the UMi environment are demonstrated. It can be deduced from the results that as the MIMO

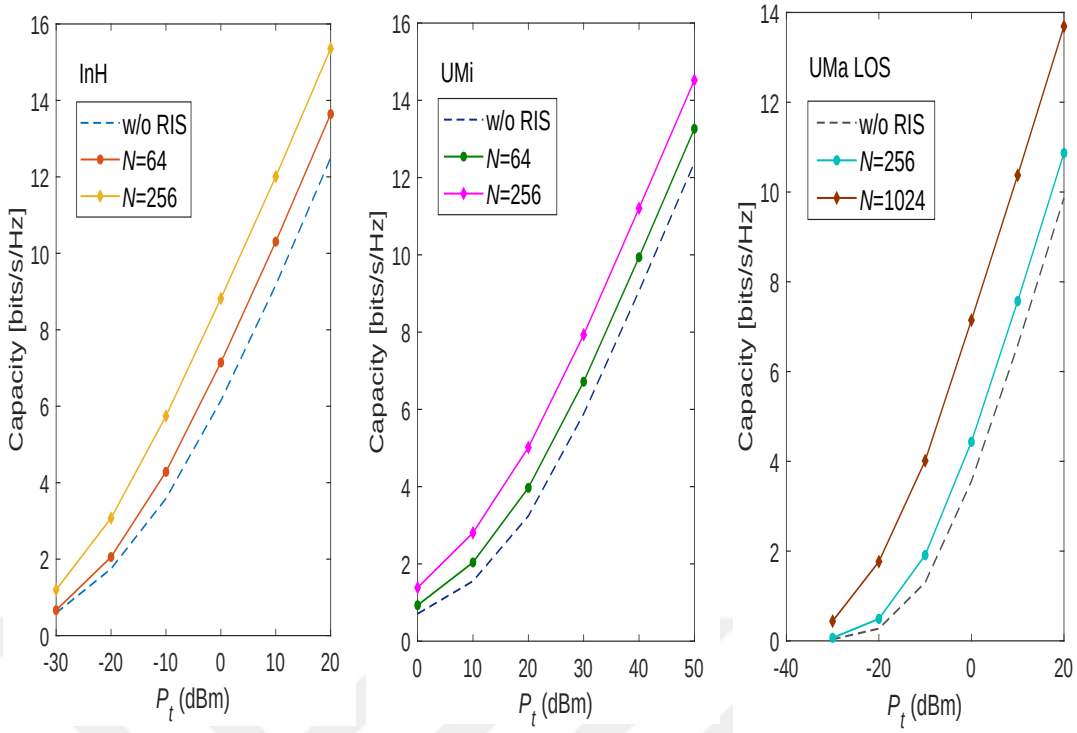

Figure 3.6 : Capacity of the RIS-aided MBM systems under a) InH b) UMi c) UMa LOS scenarios for varying N.

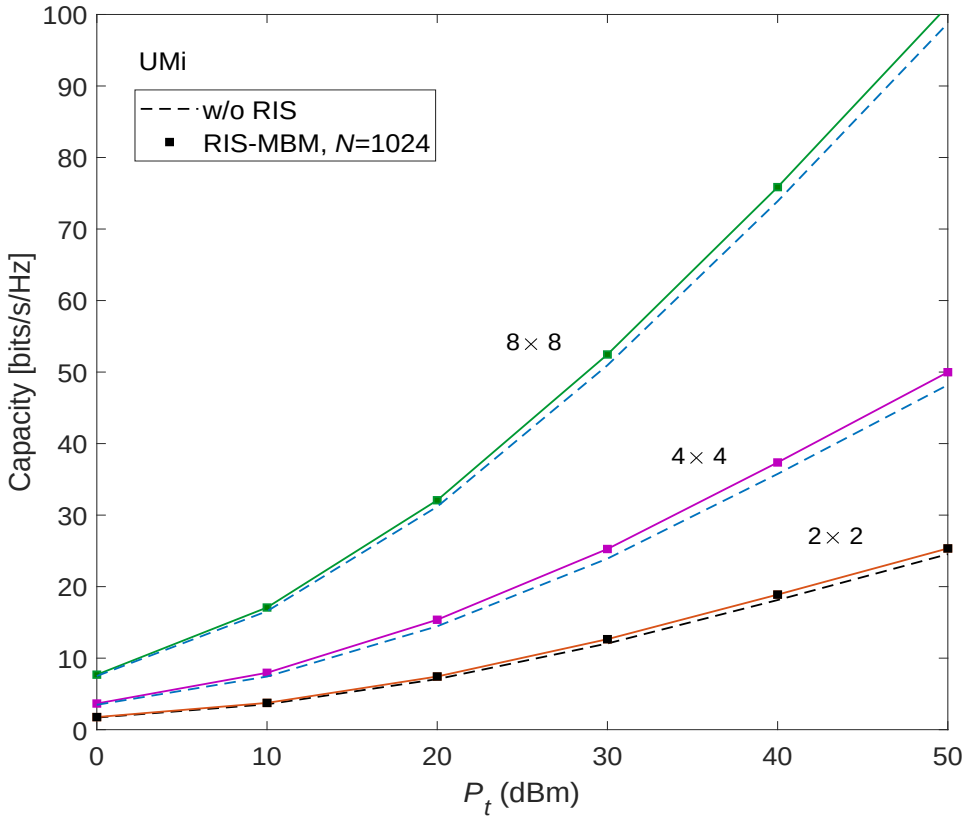

Figure 3.7 : Capacity of the MIMO-MBM systems for IMT-Advanced UMi scenario.

configuration enlarged, a linear relation between the path attenuation and capacity of the MIMO-MBM systems is observed. Therefore, the effect of the RIS on the system performance is hardly seen.

3.4 Summary

In this chapter, a 2D, open-source and easy-to-use physical channel simulator, *SimMBM*, enabling users to generate communication channels of the various MBM implementations at sub-6 GHz frequency spectrum, has been presented. The proposed channel simulator provides flexibility in modeling different MBM systems in realistic channel conditions in terms of different system parameters such as varying localizations and RA adaptations.

4. SPACE-TIME MEDIA-BASED MODULATION

In this chapter, an innovative concept based on the framework of SSK and MBM schemes, called *space-time media-based modulation (ST-MBM)*, is proposed by cleverly combining the Hurwitz-Radon family of matrices [99] with the MBM transmission approach. The proposed ST-MBM scheme is the first STBC-based scheme that achieves transmit diversity gains by using a single RF chain with a significantly lower receiver complexity. Theoretical error performance analysis of the proposed ST-MBM scheme is performed and its exact ABEP is derived for correlated and uncorrelated channel states. Furthermore, a lower bound is obtained for the mutual information of the ST-MBM scheme. Through comprehensive computer simulations, BER performance of ST-MBM scheme is compared with the existing state-of-the-art MIMO concepts in the literature.

The remaining of the chapter is organized as follows. The system model of the proposed ST-MBM scheme is introduced in Section 4.1. In Section 4.2, theoretical error performance and capacity analyses of the ST-MBM scheme are performed. Computer simulation results are presented in Section 4.3 and the chapter is concluded in 4.4.

4.1 Space-Time Media Based Modulation

An efficient way to compensate the inherently low spectral efficiency of STBC-based systems is to carry as much information as possible via the indices of the building blocks of the target transmission system. For a MIMO-MBM transmission scheme, the available building blocks for indexing are transmit antennas and RF mirrors. Besides these, in the proposed ST-MBM scheme, in order to further improve the spectral efficiency, information bits are subdivided into G transmission groups and space-time coding principle is independently applied to these transmission groups.

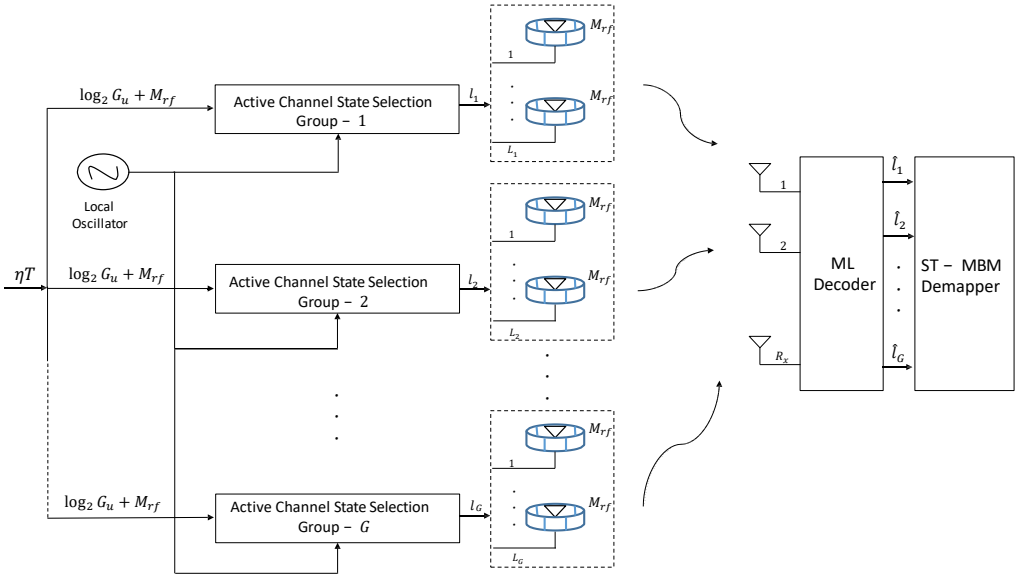

Figure 4.1 : Block diagram of the ST-MBM scheme.

In Figure 4.1, the block diagram of the proposed ST-MBM scheme, which achieves transmit diversity by expanding the transmission to T time slots while considering a MIMO configuration with T_x transmit and R_x receive antennas, is shown. In the ST-MBM scheme, each transmit antenna is surrounded by M_{rf} RF mirrors, where ON/OFF status of these M_{rf} RF mirrors generate $2^{M_{rf}}$ different channel fade realizations for each of T_x transmit antennas. As shown in Figure 4.1, incoming ηT information bits and, at the same time, T_x transmit antennas are subdivided into G groups. In each of these transmission groups,

$$\frac{\eta T}{G} = \log_2(G_u) + M_{rf} \tag{4.1}$$

bits are transmitted, where $G_u = T_x/G$ is defined as the number of transmit antennas in the uth transmission group, for $u \in \{1, 2, \ldots, G\}$. In each group, the first $\log_2 G_u$ bits of the incoming $\log_2(G_u) + M$ bits determine the index of the active transmit antenna, which is selected out of G_u available transmit antennas, while the following M_{rf} bits specify one of the available $2^{M_{rf}}$ channel states corresponding to this active antenna. It can be alternatively expressed that in each transmission group, one of the available $P_u = G_u 2^{M_{rf}}$ channel fade realizations, which are created jointly by reconfigurable antennas and the SSK concept, is selected by the incoming $\log_2(P_u)$ bits. Therefore, the total number of channel fade realizations through G transmission groups becomes $P = GP_u$, and the spectral efficiency of the ST-MBM scheme in bits per channel use

(bpcu) is given as

$$\eta = \frac{N\left[M_{rf} + \log_2\left(G_u\right)\right]}{T} = \frac{N\log_2(P_u)}{T} \tag{4.2}$$

due to the use of T time slot. The signaling structure of the proposed scheme in T time slots will be explained next.

For each transmission group, the incoming bits determine the transmission vector of the first time slot. This corresponds to an SSK vector, since no information is conveyed through the selected channel state by means of amplitude/phase modulations. Therefore, the transmission vector of the first time slot related to transmission group u can be given as

$$\mathbf{x}_u = [0 \cdots 0 \underbrace{1}_{l_u} 0 \cdots 0] \overbrace{\qquad\qquad}^{P_u} \tag{4.3}$$

where l_u denotes the index of the specified channel fade realization of the first time slot among P_u channel fade realizations in the uth transmission group, and $l_u \in \{1, 2, \ldots, P_u\}$. Then, the overall transmission matrix of each group is formed by the following structure of the Hurwitz-Radon family of matrices, where a detailed discussion is given below.

At the receiver side, in order to perceive complex Gaussian distributed random variables as in the case of SSK/MBM and, at the same time, to obtain transmit diversity gain, the Hurwitz-Radon family of matrices [99], a set of $S \times S$ real orthogonal matrices whose each row and column corresponds to an SSK vector, are used as core STBCs. For $l_u \in \{1, 2, \ldots, S\}$, each set of these $S \times S$ Hurwitz-Radon matrices satisfies the following conditions:

$$\begin{aligned}
&\mathbf{B}_{l_u}{}^T \mathbf{B}_{l_u} = \mathbf{I}_S \quad l_u = 2, \ldots, S \\
&\mathbf{B}_{l_u}{}^T = -\mathbf{B}_{l_u} \quad l_u = 2, \ldots, S \\
&\mathbf{B}_{l_u}\mathbf{B}_{l_u'} = -\mathbf{B}_{l_u'}\mathbf{B}_{l_u} \quad 1 \leq l_u < l_u^{'} \leq S
\end{aligned} \tag{4.4}$$

where $\mathbf{B}_1 = \mathbf{I}_S$ and $S \in \{2, 4, 8\}$. For $S = 4$, the Hurwitz-Radon matrices satisfying (4.4) are given as [99]

$$\begin{aligned} \mathbf{B}_1 &= \begin{bmatrix} 1 & 0 & 0 & 0 \\ 0 & 1 & 0 & 0 \\ 0 & 0 & 1 & 0 \\ 0 & 0 & 0 & 1 \end{bmatrix}, \mathbf{B}_2 = \begin{bmatrix} 0 & 1 & 0 & 0 \\ -1 & 0 & 0 & 0 \\ 0 & 0 & 0 & -1 \\ 0 & 0 & 1 & 0 \end{bmatrix} \\ \mathbf{B}_3 &= \begin{bmatrix} 0 & 0 & 1 & 0 \\ 0 & 0 & 0 & 1 \\ -1 & 0 & 0 & 0 \\ 0 & -1 & 0 & 0 \end{bmatrix}, \mathbf{B}_4 = \begin{bmatrix} 0 & 0 & 0 & 1 \\ 0 & 0 & -1 & 0 \\ 0 & 1 & 0 & 0 \\ -1 & 0 & 0 & 0 \end{bmatrix}. \end{aligned} \tag{4.5}$$

Similarly, the following Hurwitz-Radon matrices are constructed for $S = 8$ [99]:

$$\begin{aligned} \mathbf{B}_2 &= \begin{bmatrix} 0 & 1 & 0 & 0 & 0 & 0 & 0 & 0 \\ -1 & 0 & 0 & 0 & 0 & 0 & 0 & 0 \\ 0 & 0 & 0 & -1 & 0 & 0 & 0 & 0 \\ 0 & 0 & 1 & 0 & 0 & 0 & 0 & 0 \\ 0 & 0 & 0 & 0 & 0 & -1 & 0 & 0 \\ 0 & 0 & 0 & 0 & 1 & 0 & 0 & 0 \\ 0 & 0 & 0 & 0 & 0 & 0 & 0 & 1 \\ 0 & 0 & 0 & 0 & 0 & 0 & -1 & 0 \end{bmatrix}, \mathbf{B}_3 = \begin{bmatrix} 0 & 0 & 1 & 0 & 0 & 0 & 0 & 0 \\ 0 & 0 & 0 & 1 & 0 & 0 & 0 & 0 \\ -1 & 0 & 0 & 0 & 0 & 0 & 0 & 0 \\ 0 & -1 & 0 & 0 & 0 & 0 & 0 & 0 \\ 0 & 0 & 0 & 0 & 0 & 0 & 1 & 0 \\ 0 & 0 & 0 & 0 & 0 & 0 & 0 & 1 \\ 0 & 0 & 0 & 0 & -1 & 0 & 0 & 0 \\ 0 & 0 & 0 & 0 & 0 & -1 & 0 & 0 \end{bmatrix} \\ \mathbf{B}_4 &= \begin{bmatrix} 0 & 0 & 0 & 1 & 0 & 0 & 0 & 0 \\ 0 & 0 & -1 & 0 & 0 & 0 & 0 & 0 \\ 0 & 1 & 0 & 0 & 0 & 0 & 0 & 0 \\ -1 & 0 & 0 & 0 & 0 & 0 & 0 & 0 \\ 0 & 0 & 0 & 0 & 0 & 0 & 0 & 1 \\ 0 & 0 & 0 & 0 & 0 & 0 & -1 & 0 \\ 0 & 0 & 0 & 0 & 0 & 1 & 0 & 0 \\ 0 & 0 & 0 & 0 & -1 & 0 & 0 & 0 \end{bmatrix}, \mathbf{B}_5 = \begin{bmatrix} 0 & 0 & 0 & 0 & 1 & 0 & 0 & 0 \\ 0 & 0 & 0 & 0 & 0 & 1 & 0 & 0 \\ 0 & 0 & 0 & 0 & 0 & 0 & -1 & 0 \\ 0 & 0 & 0 & 0 & 0 & 0 & 0 & -1 \\ -1 & 0 & 0 & 0 & 0 & 0 & 0 & 0 \\ 0 & -1 & 0 & 0 & 0 & 0 & 0 & 0 \\ 0 & 0 & 1 & 0 & 0 & 0 & 0 & 0 \\ 0 & 0 & 0 & 1 & 0 & 0 & 0 & 0 \end{bmatrix} \\ \mathbf{B}_6 &= \begin{bmatrix} 0 & 0 & 0 & 0 & 0 & 1 & 0 & 0 \\ 0 & 0 & 0 & 0 & -1 & 0 & 0 & 0 \\ 0 & 0 & 0 & 0 & 0 & 0 & 0 & -1 \\ 0 & 0 & 0 & 0 & 0 & 0 & 1 & 0 \\ 0 & 1 & 0 & 0 & 0 & 0 & 0 & 0 \\ -1 & 0 & 0 & 0 & 0 & 0 & 0 & 0 \\ 0 & 0 & 0 & -1 & 0 & 0 & 0 & 0 \\ 0 & 0 & 1 & 0 & 0 & 0 & 0 & 0 \end{bmatrix}, \mathbf{B}_7 = \begin{bmatrix} 0 & 0 & 0 & 0 & 0 & 0 & 1 & 0 \\ 0 & 0 & 0 & 0 & 0 & 0 & 0 & -1 \\ 0 & 0 & 0 & 1 & 0 & 0 & 0 & 0 \\ 0 & 0 & 0 & 0 & 0 & -1 & 0 & 0 \\ 0 & 0 & -1 & 0 & 0 & 0 & 0 & 0 \\ 0 & 0 & 0 & 1 & 0 & 0 & 0 & 0 \\ -1 & 0 & 0 & 0 & 0 & 0 & 0 & 0 \\ 0 & 1 & 0 & 0 & 0 & 0 & 0 & 0 \end{bmatrix} \\ \mathbf{B}_8 &= \begin{bmatrix} 0 & 0 & 0 & 0 & 0 & 0 & 0 & 1 \\ 0 & 0 & 0 & 0 & 0 & 0 & 1 & 0 \\ 0 & 0 & 0 & 0 & 0 & 1 & 0 & 0 \\ 0 & 0 & 0 & 0 & 1 & 0 & 0 & 0 \\ 0 & 0 & 0 & -1 & 0 & 0 & 0 & 0 \\ 0 & 0 & -1 & 0 & 0 & 0 & 0 & 0 \\ 0 & -1 & 0 & 0 & 0 & 0 & 0 & 0 \\ -1 & 0 & 0 & 0 & 0 & 0 & 0 & 0 \end{bmatrix} \end{aligned} \tag{4.6}$$

where $\mathbf{B}_1 = \mathbf{I}_8$. It is worth noting that real-orthogonal STBCs are constructed by using the above Hurwitz-Radon matrices [99].

In the proposed ST-MBM scheme, after specifying the transmission vectors of the first time slot for each of G transmission groups (4.3), the Hurwitz-Radon matrices are independently exploited for each group as the core STBCs to construct the overall

transmission matrix. For $P_u = T = S$, the rows and columns of the Hurwitz-Radon matrices are considered for T time slots and P_u channel fade realizations, respectively.

Let us introduce the ST-MBM concept for $P_u = T$ with the following example, while the generalized ST-MBM concept for larger channel fade realizations of $P_u > 8$ will be given in the next subsection.

Example: Assume that $P_u = 4$ channel fade realizations are generated in each of $G = 2$ transmission groups, where $T_x = 4$ transmit antennas are equipped with a single ($M_{rf} = 1$) RF mirror. In this setup, spreading the signal transmission takes place in $T = 4$ time slots. For this case, a spectral efficiency of $\eta = 1$ bpcu is achieved, where $G_u = T_x/G = 2$ and $u \in \{1, 2\}$. Suppose that incoming $\eta = 4$ bits of $\{1\,0\,0\,1\}$ are transmitted over $G = 2$ transmission groups, where the first two $\{1\,0\}$ bits are assigned to the first group and the remaining $\{0\,1\}$ bits are assigned to the second group. In the first group, the first $\{1\}$ bit of $\{1\,0\}$ bit sequence activates one of $L_1 = 2$ transmit antennas while the following $\{0\}$ bit selects one of $2^{M_{rf}} = 2$ channel states generated with $M_{rf} = 1$ RF mirror, which corresponds to the first channel state of the second transmit antenna. It can be alternatively stated that the bit sequence of $\{1\,0\}$ specifies the third channel fade realization $(l_1 = 3)$ among $P_1 = L_1 2^{M_{rf}} = 4$ channel fade realizations. Similarly, for the second group, the first $\{0\}$ bit of remaining $\{0\,1\}$ bits activates the first transmit antenna of the second antenna group, where $L_2 = 2$, while the following $\{1\}$ bit determines the second channel state of the corresponding active antenna. In other words, the second $(l_2 = 2)$ out of $P_2 = L_2 2^{M_{rf}} = 4$ channel fade realizations is selected. For the remaining three time slots, we follow the Hurwitz-Radon matrices in (4.5) to obtain a diversity gain. Therefore, transmission matrices of the first and second groups can be given as

$$\mathbf{X}_1 = \overbrace{\underbrace{\begin{bmatrix} 0 & 0 & 1 & 0 \\ 0 & 0 & 0 & 1 \\ -1 & 0 & 0 & 0 \\ 0 & -1 & 0 & 0 \end{bmatrix}}_{1^{st}} \underbrace{\quad}_{2^{nd}}}^{L_1=2}_{l_1=3}, \quad \mathbf{X}_2 = \overbrace{\underbrace{\begin{bmatrix} 0 & 1 & 0 & 0 \\ -1 & 0 & 0 & 0 \\ 0 & 0 & 0 & -1 \\ 0 & 0 & 1 & 0 \end{bmatrix}}_{1^{st}} \underbrace{\quad}_{2^{nd}}}^{L_2=2}_{l_2=2} \tag{4.7}$$

which respectively correspond to $\mathbf{B}_3$ and $\mathbf{B}_2$ in (4.5). Then, the overall transmission matrix, that comprises both $\mathbf{X}_1 \in \mathbb{C}^{T\times P_1}$ and $\mathbf{X}_2 \in \mathbb{C}^{T\times P_2}$, is given as

$$\mathbf{X} = \begin{bmatrix} 0 & 0 & 1 & 0 & 0 & 1 & 0 & 0 \\ 0 & 0 & 0 & 1 & -1 & 0 & 0 & 0 \\ -1 & 0 & 0 & 0 & 0 & 0 & 0 & -1 \\ 0 & -1 & 0 & 0 & 0 & 0 & 1 & 0 \end{bmatrix}. \tag{4.8}$$

We note that the rows and columns of $\mathbf{X} \in \mathbb{C}^{T\times P}$ correspond to time slots and channel fade realizations, respectively. Since the overall transmission matrix is formed by the elements of $\{1, -1, 0\}$ in the baseband, to transmit these elements, a single RF chain is sufficient. Then, as given in Figure 4.1, a cosine carrier signal generated from a local oscillator is supplied to G groups to transmit 1s and -1s. Thus, as the traditional SM/SSK systems [100], the overall ST-MBM system has been designed by using a single RF chain.

4.1.1 Design criteria and transmit diversity analysis

The rank and determinant criteria are commonly used in the design of STBCs to maximize diversity and coding gains. Let us consider the transmit STBC matrix $\mathbf{S}_i$ and the erroneously detected STBC matrix $\mathbf{S}_j$, for $i \neq j$, then transmit diversity gain G_d is evaluated as

$$G_d = \operatorname{rank}\big[(\mathbf{S}_i - \mathbf{S}_j)(\mathbf{S}_i - \mathbf{S}_j)^H\big]. \tag{4.9}$$

The maximum transmit diversity order that can be achieved by any $T \times P_u$ orthogonal STBC is equal to the number of time slots T, which is respectively four and eight for the square STBC matrices given in (4.5) and (4.6). However, since there is only one non-zero element in each row and column of the Hurwitz-Radon matrices, removing any row(s) or column(s) results in a new orthogonal design, which does not violate the orthogonality of the remaining matrix and allows us to achieve any transmit diversity order of $G_d = T$ for $T \leq 8$. In the ST-MBM scheme, since the Hurwitz-Radon matrices are utilized as core STBC matrices, we take the advantage of this unique property and in the same way, can achieve a transmit diversity order of T, where $2 \leq T \leq 8$, by removing the required number of row(s) from the overall ST-MBM transmission matrix. Accordingly, in the ST-MBM scheme, when the transmit signal matrix $\mathbf{X}$ is erroneously detected as $\hat{\mathbf{X}}$, the transmit diversity order of the ST-MBM scheme is given

as:

$$G_d = \operatorname{rank}\left[(\mathbf{X}-\hat{\mathbf{X}})(\mathbf{X}-\hat{\mathbf{X}})^H\right] = T. \tag{4.10}$$

Furthermore, considering the above rank criterion, inserting an all-zero matrix to any STBC matrix, without distorting the integrity of the target matrix, still does not violate the orthogonality of the core STBC, and the newly generated STBC matrix achieves the same transmit diversity as that of the core STBC. This allows us to generalize the ST-MBM scheme for more than eight channel fade realizations ($P_u > 8$), which exceeds the maximum dimensions of the Hurwitz-Radon matrix, and to attain higher spectral efficiency values while still achieving a transmit diversity order of $T \leq 8$. In each transmission group, since $P_u = G_u 2^{M_{rf}} > 8$ is also an integer multiple of 8, to retain the orthogonality of the core STBC, the required number of $T \times 8$ all-zero matrices are added to the core $T \times 8$ STBC matrix, and the corresponding transmission matrix is generated by shifting the core STBC matrix in blocks in accordance with the index of active channel state l_u, where $l_u \in \{1, 2, \ldots, P_u\}$. Therefore, for $P_u > 8$, the overall transmission matrix of uth transmission group, $\mathbf{X}_u \in \mathbb{C}^{T \times P_u}$, can be given as

$$\mathbf{X}_u = \left[\mathbf{0}_8 \ \cdots \ \mathbf{0}_8 \ \mathbf{B}_{l_u} \ \mathbf{0}_8 \ \cdots \ \mathbf{0}_8\right] \tag{4.11}$$

where $\mathbf{0}_8$ is a $T \times 8$ all-zero matrix. In (4.11), $\mathbf{B}_{l_u}$ either corresponds to one of 8×8 Hurwitz-Radon matrices that achieve the maximum transmit diversity for $T = 8$, or it corresponds to a non-square STBC matrix obtained by extracting the required number of row(s) from the considered 8×8 Hurwitz-Radon matrix for $T < 8$. Therefore, the overall ST-MBM transmission matrix $\mathbf{X} \in \mathbb{C}^{T \times P}$, for $P = NP_u$ being the number of all channel fade realizations that comprises of G transmission groups, becomes

$$\mathbf{X} = \left[\mathbf{X}_1 \ \mathbf{X}_2 \ \cdots \ \mathbf{X}_G\right]. \tag{4.12}$$

$\mathbf{X}$ is transmitted over a wireless channel, represented by $\mathbf{H} \in \mathbb{C}^{P \times R_x}$, while experiencing AWGN, characterized by $\mathbf{N}$, whose elements are i.i.d complex Gaussian random variables with $\mathcal{CN}(0, N_0)$ distribution. Therefore, the matrix of received signals is given as

$$\mathbf{Y} = \mathbf{X}\mathbf{H} + \mathbf{N} \tag{4.13}$$

where $\mathbf{Y} \in \mathbb{C}^{T \times R_x}$. Alternatively, the received signals can be represented by the following equivalent model as:

$$\mathbf{y} = \mathbf{h}_\chi + \mathbf{n} = \sum_{u=1}^{G} \mathbf{h}_u + \mathbf{n} \tag{4.14}$$

where $\mathbf{y} \in \mathbb{C}^{TR_x \times 1} = \mathrm{vec}(\mathbf{Y})$, $\mathbf{n} \in \mathbb{C}^{TR_x \times 1} = \mathrm{vec}(\mathbf{N})$, $\mathbf{h}_\chi \in \mathbb{C}^{TR_x \times 1} = \mathrm{vec}(\mathbf{XH})$ and $\mathbf{h}_u \in \mathbb{C}^{TR_x \times 1}$ is a column vector that contains channel fade realizations corresponding to non-zero elements of $\mathbf{X}_u$, the transmission matrix of the uth transmission group.

At the receiver side, assuming P-CSI, the equivalent signal model of (4.14) is considered and an ML detector is used to achieve the optimum BER performance as

$$\left(\hat{l}_1, \hat{l}_2, \ldots, \hat{l}_G\right) = \arg \min_{l_1, l_2, \ldots, l_G} \left\| \mathbf{y} - \sum\nolimits_{u=1}^{N} \mathbf{h}_u \right\|^2. \tag{4.15}$$

Then, the overall computational complexity of the ML detector (4.15) is evaluated in terms of real multiplications as $\sim \mathcal{O}(TR_x 2^{\eta T+1})$, since each of $2^{\eta T}$ decision metric calculations requires $2TR_x$ real multiplications for each $\|\cdot\|^2$ operation.

which is always T for $T \times P_u$ dimensional STBCs.

4.2 Performance and Capacity Analyses

In this section, based on our system model of Section 4.1, we present error performance and capacity analyses for the proposed ST-MBM scheme.

In the ST-MBM scheme, correlated and uncorrelated fading channels are considered and the correlated channel matrix $\mathbf{H}$ is modeled through the uncorrelated Rayleigh fading channel matrix $\tilde{\mathbf{H}} \in \mathbb{C}^{P \times R_x}$, whose elements are i.i.d. complex Gaussian random variables with distribution of $\mathcal{CN}(0,1)$, as

$$\mathbf{H} = \mathbf{R}_t^{1/2} \tilde{\mathbf{H}} \mathbf{R}_r^{1/2}. \tag{4.16}$$

where $\mathbf{R}_t$ and $\mathbf{R}_r$ denote transmit and receive correlation matrices with dimensions of $P \times P$ and $R_x \times R_x$, respectively.

In this study, the transmit correlation matrix $\mathbf{R}_t$ is determined by considering two different correlation models: the Kronecker model [101] and the equicorrelation model [30]. The Kronecker model is used for the correlation among the fades of different

transmit antennas, while the equicorrelation model is considered for the correlation among the channel states of each transmit antenna. $\mathbf{R}_t$ is given as

$$\mathbf{R}_t = \begin{bmatrix} 1 & r_b & \cdots & r_b & r_a & r_a & \cdots & r_a & \cdots & r_a^{T_x-1} & r_a^{T_x-1} & \cdots & r_a^{T_x-1} \\ r_b & 1 & \cdots & r_b & r_a & r_a & \cdots & r_a & \cdots & r_a^{T_x-1} & r_a^{T_x-1} & \cdots & r_a^{T_x-1} \\ \vdots & \vdots & \ddots & \vdots & \vdots & \vdots & \ddots & \vdots & \vdots & \vdots & \vdots & \ddots & \vdots \\ r_b & r_b & \cdots & 1 & r_a & r_a & \cdots & r_a & \cdots & r_a^{T_x-1} & r_a^{T_x-1} & \cdots & r_a^{T_x-1} \\ — & — & — & — & — & — & — & — & — & — & — & — & — \\ r_a & r_a & \cdots & r_a & 1 & r_b & \cdots & r_b & \cdots & r_a^{T_x-2} & r_a^{T_x-2} & \cdots & r_a^{T_x-2} \\ r_a & r_a & \cdots & r_a & r_b & 1 & \cdots & r_b & \cdots & r_a^{T_x-2} & r_a^{T_x-2} & \cdots & r_a^{T_x-2} \\ \vdots & \vdots & \ddots & \vdots & \vdots & \vdots & \ddots & \vdots & \vdots & \vdots & \vdots & \ddots & \vdots \\ r_a & r_a & \cdots & r_a & r_b & r_b & \cdots & 1 & \cdots & r_a^{T_x-2} & r_a^{T_x-2} & \cdots & r_a^{T_x-2} \\ — & — & — & — & — & — & — & — & — & — & — & — & — \\ \vdots & \vdots & \vdots & \vdots & \vdots & \vdots & \vdots & \vdots & \vdots & \vdots & \vdots & \vdots & \vdots \\ — & — & — & — & — & — & — & — & — & — & — & — & — \\ r_a^{T_x-1} & r_a^{T_x-1} & \cdots & r_a^{T_x-1} & r_a^{T_x-2} & r_a^{T_x-2} & \cdots & r_a^{T_x-2} & \cdots & 1 & r_b & \cdots & r_b \\ r_a^{T_x-1} & r_a^{T_x-1} & \cdots & r_a^{T_x-1} & r_a^{T_x-2} & r_a^{T_x-2} & \cdots & r_a^{T_x-2} & \cdots & r_b & 1 & \cdots & r_b \\ \vdots & \vdots & \ddots & \vdots & \vdots & \vdots & \ddots & \vdots & \vdots & \vdots & \vdots & \ddots & \vdots \\ r_a^{T_x-1} & r_a^{T_x-1} & \cdots & r_a^{T_x-1} & r_a^{T_x-2} & r_a^{T_x-2} & \cdots & r_a^{T_x-2} & \cdots & r_b & r_b & \cdots & 1 \end{bmatrix} \tag{4.17}$$

where r_a and r_b are the correlation coefficients between the transmit antennas and channel states, respectively. On the other hand, the receive correlation matrix $\mathbf{R}_r$ is characterized by using the Kronecker model [101] and given as

$$\mathbf{R}_r = \begin{bmatrix} 1 & r_a & r_a^2 & \cdots & r_a^{R_x-1} \\ r_a & 1 & r_a & \cdots & r_a^{R_x-2} \\ r_a^2 & r_a & 1 & \cdots & r_a^{R_x-3} \\ \vdots & \vdots & \vdots & \ddots & \vdots \\ r_a^{R_x-1} & r_a^{R_x-2} & r_a^{R_x-3} & \cdots & 1 \end{bmatrix}. \tag{4.18}$$

It is worth noting that $0 < r_a, r_b < 1$.

4.2.1 Performance analysis

In this subsection, the theoretical ABEP performance of the ST-MBM scheme is analyzed. Considering a commonly used upper bounding technique [102], the ABEP of the system is given as

$$P_b \leq \frac{1}{2^{\eta T}} \sum_{\mathbf{X}} \left[\frac{1}{\eta T} \sum_{\hat{\mathbf{X}}} Pr\left(\mathbf{X} \to \hat{\mathbf{X}}\right) e\left(\mathbf{X}, \hat{\mathbf{X}}\right) \right] \tag{4.19}$$

where $Pr(\mathbf{X} \to \hat{\mathbf{X}})$ is the PEP and $e(\mathbf{X}, \hat{\mathbf{X}})$ is the number of bit errors occurred for the corresponding pairwise error event.

In order to obtain the PEP of the ST-MBM scheme, first, conditional PEP (CPEP) is derived, which can be given in terms of the Q-function as follows

$$P_r\left(\mathbf{X}\to\hat{\mathbf{X}}|\mathbf{H}\right)=Q\left(\sqrt{\frac{\Lambda}{2N_0}}\right) \tag{4.20}$$

where Λ is given, for $\gamma=1/N_0$, as

$$\Lambda=\left\|\gamma\left(\mathbf{X}-\hat{\mathbf{X}}\right)\mathbf{H}\right\|^2. \tag{4.21}$$

Then, for the following difference matrix

$$\mathbf{\Delta}=\left(\mathbf{X}-\hat{\mathbf{X}}\right)^H\left(\mathbf{X}-\hat{\mathbf{X}}\right) \tag{4.22}$$

and $\mathbf{R}_s=\mathbf{R}_r\otimes\mathbf{R}_t$, Λ is rewritten in quadratic form as

$$\begin{aligned}\Lambda&=\left\|\gamma\left(\mathbf{X}-\hat{\mathbf{X}}\right)\mathbf{H}\right\|^2\\&=\mathrm{Tr}\left(\mathbf{H}^H\left(\mathbf{X}-\hat{\mathbf{X}}\right)^H\left(\mathbf{X}-\hat{\mathbf{X}}\right)\mathbf{H}\right)\\&=\mathrm{vec}(\mathbf{H}^H)^H(\mathbf{I}_{R_x}\otimes\mathbf{\Delta})\mathrm{vec}(\mathbf{H}^H)\\&=\mathrm{vec}(\tilde{\mathbf{H}}^H)^H(\mathbf{R}_s{}^{1/2})^H(\mathbf{I}_{R_x}\otimes\mathbf{\Delta})\mathbf{R}_s{}^{1/2}\mathrm{vec}(\tilde{\mathbf{H}}^H).\end{aligned} \tag{4.23}$$

Substituting (4.23) into the following alternative expression

$$Q(x)=\frac{1}{\pi}\int_0^{\pi/2}\exp\left(-\frac{x^2}{2\sin^2\theta}\right)d\theta \tag{4.24}$$

and considering

$$\mathbf{\Gamma}=(\mathbf{R}_s{}^{1/2})^H(\mathbf{I}_{R_x}\otimes\mathbf{\Delta})\mathbf{R}_s{}^{1/2} \tag{4.25}$$

the CPEP of the system (4.20) is given in a positive semidefinite quadratic form as

$$P_r\left(\mathbf{X}\to\hat{\mathbf{X}}|\mathbf{H}\right)=\frac{1}{\pi}\int_0^{\pi/2}\exp\left(-\gamma\frac{\mathrm{vec}(\tilde{\mathbf{H}}^H)^H\mathbf{\Gamma}\mathrm{vec}(\tilde{\mathbf{H}}^H)}{4\sin^2\theta}\right)d\theta \tag{4.26}$$

Then, the PEP of the system is derived by averaging (4.26) over the channel matrix $\mathbf{H}$ through the MGF approach as follows

$$P_r\left(\mathbf{X}\to\hat{\mathbf{X}}\right)=\frac{1}{\pi}\int_0^{\pi/2}\mathcal{M}_{\mathbf{\Gamma}}\left(-\frac{\gamma}{4\sin^2\theta}\right)d\theta. \tag{4.27}$$

The MGF of (4.27) is evaluated using the expression for the MGF of a quadratic form $\mathbf{z}^H\mathbf{Q}\mathbf{z}$, involving the vector $\mathbf{z}$ and the Hermitian matrix $\mathbf{Q}$, given in [103] as

$$\mathcal{M}(s)=\frac{\exp[s\bar{\mathbf{z}}^H\mathbf{Q}(\mathbf{I}-s\mathbf{K}_{\mathbf{z}}\mathbf{Q})^{-1}\bar{\mathbf{z}}]}{(\mathbf{I}-s\mathbf{K}_{\mathbf{z}}\mathbf{Q})} \tag{4.28}$$

where $\bar{\mathbf{z}}$ is the mean vector and $\mathbf{K_z}$ is the covariance matrix that is given as

$$\mathbf{K_z} = E\left\{\mathbf{z}^H\mathbf{z}\right\} - \bar{\mathbf{z}}^H\bar{\mathbf{z}}. \tag{4.29}$$

Since $\mathrm{vec}(\tilde{\mathbf{H}}^H)$ is a complex Gaussian channel vector whose elements are distributed with zero mean and unit variance, for $\mathbf{z} = \mathrm{vec}(\tilde{\mathbf{H}}^H)$ and $\mathbf{Q} = \mathbf{\Gamma}$, the mean vector and the covariance matrix of $\mathrm{vec}(\tilde{\mathbf{H}}^H)$ respectively become $\bar{\mathbf{z}} = \overline{\mathrm{vec}(\tilde{\mathbf{H}}^H)} = 0$ and $\mathbf{K_z} = \mathbf{I}_{PR_x}$. Therefore, the exact PEP of the ST-MBM scheme is calculated from the following integral

$$P_r\left(\mathbf{X} \to \hat{\mathbf{X}}\right) = \frac{1}{\pi}\int_0^{\pi/2} \det\left[\mathbf{I}_{PR_x} + \frac{\gamma}{4\sin^2\theta}\mathbf{\Gamma}\right]^{-1} d\theta. \tag{4.30}$$

It is worth noting that (4.30) can be easily calculated by numerical integration. Also, a closed form upper-bound expression for (4.30) is obtained by letting $\theta = \frac{\pi}{2}$ as

$$P_r\left(\mathbf{X} \to \hat{\mathbf{X}}\right) \leq \frac{1}{2}\det\left(\mathbf{I}_{PR_x} + \frac{\gamma}{4}\mathbf{\Gamma}\right)^{-1}. \tag{4.31}$$

4.2.2 Capacity analysis

The amount of information conveyed between the transmission vector $\mathbf{x}$ and the received vector $\mathbf{y}$ is defined as the mutual information and is given for the MIMO channel matrix $\mathbf{H}$ as

$$I(\mathbf{y};\mathbf{x}) = \mathbb{E}_{\mathbf{H}}\Big\{H(\mathbf{y}|\mathbf{H}) - H(\mathbf{y}|\mathbf{x},\mathbf{H})\Big\}. \tag{4.32}$$

However, for the ST-MBM scheme, when the equivalent signal model (4.14) of the ST-MBM is considered, since incoming information bits modulate channel elements and carry no information with an ordinary modulation, the mutual information is defined as amount of information conveyed between the received signal $\mathbf{y}$ and the channel vector $\mathbf{h}\chi$ [6], and can be given as follows

$$\begin{aligned} I(\mathbf{y};\mathbf{h}\chi) &= H(\mathbf{y}) - H(\mathbf{y}|\mathbf{h}\chi) \\ &= \frac{1}{T}\sum_{\mathbf{h}\chi}\int_{-\infty}^{\infty}\cdots\int_{-\infty}^{\infty} P(\mathbf{y}|\mathbf{h}\chi)P(\mathbf{h}\chi) \times \log_2\left(\frac{P(\mathbf{y}|\mathbf{h}\chi)}{\sum_{\hat{\mathbf{h}}\chi} P(\mathbf{y}|\hat{\mathbf{h}}\chi)P(\hat{\mathbf{h}}\chi)}\right) d\mathbf{y}. \end{aligned} \tag{4.33}$$

The conditional probability density function (p.d.f.) of the equivalent received signal vector of (4.14) is given by

$$P(\mathbf{y}|\mathbf{h}\chi) = \frac{1}{(\pi N_0)^{TR_x}}\exp\left(-\frac{\|\mathbf{y} - \mathbf{h}\chi\|^2}{N_0}\right). \tag{4.34}$$

Since all possible $\mathbf{h}_\chi$ are equiprobable, we have $P(\mathbf{h}_\chi) = 1/2^{\eta T}$. Substituting (4.34) and $P(\mathbf{h}_\chi) = 1/2^{\eta T}$ into (4.33), the mutual information of the ST-MBM scheme using T time slots, $I(\mathbf{y}; \mathbf{h}_\chi)$, results as

$$
\begin{aligned}
I(\mathbf{y};\mathbf{h}\chi) = & \\
&= \frac{1}{T}\left(\eta T - \left[\frac{1}{2^{\eta T}} \times \sum_{\mathbf{h}\chi} \frac{1}{(\pi N_0)^{TR_x}} \int_{\mathbf{y}\in\mathbb{C}^{TR_x}} \exp\left(-\frac{\|\mathbf{y}-\mathbf{h}\chi\|^2}{N_0}\right)\right.\right. \\
&\qquad \left.\left. \times \log_2\left(\sum_{\substack{\hat{\mathbf{h}}\chi \\ \hat{\mathbf{h}}\chi\neq\mathbf{h}\chi}} \exp\left(\frac{\|\mathbf{y}-\mathbf{h}\chi\|^2 - \|\mathbf{y}-\hat{\mathbf{h}}\chi\|^2}{N_0}\right)\right) d\mathbf{y}\right]\right) \\
&= \frac{1}{T}\left(\eta T - \left[\frac{1}{2^{\eta T}} \times \sum_{\mathbf{h}\chi} \frac{1}{(\pi N_0)^{TR_x}} \int_{\mathbf{y}\in\mathbb{C}^{TR_x}} \exp\left(-\frac{\|\mathbf{y}-\mathbf{h}\chi\|^2}{N_0}\right)\right.\right. \\
&\qquad \left.\left. \times \log_2\left[1 + \sum_{\substack{\hat{\mathbf{h}}\chi \\ \hat{\mathbf{h}}\chi\neq\mathbf{h}\chi}} \exp\left(\frac{\|\mathbf{y}-\mathbf{h}\chi\|^2 - \|\mathbf{y}-\hat{\mathbf{h}}\chi\|^2}{N_0}\right)\right] d\mathbf{y}\right]\right)
\end{aligned}
\tag{4.35}
$$

where the factor of $1/T$ comes from T channel uses. Then, using the Jensen's inequality and applying some algebraic manipulations [104], a lower bound is obtained for $I(\mathbf{y}; \mathbf{h}\chi)$ as

$$
I(\mathbf{y};\mathbf{h}\chi) \geq \frac{1}{T}\left(\eta T + \frac{1}{2^{\eta T}} \times \sum_{\mathbf{h}\chi} \sum_{\substack{\hat{\mathbf{h}}\chi \\ \hat{\mathbf{h}}\chi\neq\mathbf{h}\chi}} \exp\left(\frac{-\|\mathbf{h}\chi - \hat{\mathbf{h}}\chi\|^2}{4N_0}\right)\right]\right). \tag{4.36}
$$

4.3 Simulation Results

In this section, BER performance of the ST-MBM scheme is investigated through comprehensive computer simulations. For different spectral efficiency values and transmit diversity gains, the BER performance and mutual information analysis of the ST-MBM scheme are evaluated and its superior error performance over existing systems are shown. All computer simulations are depicted as a function of the received energy per bit to noise ratio (E_b/N_0) for $R_x = 4$.

In Figure 4.2, the theoretical ABEP performance of ST-MBM schemes designed for $T = 2$ and $T = 3$ is depicted for correlated and uncorrelated fading conditions. The results show that the theoretical ABEP results of the ST-MBM scheme are consistent with the computer simulation results at high E_b/N_0 values. Also, increasing

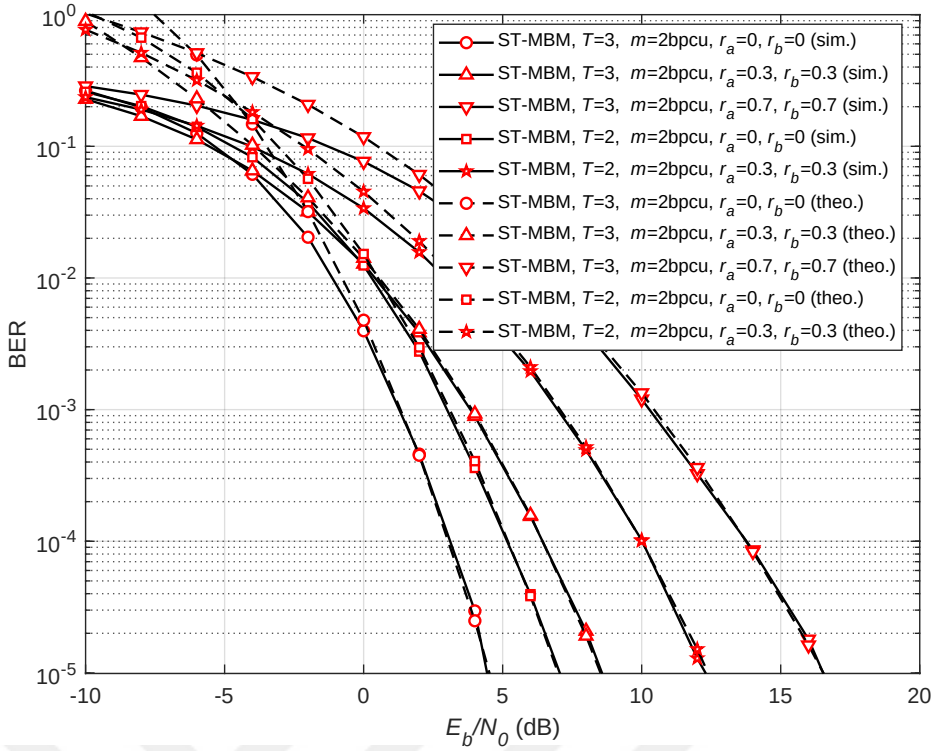

Figure 4.2 : Theoretical and simulation results of the ST-MBM scheme for $T = 2$ and $T = 3$ under different channel correlation values.

correlation coefficients r_a and r_b apparently results in noticeable performance degradation and should be carefully monitored by the system designer.

To show the effect of different transmit diversity gains at a certain spectral efficiency value, in Figure 4.3, the BER performance of the ST-MBM scheme achieving a transmit diversity order of T with and without channel estimation errors, is provided. For each case, to achieve the same spectral efficiency value of $\eta = 2$ bpcu, a total of $P = 2^{\eta T}$ channel fade realizations are considered for $G = 2$ transmission groups, where $P = NP_u$. Then, to analyze the effect of imperfect channel state knowledge on the BER performance of the proposed ST-MBM scheme, the estimated channel matrix is assumed to be $\hat{\mathbf{H}} = \mathbf{H} + \mathbf{E}$, where $\mathbf{E}$ is the matrix of channel estimation errors whose entries are i.i.d. Gaussian random variables with the distribution of $\mathcal{CN}(0, \sigma_E^2)$. Thus, the entries of the overall estimated channel matrix $\hat{\mathbf{H}}$ are assumed to be distributed with $\mathcal{CN}(0, 1 + \sigma_E^2)$. The shown results clearly demonstrate the superior performance of the ST-MBM scheme with increasing transmit diversity gains, which is significantly beyond the performance of the SSK scheme with unity transmit diversity gain. Moreover, it can be deduced from Figure 4.3 that the ST-MBM schemes achieving Tth order transmit diversity are more robust to channel state errors at high

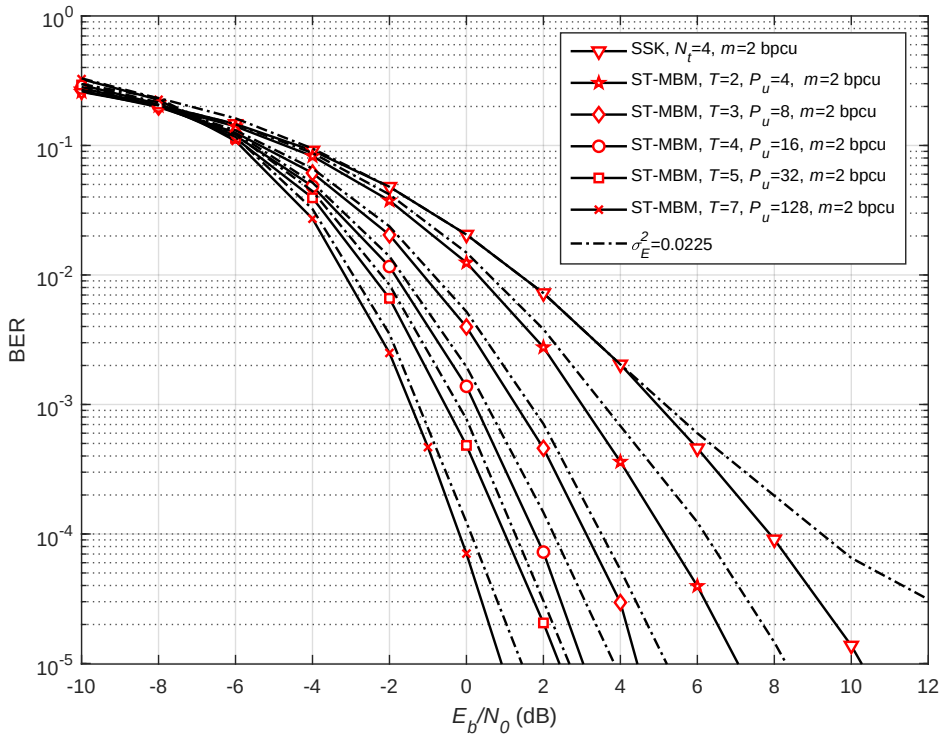

Figure 4.3 : BER performance of the SSK and ST-MBM schemes for $T \in \{2, 3, 4, 5, 7\}$ and $\eta = 2$ bpcu with perfect and imperfect channel estimation.

E_b/N_0 values compared to the traditional SSK scheme. We also observe from Figure 4.3 that the proposed ST-MBM scheme would be suitable for future ultra-reliable communication systems that require high diversity gains.

In Figure 4.4, BER performance of the ST-MBM scheme with increasing spectral efficiency values is investigated. It can be observed from this figure that unlike the traditional MIMO systems, as the spectral efficiency value increases, the error performance gradually improves. However, the system performance appears to be saturated at spectral efficiency values of 6 and 7 bpcu, which shows a similar behavior with the simulation results of the classical SSK/MBM schemes that saturate at high spectral efficiency values [28]. This phenomenon shows that as the ST-MBM scheme creates a virtual constellation that has randomly distributed elements while attaining transmit diversity gains, it retains the inherent maximum capacity achieving property of the classical SSK scheme.

In Figure 4.5, for $\eta = 6$ bpcu, the error performance of the ST-MBM scheme is compared with the classical SSK scheme and the existing state-of-the-art STBC-based systems that achieve second order transmit diversity gain. The significant performance improvement of the ST-MBM scheme over common STBC-based systems including

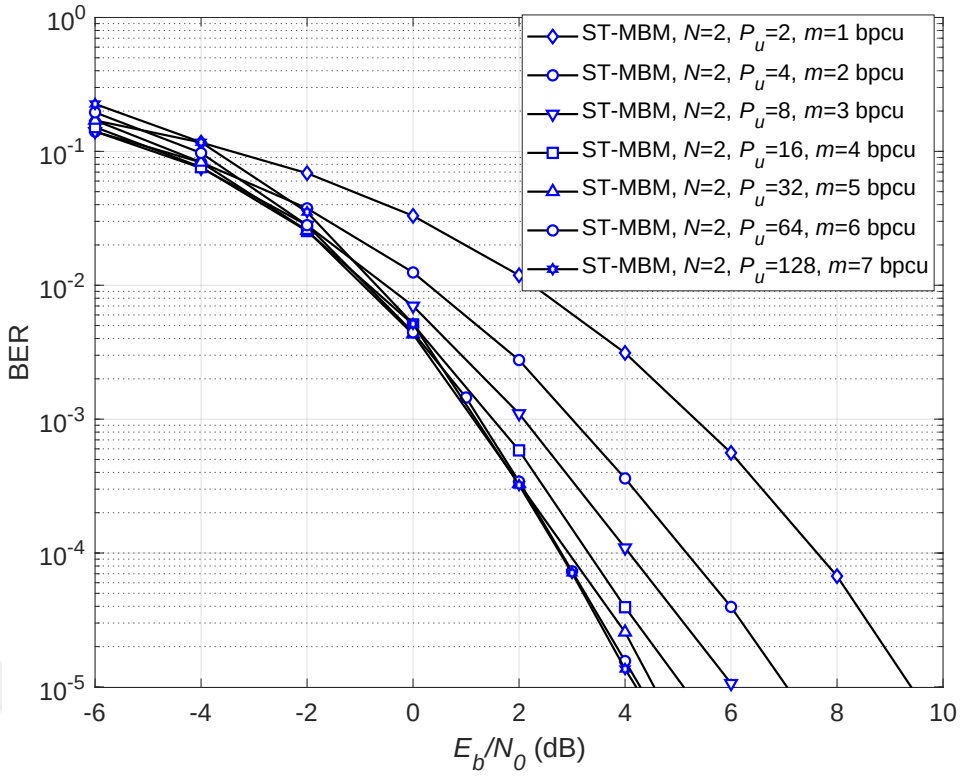

Figure 4.4 : BER performance of the ST-MBM scheme for $T = 2$ and $\eta = 1, 2, 3, 4, 5, 6, 7$ bpcu.

Alamouti's STBC [33], STBC-SM [105] and space-time quadrature SM (ST-QSM) [106] is clearly observed. Furthermore, we compare the performance of the proposed scheme with recently developed STBC-based MBM systems including space-time channel modulation (STCM) [16] and USTLD-STCM [17] to achieve $\eta = 6$ bpcu. In this comparison, $M_{rf} = 2$ RF mirrors are utilized with 16-QAM signal constellation, while in the ST-MBM scheme, $G = 2$ transmission groups with $P_u = 64$ channel fade realizations are used without ordinary modulation. Computer simulation results show that at a BER value of 10^{-5}, the ST-MBM scheme exhibits 3.5 and 1.5 dB gains in required E_b/N_0 compared to STCM [28] and USTLD-STCM [32], respectively.

However, for the same spectral efficiency, when STCM employs $M_{rf} = 4$ RF mirrors with QPSK modulation, its BER performance significantly improves, while it is still 0.5 dB behind the ST-MBM scheme at the BER value of 10^{-5}. Compared to STCM, the proposed ST-MBM scheme achieves almost 80% reduction in transceiver complexity, where the decoding complexity of STCM with two RF chains as well as in-phase and quadrature (I/Q) modulation, in terms of real multiplications, is $\sim \mathcal{O}(10TR_x2^{\eta T})$ while the corresponding value is $\sim \mathcal{O}(TR_x2^{\eta T+1})$ for the ST-MBM

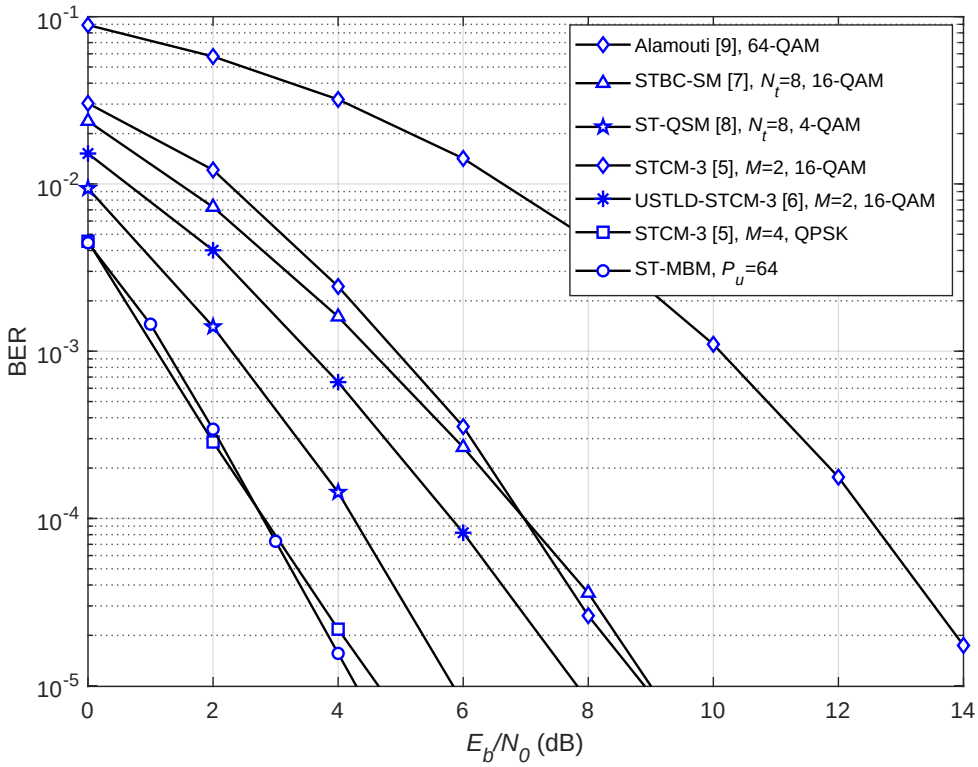

Figure 4.5 : BER performance of ST-MBM, STCM, USTLD-STCM, STBC-SM, ST-QSM, Alamouti's STBC and SSK schemes for $\eta = 6$ bpcu.

scheme. In conclusion, we note that the proposed ST-MBM scheme provides a remarkable reduction in both transmitter and receiver complexity by eliminating the need for multiple RF chains and I/Q modulation and enabling a significant reduction in the number of operations required for ML detection.

In Figures 4.6 and 4.7, the mutual information curves of the ST-MBM scheme that achieves a Tth order transmit diversity gain, is depicted for different spectral efficiency values. Figure 4.6 shows that as E_b/N_0 increases, each curve converges to its attainable mutual information value. Additionally, in Figure 4.7, for spectral efficiency values of $\eta = 2$, 3 and 4 bpcu, the mutual information results of the ST-MBM scheme for different transmit diversity orders are compared. The mutual information results of the ST-MBM scheme are compared at $\eta = 2$ bpcu, when T varies from two to five, while at $\eta = 3$ and 4 bpcu, transmit diversity orders of three and four are considered. Although the mutual information of the ST-MBM scheme is scaled with the transmit diversity order of T due to the number of channel uses (4.35), the results reveal that as the transmit diversity order, T, increases the system converges faster to its achievable mutual information.

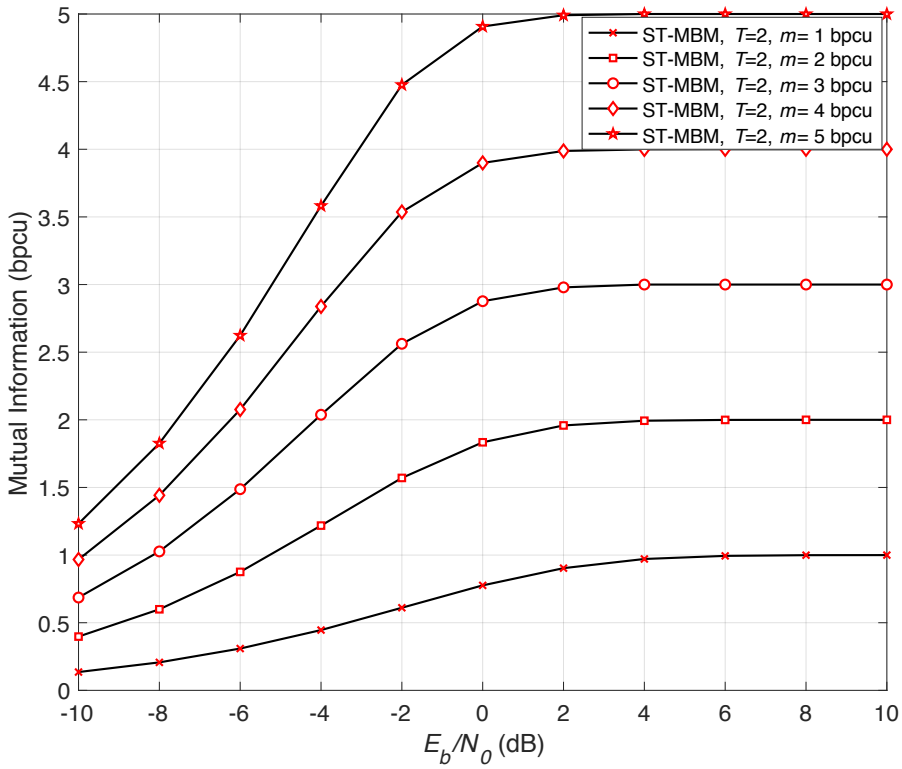

Figure 4.6 : Mutual information of the ST-MBM scheme with varying spectral efficiencies for $T = 2$.

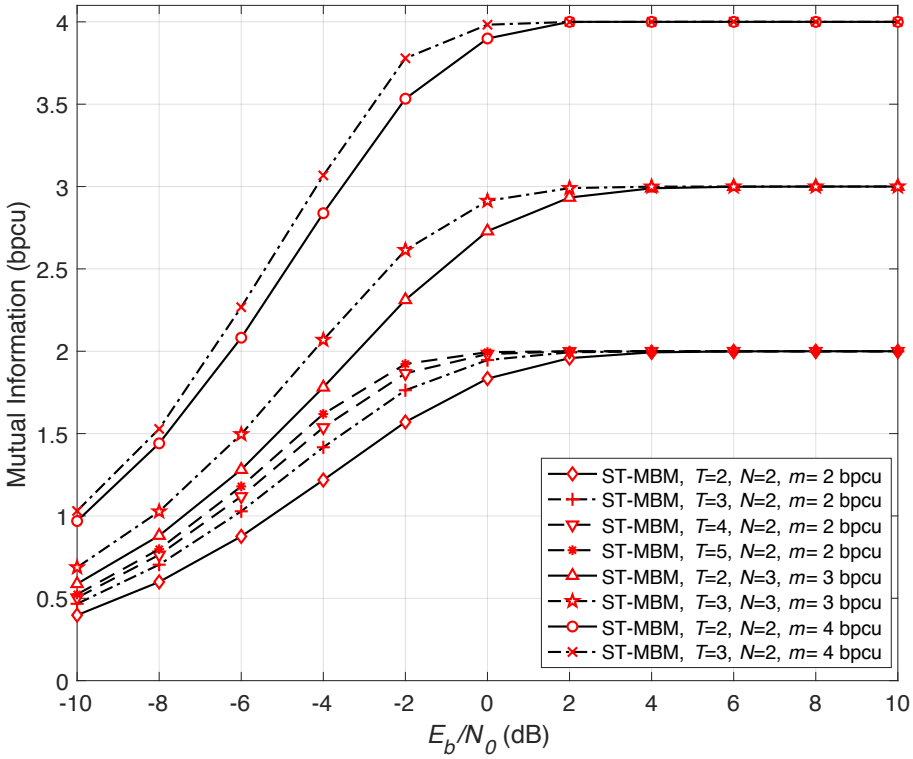

Figure 4.7 : Mutual information of the ST-MBM scheme with increasing transmit diversity orders for $\eta = 2$, 3 and 4 bpcu.

4.4 Conclusion

In this chapter, we have presented a general framework for space-time coded IM systems and introduced the ST-MBM scheme as the first STBC-based transmission scheme that uses a single RF chain at the transmitter while achieving various transmit diversity gains through MBM and time dispersion. Theoretical error performance analysis of the ST-MBM scheme for correlated and uncorrelated channel fadings has been investigated. Additionally, a lower bound has been derived for the mutual information of the ST-MBM scheme. Furthermore, through extensive computer simulations, the superior error performance of the proposed ST-MBM scheme with significantly lower decoding complexity over existing STBC-based transmission schemes has been demonstrated. The flexibility to achieve higher spectral efficiencies and various transmit diversity gains makes the ST-MBM scheme highly suitable for beyond 5G and URLLC applications.

5. CIRCULAR SPACE-TIME BLOCK CODE DESIGN FOR ULTRA-RELIABLE IM SCHEMES

In this chapter, a novel MBM-based CSTBC technique, *CSTBC-IM*, which achieves numerous orders of transmit diversity gains, is proposed as an ultra-reliable IM concept. In the proposed CSTBC-IM scheme, the MBM concept is considered for both MIMO and SIMO system configurations. Moreover, the theoretical error performance analysis of the proposed CSTBC-IM schemes is performed and an upper bound expression is obtained for ABEP. Through extensive computer simulations, the flexibility of the CSTBC-IM schemes that provide various orders of transmit diversity gains and achieve high spectral efficiency values, are discussed. Furthermore, their superior error performance over the reference IM techniques, such as STCM [28], STBC-SM [105], ST-QSM, USTLD-STCM [32] and classical Alamouti's STBC [33], is shown.

The rest of the chapter is organized as follows. In Section 5.1, the system models of the proposed CSTBC-IM schemes are introduced. The analytical error performance analysis is given in Section 5.2. In Section 5.3, the numerical results are discussed and the chapter is concluded in Section 5.4.

5.1 Circular Space-Time Code Design

In the last decade, several STBC-based IM schemes [28, 105, 106], which are inspired by traditional STBC concepts [99], have been designed to provide a second-order transmit diversity gain for plain IM schemes. In this study, a novel STBC technique is designed considering the structure of a circulant matrix in which each row contains the same elements as those of the first row and is determined by the circular shift of the previous row.

Suppose that $\mathbf{B}$ is a circulant matrix with dimensions $T \times P$, and it is formed by the elements c_i, for $i \in \{1, 2, \ldots, P\}$, as follows:

$$\mathbf{B} = \begin{bmatrix} c_1 & c_2 & \cdots & c_T & \cdots & c_{P-1} & c_P \\ c_P & c_1 & \cdots & c_{T-1} & \cdots & c_{P-2} & c_{P-1} \\ \vdots & \ddots & \ddots & \ddots & \ddots & \ddots & \vdots \\ c_{P-T+2} & \cdots & c_P & c_1 & \cdots & c_{P-T} & c_{P-T+1} \end{bmatrix}. \tag{5.1}$$

Let $\mathbf{B}$ be an STBC transmission matrix and T denotes the number of time intervals. Then, when the rank criterion [99], one of the most common STBC design principles, is considered to maximize the transmit diversity, for $\mathbf{B}$ and $\hat{\mathbf{B}}$ respectively symbolizing the transmitted and erroneously detected circular STBC matrices, the transmit diversity gain is calculated by [99]:

$$G_d = \min_{\mathbf{B}, \hat{\mathbf{B}}} \operatorname{rank}\left(\left(\mathbf{B} - \hat{\mathbf{B}}\right) \left(\mathbf{B} - \hat{\mathbf{B}}\right)^{\mathrm{H}} \right). \tag{5.2}$$

According to our exhaustive numerical tests, we reveal that when the circular $\mathbf{B}$ matrix is sufficiently sparse with a single non-zero element in each row whose position is determined by circularly shifting the previous row by one unit, it is possible to obtain a Tth order transmit diversity gain, if the following row/column ratio is satisfied:

$$r = \frac{T}{P} \leq 0.5. \tag{5.3}$$

Based on (5.1), this allows us to design transmission schemes that are highly flexible and achieve numerous orders of transmit diversity gains.

In our proposed design, we assume that s is the single non-zero element in each row of the circular STBC matrix $\mathbf{B}$, which stands for an M-PSK/QAM symbol. Moreover, the $r \leq 0.5$ is satisfied to obtain a transmit diversity order $G_d = T$.

Since the circular STBC concept requires a sparse matrix with a single non-zero element in each row or column, IM schemes are the most suitable systems to be adapted. Therefore, we combine the recent MBM transmission schemes [30, 90] with the circular STBC concept and propose a family of MBM-based CSTBC-IM schemes, including CSTBC-SM, CSTBC-MIMO, CSTBC-SIMO and CSTBC-SSK schemes, which will be introduced in the subsequent subsections.

In general, in the proposed CSTBC-IM schemes, the transmission is performed in T time intervals and a system configuration with T_x transmit and R_x receive antennas is

considered. Moreover, each transmit antenna is assumed to be surrounded by M_{rf} RF mirrors that create $P = 2^{M_{rf}}$ channel state realizations for each of those T_x antennas, where for each setup, $r \leq 0.5$ is ensured. Then, for each CSTBC-IM scheme, the incoming information bits determine the transmission vector of the first time slot, where it contains only one non-zero entry as in classical IM schemes [15]. Then, to construct the overall transmission matrix, the remaining time intervals follow the structure of a circular matrix (5.1).

5.1.1 CSTBC-SIMO and CSTBC-SSK

In this subsection, the CSTBC-SIMO and CSTBC-SSK transmission schemes are proposed, where the circular STBC concept is combined with the SIMO-MBM [30] transmission scheme to attain a Tth order transmit diversity gain. In the CSTBC-SIMO scheme, one transmit antenna ($T_x = 1$) with M_{rf} RF mirrors is considered, where the incoming M_{rf} bits select the index of the effective channel state out of $P = 2^{M_{rf}}$ channel state realizations and $\log_2 M$ bits determine a modulated symbol from M-PSK/QAM constellation to transmit through this selected channel state. Therefore, the spectral efficiency of the CSTBC-SIMO scheme in bits per channel use (bpcu) is given by

$$\eta_{SIMO} = \frac{M_{rf} + \log_2 M}{T} \quad \text{[bpcu]}. \tag{5.4}$$

In the CSTBC-SIMO scheme, the incoming ηT information bits determine the transmission vector of the first time interval, then, the overall transmission matrix is constructed by circular shifting of this transmission vector. For s being the M-PSK/QAM symbol and l being the index of the selected channel state of the first time interval, where $l \in \{1, 2, \ldots, P\}$, the overall transmission matrix $\mathbf{X} \in \mathbb{C}^{T \times P}$ of CSTBC-SIMO can be given as

$$\mathbf{X} = \begin{bmatrix} 0 & \ldots & 0 & \overbrace{s}^{l} & 0 & \ldots & 0 & 0 & 0 & 0 \\ 0 & 0 & \cdots & 0 & s & 0 & \cdots & 0 & 0 & 0 \\ \vdots & \ddots & \ddots & \ddots & \ddots & \ddots & \ddots & \ddots & \ddots & \vdots \\ 0 & 0 & \cdots & 0 & 0 & 0 & s & 0 & \cdots & 0 \end{bmatrix}. \tag{5.5}$$

The same signal transmission model as that of the CSTBC-SIMO scheme is also considered for the CSTBC-SSK scheme. However, unlike CSTBC-SIMO, instead of a modulated M-PSK/QAM signal, a cosine signal ($s = 1$) is transmitted over the effective channel state of each time interval.

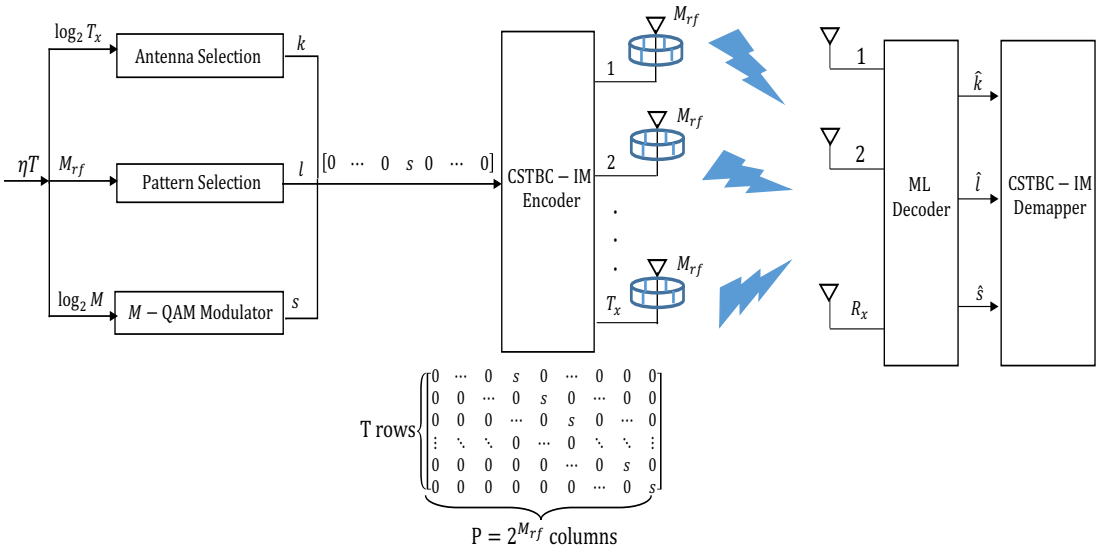

Figure 5.1 : Block diagram of the CSTBC-SM scheme.

5.1.2 CSTBC-SM and CSTBC-MIMO

In this subsection, to improve the spectral efficiency of the CSTBC-SIMO and CSTBC-SSK schemes, the proposed circular STBC concept is generalized for MIMO system configurations, and CSTBC-SM and CSTBC-MIMO transmission schemes are introduced.

The block diagram of the CSTBC-SM scheme is given in Figure 5.1. In CSTBC-SM scheme, the incoming ηT bits determine the indices of both the active antenna and its effective channel state, as well as a modulated symbol from M-PSK/QAM constellations to be transmitted through this effective channel state. Therefore, the spectral efficiency of the CSTBC-SM scheme is given as

$$\eta_{SM} = \frac{M_{rf} + \log_2 T_x + \log_2 M}{T} \quad \text{[bpcu]}. \tag{5.6}$$

In the CSTBC-SM scheme, the incoming $\log_2 T_x$, M_{rf} and $\log_2 M$ bits determine the indices of an active antenna k, its corresponding channel state l and a M-PSK/QAM symbol s, respectively. Then, the transmission vector of the first transmission interval $\mathbf{x}_1 \in \mathbb{C}^{1\times PT_x}$ is constructed as:

$$\mathbf{x}_1 = \big[\underbrace{0\ 0\ \cdots\ 0}_{1}\ \cdots\ \underbrace{0\ \cdots\ 0\ \overbrace{s}^{l}\ 0\ \cdots\ 0}_{k}\ \cdots\ \underbrace{0\ 0\ \cdots\ 0}_{T_x}\big]. \tag{5.7}$$

where $k \in \{1,2,\cdots,T_x\}$ and $l \in \{1,2,\cdots,P\}$. Then, as to CSTBC-SIMO and CSTBC-SSK schemes, for the remaining $T-1$ time intervals, the structure of a circular matrix is followed and the overall transmission matrix $\mathbf{X} \in \mathbb{C}^{T\times PT_x}$ of the

CSTBC-SM scheme is constructed as

$$\mathbf{X} = \begin{bmatrix} 0 & 0 & \cdots & 0 & \cdots & 0 & \cdots & 0 & s & 0 & \cdots & 0 & 0 & 0 & 0 & \cdots & 0 & 0 & \cdots & 0 \\ 0 & 0 & \cdots & 0 & \cdots & 0 & 0 & \cdots & 0 & s & 0 & \cdots & 0 & 0 & 0 & \cdots & 0 & 0 & \cdots & 0 \\ \vdots & \vdots & \cdots & \vdots & \cdots & \vdots & \ddots & \ddots & \ddots & \ddots & \ddots & \ddots & \ddots & \ddots & \vdots & \cdots & \vdots & \vdots & \cdots & \vdots \\ 0 & 0 & \cdots & 0 & \cdots & 0 & 0 & \cdots & 0 & 0 & 0 & s & 0 & \cdots & 0 & \cdots & 0 & 0 & \cdots & 0 \end{bmatrix}. \quad (5.8)$$

To further improve the spectral efficiency of the CSTBC-SM scheme, a novel CSTBC-MIMO transmission scheme is developed by adapting circular STBC concept to the MIMO-MBM scheme. In the CSTBC-MIMO transmission scheme, all available T_x transmit antennas are used in transmission through their effective channel states and T_x number of M-PSK/QAM modulated symbols are transmitted. Therefore, the spectral efficiency of the CSTBC-MIMO scheme is given as

$$\eta_{MIMO} = \frac{T_x(M_{rf} + \log_2 M)}{T} \quad \text{[bpcu]}. \quad (5.9)$$

In the CSTBC-MIMO transmission scheme, the first $T_x M_{rf}$ bits of the incoming ηT information bits determine an effective channel state l_i among P channel state realizations for each of T_x transmit antennas, where $l_i \in \{1, 2, \ldots, P\}$. On the other hand, the remaining $T_x \log_2 M$ information bits determine s_i M-PSK/QAM symbols, for $i \in \{1, 2, \ldots, T_x\}$, for the transmission over the selected channel states with the indices l_i. Then, the overall transmission matrix $\mathbf{X} \in \mathbb{C}^{T \times PT_x}$ of the CSTBC-MIMO scheme is given as follows

$$\mathbf{X} = \begin{bmatrix} 0 & \cdots & 0 & s_1 & 0 & \cdots & 0 & 0 & 0 & 0 & \cdots & 0 & s_2 & 0 & \cdots & 0 & 0 & 0 & 0 & \cdots & 0 & \cdots & 0 & s_{T_x} & 0 & \cdots & 0 & 0 & 0 & 0 \\ 0 & 0 & \cdots & 0 & s_1 & 0 & \cdots & 0 & 0 & 0 & 0 & \cdots & 0 & s_2 & 0 & \cdots & 0 & 0 & 0 & \cdots & 0 & 0 & \cdots & 0 & s_{T_x} & 0 & \cdots & 0 & 0 & 0 \\ \vdots & \ddots & \ddots & \ddots & \ddots & \ddots & \ddots & \ddots & \ddots & \vdots & \vdots & \ddots & \ddots & \ddots & \ddots & \ddots & \ddots & \ddots & \ddots & \vdots & \cdots & \vdots & \ddots & \ddots & \ddots & \ddots & \ddots & \ddots & \ddots & \vdots \\ 0 & 0 & \cdots & 0 & 0 & 0 & s_1 & 0 & \cdots & 0 & 0 & 0 & \cdots & 0 & 0 & 0 & s_2 & 0 & \cdots & 0 & \cdots & 0 & 0 & \cdots & 0 & 0 & 0 & s_{T_x} & 0 & \cdots & 0 \end{bmatrix}. \quad (5.10)$$

5.1.3 Transmission model

In the CSTBC-IM transmission schemes, $\mathbf{X} \in \mathbb{C}^{T \times PT_x}$ is transmitted over a channel created by different channel state realizations and represented by $\mathbf{H} \in \mathbb{C}^{PT_x \times R_x}$ while experiencing AWGN samples, denoted by $\mathbf{N} \in \mathbb{C}^{T \times R_x}$. The entries of the matrices $\mathbf{H}$ and $\mathbf{N}$ are modeled by i.i.d. complex Gaussian random variables with distributions of $\mathcal{CN}(0, 1)$ and $\mathcal{CN}(0, \sigma^2)$, respectively. Then, the matrix of received signals $\mathbf{Y} \in \mathbb{C}^{T \times R_x}$ is obtained as

$$\mathbf{Y} = \mathbf{X}\mathbf{H} + \mathbf{W}. \quad (5.11)$$

For a general CSTBC-IM system, the received signals can also be given in the following equivalent model, for $\mathbf{y} = \text{vec}(\mathbf{Y}) \in \mathbb{C}^{TR_x \times 1}$ and $\mathbf{n} = \text{vec}(\mathbf{N}) \in \mathbb{C}^{TR_x \times 1}$,

as

$$\mathbf{y} = \mathbf{H}_e\mathbf{x} + \mathbf{w} \tag{5.12}$$

where $\mathbf{x} = [s_1, s_2, \ldots, s_{T_x}]^{\mathrm{T}} \in \mathbb{C}^{T_x \times 1}$ and s_j is the modulated symbol transmitted over a particular channel state of the jth transmit antenna, for $j = \{1, 2, ..., T_x\}$, while $\mathbf{H}_e \in \mathbb{C}^{TR_x \times T_x}$ is the equivalent channel matrix containing the columns of $\mathbf{H}$ corresponding to the jth transmit antenna.

The receiver of the CSTBC-IM schemes is assumed to have perfect knowledge of the equivalent channel matrix $\mathbf{H}_e$ and consider a maximum likelihood (ML) detector to obtain an optimum BER performance by the following decision rule:

$$\hat{\mathbf{x}} = \arg\min_{\mathbf{s}} ||\mathbf{y} - \mathbf{H}_e\mathbf{x}||^2. \tag{5.13}$$

Then, the detected $\hat{\mathbf{x}}$ is demapped to determine the corresponding bits.

In CSTBC-IM schemes, both correlated and uncorrelated channel fading statistics are considered. For the case of correlated channels, a correlation is assumed among the channel states of each transmit antenna, where the correlation model is taken from a real multi-state reconfigurable antenna with $M_{rf} = 2$ and $P = 2^{M_{rf}} = 4$ channel states [107] and the correlation values among those channel states are represented by the following matrix $\mathbf{R} \in \mathbb{C}^{P \times P}$ [107]

$$\mathbf{R} = \begin{bmatrix} 1 & 0.0722 & 0.0593 & 0.0007 \\ 0.0772 & 1 & 0.0158 & 0.0522 \\ 0.0593 & 0.0158 & 1 & 0.0688 \\ 0.007 & 0.0522 & 0.0688 & 1 \end{bmatrix}. \tag{5.14}$$

For the case of correlated channel states, the correlated $\mathbf{H}$ matrix is constructed by an uncorrelated channel matrix $\tilde{\mathbf{H}} \in \mathbb{C}^{PT_x \times R_x}$ whose entries are i.i.d. complex Gaussian random variables with $\mathcal{CN}(0, 1)$ distribution, as follows:

$$\mathbf{H} = \mathbf{R}_t^{1/2}\tilde{\mathbf{H}}\mathbf{R}_r^{1/2} \tag{5.15}$$

where $\mathbf{R}_t$ and $\mathbf{R}_r$ are the transmit and received correlation matrices. Then, since no spatial correlation is assumed, $\mathbf{R}_t = \mathbf{I}_{T_x} \otimes \mathbf{R}$ and $\mathbf{R}_r = \mathbf{I}_{R_x}$.

5.2 Performance Analysis

In this section, the PEP of the CSTBC-IM transmission schemes is analytically derived and an upper bound expression for the ABEP of the CSTBC-IM schemes is obtained.

To determine the PEP of the proposed systems, first, an expression for conditional PEP is derived [102] for the transmission of $\mathbf{X}$ and its erroneous detection $\hat{\mathbf{X}}$, as follows

$$P_r\big(\mathbf{X}\to\hat{\mathbf{X}}|\mathbf{H}\big)=Q\left(\sqrt{\frac{||(\mathbf{X}-\hat{\mathbf{X}})\mathbf{H}||^2}{4\sigma^2}}\right). \tag{5.16}$$

Let $\Lambda=||\big(\mathbf{X}-\hat{\mathbf{X}}\big)\mathbf{H}||^2$ and $\mathbf{\Delta}$ be the following difference matrix

$$\mathbf{\Delta}=\big(\mathbf{X}-\hat{\mathbf{X}}\big)^{\mathrm{H}}\big(\mathbf{X}-\hat{\mathbf{X}}\big). \tag{5.17}$$

After some algebraic manipulations, $\mathbf{\Delta}$ is given in quadratic form as

$$\begin{aligned}\Lambda&=||\big(\mathbf{X}-\hat{\mathbf{X}}\big)\mathbf{H}||^2\\&=\mathrm{vec}(\tilde{\mathbf{H}}^{\mathrm{H}})^{\mathrm{H}}(\mathbf{R}_s{}^{1/2})^{\mathrm{H}}(\mathbf{I}_{R_x}\otimes\mathbf{\Delta})\mathbf{R}_s{}^{1/2}\mathrm{vec}(\tilde{\mathbf{H}}^{\mathrm{H}})\end{aligned} \tag{5.18}$$

where $\mathbf{R}_s=\mathbf{R}_t\otimes\mathbf{R}_r$. Then, considering the following alternative Q-function expression

$$Q(x)=\frac{1}{\pi}\int_0^{\pi/2}\exp\left(\frac{-x^2}{2\sin^2\theta}\right)d\theta \tag{5.19}$$

and substituting (5.18) into (5.19), (5.16) can be rewritten as

$$P_r\left(\mathbf{X}\to\hat{\mathbf{X}}|\mathbf{H}\right)=\frac{1}{\pi}\int_0^{\pi/2}\exp\left(-\gamma\frac{\mathrm{vec}(\tilde{\mathbf{H}}^{\mathrm{H}})^{\mathrm{H}}\mathbf{\Gamma}\mathrm{vec}(\tilde{\mathbf{H}}^{\mathrm{H}})}{4\sin^2\theta}\right)d\theta \tag{5.20}$$

where $\gamma=1/2\sigma^2$ and $\mathbf{\Gamma}=(\mathbf{R}_s{}^{1/2})^{\mathrm{H}}(\mathbf{I}_{R_x}\otimes\mathbf{\Delta})\mathbf{R}_s{}^{1/2}$. Then, averaging (5.20) over $\mathbf{H}$ and considering a MGF approach [103], the PEP expression is obtained as follows

$$P_r\left(\mathbf{X}\to\hat{\mathbf{X}}\right)=\frac{1}{\pi}\int_0^{\pi/2}\frac{\exp\left(-\bar{\mathbf{z}}^{\mathrm{H}}\frac{\gamma}{4\sin^2\theta}\mathbf{\Gamma}\left(\mathbf{I}_{PT_xR_x}+\frac{\gamma}{4\sin^2\theta}\mathbf{K}_{\mathbf{z}}\mathbf{\Gamma}\right)^{-1}\bar{\mathbf{z}}\right)}{\det\left(\mathbf{I}_{PT_xR_x}+\frac{\gamma}{4\sin^2\theta}\mathbf{K}_{\mathbf{z}}\mathbf{\Gamma}\right)}d\theta \tag{5.21}$$

where $\mathbf{z}=\mathrm{vec}(\tilde{\mathbf{H}}^{\mathrm{H}})$, $\bar{\mathbf{z}}$ is the mean vector and $\mathbf{K}_{\mathbf{z}}=E\left\{\mathbf{z}^{\mathrm{H}}\mathbf{z}\right\}-\bar{\mathbf{z}}^{\mathrm{H}}\bar{\mathbf{z}}$ is the covariance matrix. Then, since $\bar{\mathbf{z}}=0$ and $\mathbf{K}_{\mathbf{z}}=\mathbf{I}_{PT_xR_x}$ for the Rayleigh fading channel matrix $\tilde{\mathbf{H}}$, the PEP of the CSTBC-IM schemes simplifies to

$$P_r\big(\mathbf{X}\to\hat{\mathbf{X}}\big)=\frac{1}{\pi}\int_0^{\pi/2}\det\left[\mathbf{I}_{PT_xR_x}+\gamma\frac{\mathbf{\Gamma}}{4\sin^2\theta}\right]^{-1}d\theta. \tag{5.22}$$

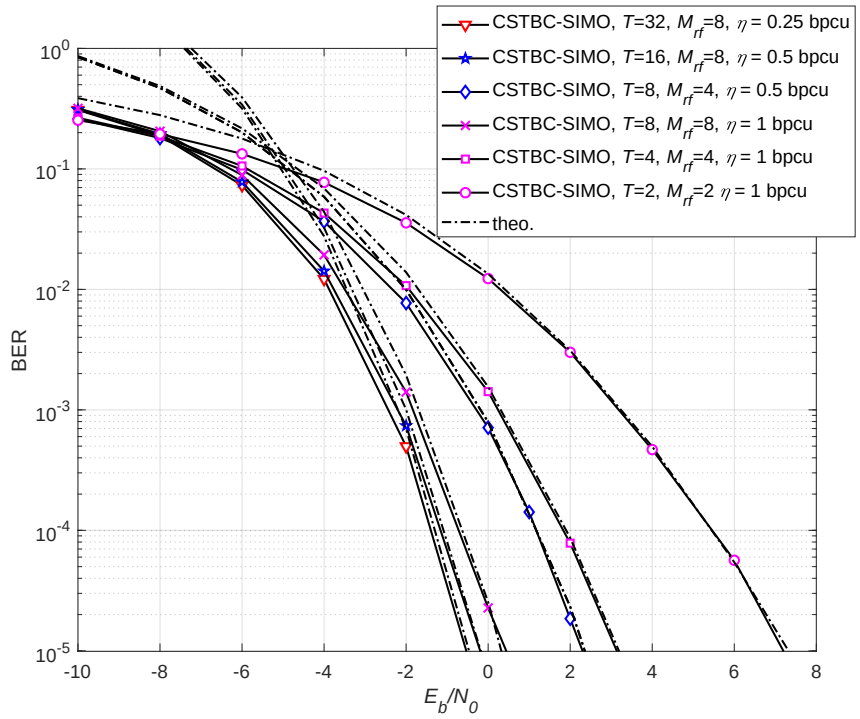

Figure 5.2 : The theoretical and Monte Carlo simulation results of CSTBC-SSK scheme at low spectral efficiency values for $R_x = 4$.

Moreover, to derive a closed form expression, an upper bound is obtained in terms of the non-zero eigenvalues λ_m of the difference matrix $\mathbf{\Delta}$ (5.17) by letting $\theta = \frac{\pi}{2}$, as follows

$$P_r\left(\mathbf{X} \to \hat{\mathbf{X}}\right) \leq \frac{1}{2}\left[\prod_{m=1}^{T}\left(\frac{1}{1+\gamma\frac{\lambda_m}{4}}\right)^{N_r}\right]. \tag{5.23}$$

Then, using the well-known union bound approach [102], ABEP is obtained as:

$$P_b \leq \frac{1}{2^{\eta T}}\sum_{\mathbf{X}}\left[\frac{1}{\eta T}\sum_{\hat{\mathbf{X}}} Pr\left(\mathbf{X} \to \hat{\mathbf{X}}\right) e\left(\mathbf{X}, \hat{\mathbf{X}}\right)\right] \tag{5.24}$$

where $e\left(\mathbf{X}, \hat{\mathbf{X}}\right)$ is the number of bit errors for each $\left(\mathbf{X} \to \hat{\mathbf{X}}\right)$ error event.

5.3 Simulation Results

In this section, the BER performance of CSTBC-IM schemes are investigated via comprehensive theoretical and Monte Carlo simulations to reveal the flexibility of the proposed schemes, which attain both high and low spectral efficiency values while achieving a Tth order transmit diversity gain. All simulations are sketched as a function of received energy per bit to noise ratio (E_b/N_0), where $N_0 = 2\sigma^2$, for $R_x = 4$.

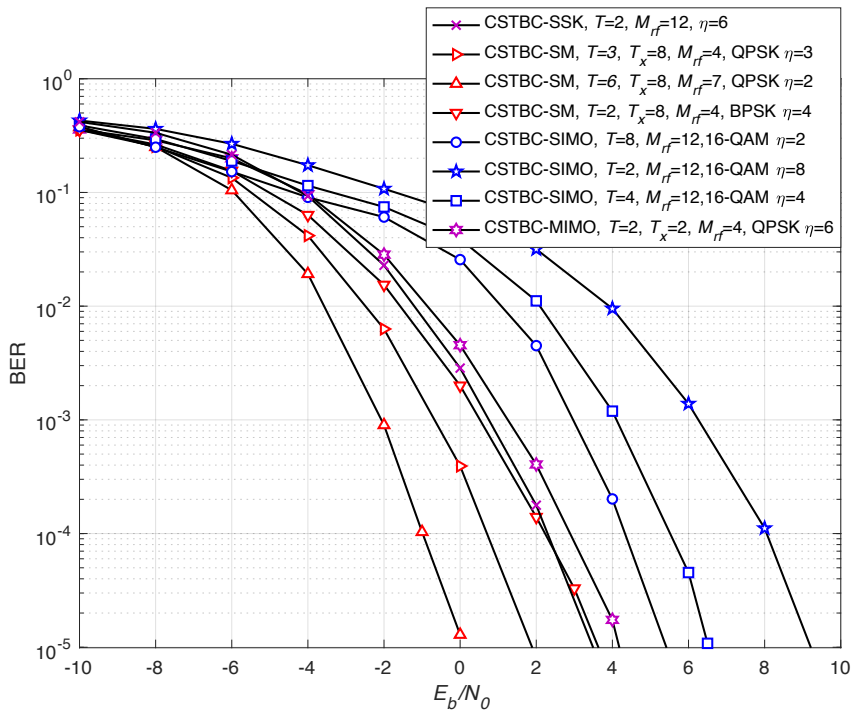

Figure 5.3 : The BER performance of the CSTBC-IM schemes for various spectral efficiency values and $R_x = 4$.

In Figure 5.2, theoretical and computer simulation results of the CSTBC-SSK scheme achieving a Tth order transmit diversity gain are shown for low spectral efficiency values, where T ranges from 2 to 32. These results show that the computer simulation curves are in perfect agreement with the theoretical curves at high E_b/N_0 values. In addition, the effect of increasing transmit diversity on the BER performance is clearly observed, where the BER improves as T increases.

The BER performance of CSTBC-IM schemes that achieve various spectral efficiency values are demonstrated in Figure 5.3. It can be deduced from Figures 5.2 and 5.3 that the proposed CSTBC-IM schemes enable a Tth order transmit diversity gain at both low and high spectral efficiency values.

In Figure 5.4, for $T = 2$, the BER performance of the proposed CSTBC-IM schemes over correlated and uncorrelated channel statistics is investigated. For the correlated channel conditions, the correlation is assumed only among the channel state realizations of each transmit antenna, where the correlation matrix $\mathbf{R}$ given in (5.14) of a real multi-state transmit antenna with $M_{rf} = 2$ and $P = 2^{M_{rf}} = 4$, is considered. For the CSTBC-SIMO and CSTBC-SSK schemes, which respectively attain $\eta = 1$ and 2 bpcu spectral efficiency values, the BER results under the correlated

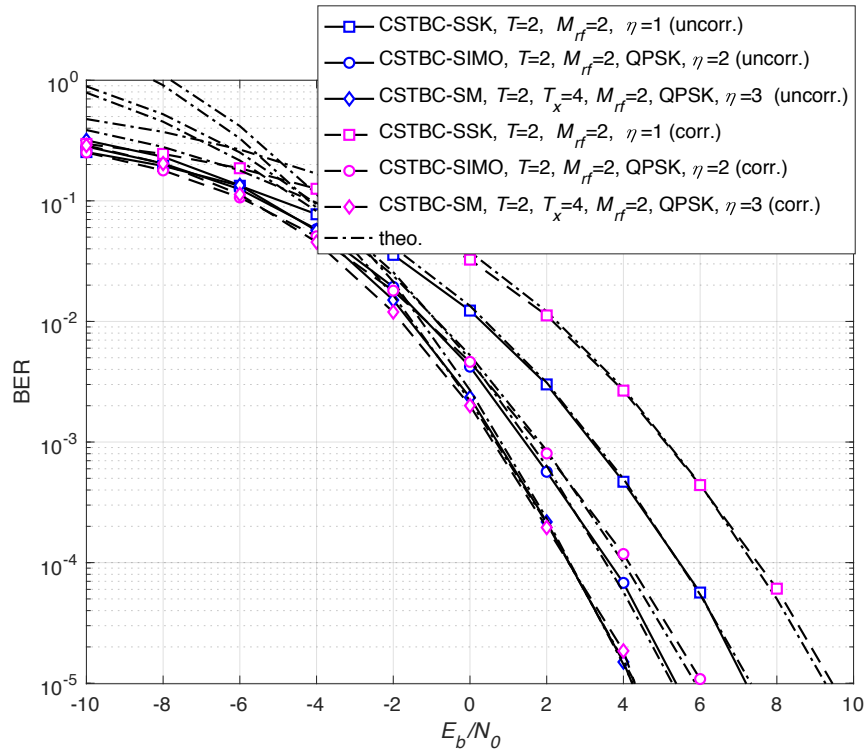

Figure 5.4 : The BER performance of the CSTBC-IM schemes with $M_{rf} = 2$ for correlated and uncorrelated channel statistics and $R_x = 4$.

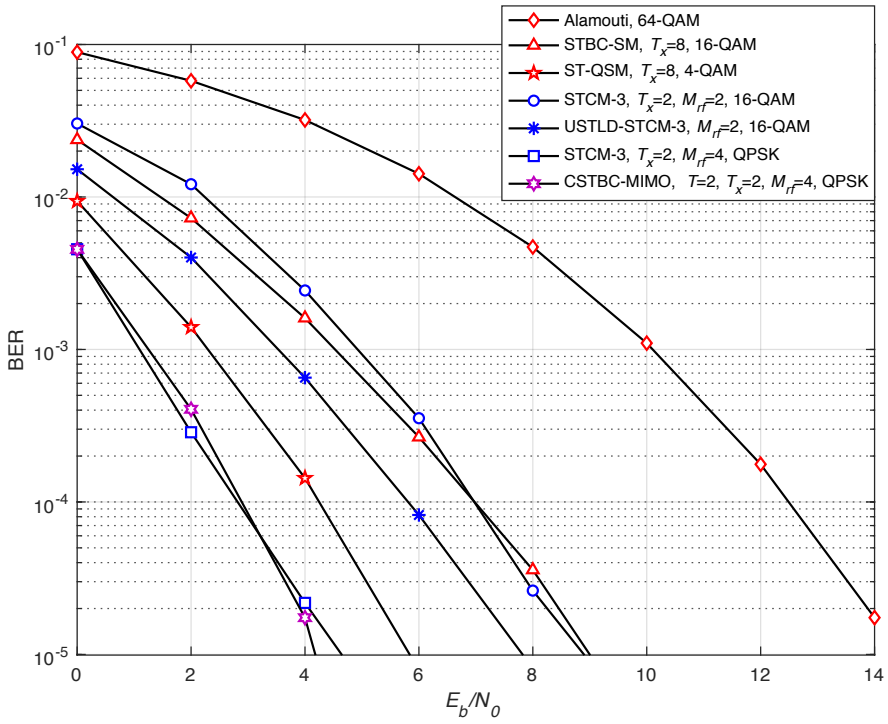

Figure 5.5 : The BER performance of CSTBC-MIMO, STCM, STBC-SM, USTLD-STCM, ST-QSM and Alamouti's STBC schemes for $\eta = 6$ bpcu and $R_x = 4$.

channel conditions are nearly 2 dB behind the uncorrelated case. However, when the same channel state correlation is assumed without any spatial correlation, the BER performance of CTBC-SM, for $T_x = 4$, $M_{rf} = 2$ and QPSK, is almost the same as the uncorrelated case.

In Figure 5.5, the BER performance of CSTBC-MIMO scheme is compared to that of the state-of-the-art transmission schemes achieving a second-order transmit diversity gain at $\eta = 6$ bpcu. The results show that the BER performance of the CSTBC-MIMO scheme for $T_x = 2$, $M_{rf} = 4$ and QPSK is far beyond the traditional STBC-based IM schemes [32, 33, 105, 106] while it achieves a nearly 0.5 dB E_b/N_0 gain over the recent STCM scheme [28].

5.4 Summary

In this chapter, the family CSTBC-IM schemes, which achieve various orders of transmit diversity gains with a single RF chain, have been proposed for beyond 5G ultra-reliable communication applications. The error performance of CSTBC-IM schemes has been theoretically analyzed and an upper-bound expression for ABEP has been derived. Through extensive Monte Carlo simulations, the flexibility of the proposed systems to attain higher spectral efficiency values while providing various transmit diversity gains have been shown, which can make the CSTBC-IM schemes as a potential enabler for beyond 5G ultra-reliable communication applications.

6. LOW COMPLEXITY ADAPTATION FOR RIS-BASED MIMO SYSTEMS

In this chapter, an efficient low-complexity algorithm, which is based on cosine similarity theorem [108] and adapts the phase shift of each reflecting elements, is proposed for RIS-aided MIMO (RIS-MIMO) and RIS-aided SM (RIS-SM) schemes in which the transmission principles of classical MIMO and classical SM [3, 72] are considered, respectively. Moreover, a semi-analytical probabilistic model is developed to derive the ABEP of the proposed RIS-MIMO and RIS-SM schemes. Furthermore, through the comprehensive computer simulations, the BER performance of the RIS-aided MIMO systems with the proposed algorithm is investigated for the various conditions including perfect/imperfect channel estimation, continous/discrete phase reflection and path loss effect.

The rest of this chapter is structured as follows. In Section 6.1, the system model of the proposed RIS-aided MIMO transmission systems is presented. The theoretical performance analysis of the system is carried out in Section 6.2. Computer simulation results are described in Section 6.3 and the chapter is concluded in Section 6.4.

6.1 System Model

In this section, the concept of the proposed low-complexity algorithm and the system models of the RIS-MIMO and RIS-SM schemes are introduced. In the proposed systems, the transmitter and the receiver are assumed to be equipped with T_x and R_x antennas, respectively, as shown in Figure 6.1. In addition, an RIS with N passive reflecting elements is used to improve the communication performance by appropriately adjusting phase shift of each reflecting element. Consider $\mathbf{H} \in \mathbb{C}^{N \times T_x}$ and $\mathbf{G} \in \mathbb{C}^{N \times R_x}$ as the matrices of uncorrelated Rayleigh fading channel from the transmitter to the RIS, and from the RIS to the receiver, respectively, whose elements are i.i.d. and follow $\mathcal{CN}(0,1)$ distribution. On the other hand, $\mathbf{\Phi} \in \mathbb{C}^{N \times N}$ stands for the matrix of RIS reflection coefficients with $\mathbf{\Phi} = \operatorname{diag}\left\{\xi_1 e^{j\phi_1}, \xi_2 e^{j\phi_2}, \ldots, \xi_N e^{j\phi_N}\right\}$, where $\phi_i \in [-\pi, \pi]$ is phase shift and $\xi_i \in (0, 1]$ is the amplitude reflection coefficient

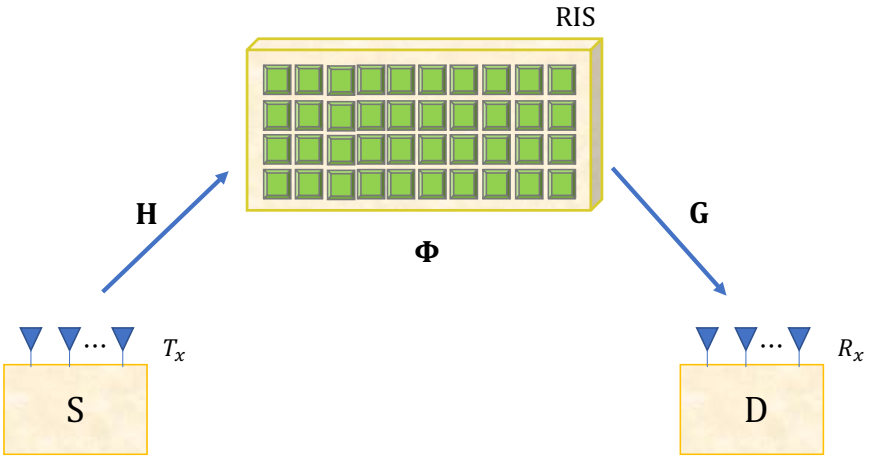

Figure 6.1 : RIS-aided MIMO system.

of the ith reflecting element, for $i \in \{1, 2, \ldots, N\}$. However, for the sake of simplicity, we set $\xi_i = 1$. Therefore, the composite MIMO channel matrix $\mathbf{C} \in \mathbb{C}^{R_x \times T_x}$ from the transmitter to the receiver becomes $\mathbf{C} = \mathbf{G}^{\mathrm{H}} \mathbf{\Phi} \mathbf{H}$. In the proposed systems, perfect channel state information (CSI) of all channels are available at all nodes and quasi-static block fading channels are assumed.

6.1.1 Proposed algorithm

In this subsection, we develop a low-complexity algorithm to maximize the average received SNR of the RIS aided MIMO systems, which results in maximizing the overall channel gain of the system by arranging the phase shift of each reflecting element. Then, using $\mathbf{C} = \mathbf{G}^{\mathrm{H}} \mathbf{\Phi} \mathbf{H} = \sum_{i=1}^{N} \mathbf{g}_i^H e^{j\phi_i} \mathbf{h}_i$, our problem is formulated as

$$\begin{aligned} &\max_{\phi_i} \|\mathbf{C}\| = \max_{\phi_i} \| \sum\nolimits_{i=1}^{N} \mathbf{g}_i^H e^{j\phi_i} \mathbf{h}_i \| \\ &\text{s.t.} \quad |e^{j\phi_i}| = 1 \end{aligned} \tag{6.1}$$

where $\mathbf{g}_i^{\mathrm{H}}$ and $\mathbf{h}_i$ stand for the ith column and ith row of $\mathbf{G}^{\mathrm{H}}$ and $\mathbf{H}$, respectively. Although the maximization problem in (6.1) is non-convex due to the constraint $\phi_i \in [-\pi, \pi]$, the achievable channel gain can be upper bounded as

$$\|\mathbf{C}\| = \| \sum\nolimits_{i=1}^{N} \mathbf{g}_i^H e^{j\phi_i} \mathbf{h}_i \| \leq \sum\nolimits_{i=1}^{N} \|\mathbf{g}_i^{\mathrm{H}}\| \, \|\mathbf{h}_i\| \, . \tag{6.2}$$

Then, exploiting (6.2), the maximum achievable gain of the component at the kth row and the lth column of $\mathbf{C}$, shown by $c_{k,l}$, can be given as

$$|c_{k,l}| = | \sum\nolimits_{i=1}^{N} g_{k,i} e^{j\phi_i} h_{i,l} | \leq \sum\nolimits_{i=1}^{N} |g_{k,i}| |h_{i,l}| \tag{6.3}$$

Algorithm 1 Cosine Similarity-based Low-Complexity Algorithm

Input: $\mathbf{h}_i$, $\mathbf{g}_i$, $\tilde{\mathbf{h}}_i$, $\tilde{\mathbf{g}}_i$
Output: $\mathbf{\Phi}$

1: **for** $i = 1 : N$ **do**
2: $\quad \phi_i^h = \arccos\left(\frac{<\mathbf{h}_i, \tilde{\mathbf{h}}_i>_{\mathrm{Re}}}{||\mathbf{h}_i||||\tilde{\mathbf{h}}_i||}\right)$
3: $\quad \phi_i^g = \arccos\left(\frac{<\mathbf{g}_i^{\mathrm{H}}, \tilde{\mathbf{g}}_i^{\mathrm{H}}>_{\mathrm{Re}}}{||\mathbf{g}_i^{\mathrm{H}}||||\tilde{\mathbf{g}}_i^{\mathrm{H}}||}\right)$
4: $\quad \phi_i = -(\phi_i^h + \phi_i^g)$
5: **end for**
6: $\mathbf{\Phi} = \mathrm{diag}(e^{j\phi_1}, e^{j\phi_2}, \ldots, e^{j\phi_N})$

where $g_{k,i}$ and $h_{i,l}$ are the kth and lth components of the channel vectors $\mathbf{g}_i^{\mathrm{H}}$ and $\mathbf{h}_i$, respectively, for $k \in \{1, 2, \ldots, R_x\}$ and $l \in \{1, 2, \ldots, T_x\}$. It is quite obvious that there exists an optimum $\mathbf{\Phi}$ matrix that satisfies (6.3) with an equality to achieve the maximum channel gain. However, due to the non-convex constraints, it is difficult to find an optimal solution for this problem in a computationally efficient and robust manner. Moreover, this challenge increases when a multi-antenna system is considered at both the transmitter and the receiver. Due to these limitations, we develop an efficient suboptimal solution using the cosine similarity theorem [108], where the angle between $\mathbf{u}$ and $\mathbf{v}$ vectors is calculated, using their inner product and magnitudes [108], as

$$\cos(\mathbf{u}, \mathbf{v}) = \frac{<\mathbf{u}, \mathbf{v}>}{||\mathbf{u}||||\mathbf{v}||}. \tag{6.4}$$

In the proposed algorithm, to maximize the individual gain of each $c_{k,l}$ component (6.3) the phase shift ϕ_i is adjusted to approximate the complex channel vectors $\mathbf{h}_i$ and $\mathbf{g}_i^{\mathrm{H}}$ to their component-wise absolute vectors $\tilde{\mathbf{h}}_i = [|h_{i,1}|, |h_{i,2}|, , \ldots |h_{i,T_x}|]$ and $\tilde{\mathbf{g}}_i^{\mathrm{H}} = [|g_{1,i}|, |g_{2,i}|, , \ldots |g_{R_x,i}|]^{\mathrm{H}}$, respectively. Therefore, in Algorithm 1, real ϕ_i^h and ϕ_i^g angles are calculated in order to measure the cosine similarity between the vectors $\mathbf{h}_i$ and $\tilde{\mathbf{h}}_i$ and $\mathbf{g}_i^{\mathrm{H}}$ and $\tilde{\mathbf{g}}_i^{\mathrm{H}}$, respectively. Then, for the ith reflecting element, the overall phase shift ϕ_i is determined as $\phi_i = -(\phi_i^h + \phi_i^g)$ and the overall reflection matrix $\mathbf{\Phi}$ is obtained accordingly.

Let us present the concept of the proposed algorithm by an example. Consider an RIS-aided MIMO system, with $T_x = 2$, $R_x = 3$ ve $N = 2$ whose composite channel matrix $\mathbf{C} = \mathbf{G}^{\mathrm{H}}\mathbf{\Phi}\mathbf{H}$ is constructed as

$$\mathbf{C} = \begin{bmatrix} g_{11} & g_{12} \\ g_{21} & g_{22} \\ g_{31} & g_{32} \end{bmatrix} \begin{bmatrix} e^{j\phi_1} & 0 \\ 0 & e^{j\phi_2} \end{bmatrix} \begin{bmatrix} h_{11} & h_{12} \\ h_{21} & h_{22} \end{bmatrix} \tag{6.5}$$

which can be rewritten, in the form of $\mathbf{C} = \sum_{i=1}^{N} \mathbf{g}_i^H e^{j\phi_i} \mathbf{h}_i$, as

$$\mathbf{C} = \begin{bmatrix} g_{11} \\ g_{21} \\ g_{31} \end{bmatrix} e^{j\phi_1} \begin{bmatrix} h_{11} & h_{12} \end{bmatrix} + \begin{bmatrix} g_{12} \\ g_{22} \\ g_{32} \end{bmatrix} e^{j\phi_2} \begin{bmatrix} h_{21} & h_{22} \end{bmatrix}. \tag{6.6}$$

Since the phase shift ϕ_i only affects $\mathbf{g}_i^{\mathrm{H}}$ and $\mathbf{h}_i$ vectors, instead of jointly adjusting all phases, each ϕ_i can be individually determined in a more computationally efficient manner. Therefore, in the proposed algorithm, considering (6.3), we singly determine each ϕ_i to improve the overall channel gain. For this aim, ϕ_i is properly adjusted to make the channel vectors $\mathbf{h}_i$ and $\mathbf{g}_i^{\mathrm{H}}$ approximate to their component-wise absolute vectors $\tilde{\mathbf{h}}_i = [|h_{i,1}|, |h_{i,2}|]$, and $\tilde{\mathbf{g}}_i^{\mathrm{H}} = [|g_{1,i}|, |g_{2,i}|, |g_{3,i}|]^{\mathrm{H}}$, respectively. Therefore, as given in Algorithm 1, the real angles ϕ_i^h and ϕ_i^g, which respectively measure the similarities between the vectors $\mathbf{h}_i$ and $\tilde{\mathbf{h}}_i$, and the vectors $\mathbf{g}_i^{\mathrm{H}}$ and $\tilde{\mathbf{g}}_i^{\mathrm{H}}$, are calculated using the cosine similarity theorem [108]. Then, the effective phase shift of ith reflecting elements is set to $\phi_i = -(\phi_i^h + \phi_i^g)$. After N repetitions are performed, the overall reflection matrix $\mathbf{\Phi}$ is constructed.

The required complexity to perform this algorithm is $\mathcal{O}(6N(T_x + R_x))$ in terms of real multiplications. It is worth noting that when a SISO system ($T_x = R_x = 1$) is considered, this algorithm satisfies (6.3) with equality that achieves the optimum channel gain in [95].

6.1.2 RIS-MIMO scheme

In the proposed RIS-MIMO scheme with T_x transmit antennas, R_x receive antennas and N reflecting elements, a classical MIMO transmission principle is applied and the reflection parameters are determined by performing the proposed low-complexity algorithm to improve the overall channel gain. Let $\mathbf{x} = [x_1, x_2, \ldots, x_{T_x}]^{\mathrm{T}} \in \mathbb{C}^{T_x \times 1}$ be the transmitted signal vector of the RIS-MIMO scheme, where x_j denotes an M-ary PSK/QAM symbol transmitted through jth transmit antenna, for $j \in \{1, 2, \ldots, T_x\}$. Then, the received signal vector $\mathbf{y} \in \mathbb{C}^{R_x \times 1}$ becomes

$$\begin{aligned} \mathbf{y} &= \mathbf{G}^{\mathrm{H}} \mathbf{\Phi} \mathbf{H} \mathbf{x} + \mathbf{n} \\ &= \mathbf{C}\mathbf{x} + \mathbf{n} \end{aligned} \tag{6.7}$$

where $\mathbf{n} \in \mathbb{C}^{R_x \times 1}$ is the vector of additive white Gaussian noise samples whose elements are i.i.d. and follow $\mathcal{CN}(0, N_0)$ distribution.

6.1.3 RIS-SM scheme

In this subsection, the system model of the RIS-SM scheme, where an RIS-aided MIMO scheme applying the traditional SM transmission principle [3] is presented. Unlike traditional SM [3], in the proposed RIS-SM scheme, the transmitted signal quality is significantly improved by the RIS, whose each reflection parameter is arranged using the proposed low-complexity algorithm.

In RIS-SM, one of the T_x transmit antenna is activated and a modulated symbol s from the M-PSK constellation is transmitted through this active antenna. Since the remaining transmit antennas are deactivated, the signal vector is determined as $\mathbf{x} = \begin{bmatrix} 0 & \dots 0 & s & 0 & \dots & 0 \end{bmatrix}^{\mathrm{T}}$ and transmitted through the overall channel matrix $\mathbf{C}$ as given in (6.7).

Note that in the proposed RIS-SM scheme, the knowledge of the active antenna index is not provided to the RIS.

At the receiver of both RIS-MIMO and RIS-SM schemes, to obtain the best BER performance, a ML detector is considered, and the transmit RIS-SM and RIS-MIMO vectors are detected by considering all possible $\mathbf{x}$ realizations as follows

$$\hat{\mathbf{x}} = \arg\min_{\mathbf{x}} \|\mathbf{y} - \mathbf{C}\mathbf{x}\|^2 . \tag{6.8}$$

6.2 Performance Analysis

In this section, the theoretical BER performance of the proposed RIS-MIMO and RIS-SM schemes is evaluated by performing a semi-analytical probabilistic approach.

6.2.1 Numerical analysis

As given in Algorithm 1, since the proposed algorithm relates the phase shifts of the reflecting elements with the channel statistics, the reflection matrix $\mathbf{\Phi}$ is directly correlated with the channel matrices $\mathbf{H}$ and $\mathbf{G}$. Therefore, the distribution of the composite channel matrix $\mathbf{C}$ could not be derived through a fully analytic approach. As a result, we resort to a comprehensive numerical analysis in order to obtain the statistics of the channel matrix $\mathbf{C}$.

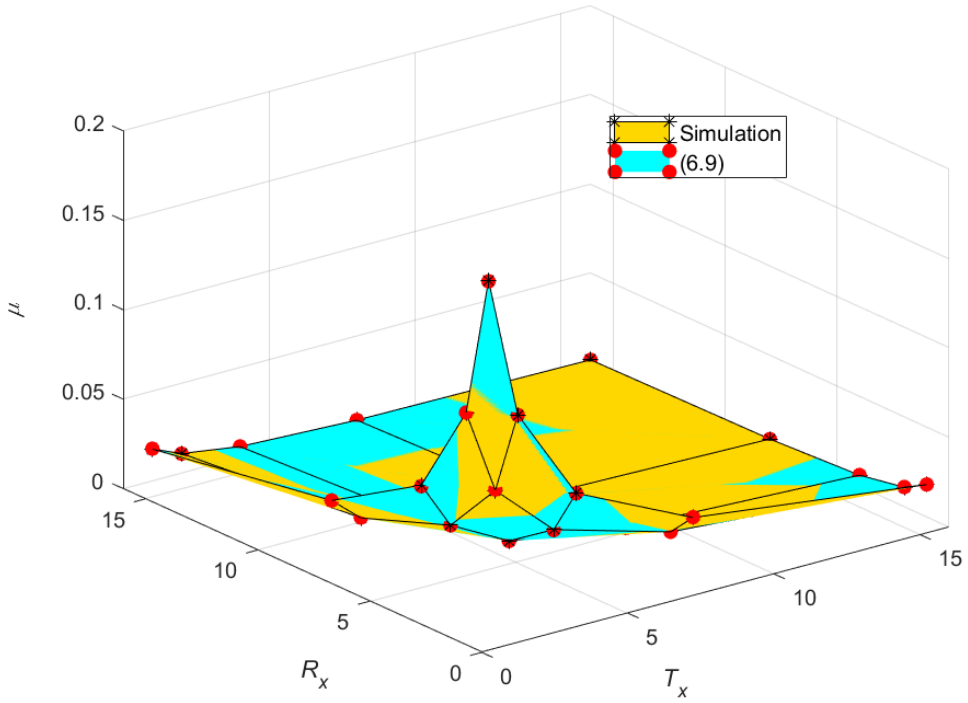

Figure 6.2 : Comparison of the mean μ (6.9) with the Monte-Carlo simulations for different T_x ve R_x antennas.

As it is stated in the previous section, the elements of the channel matrices $\mathbf{H}$ and $\mathbf{G}$ are i.i.d. and follow $\mathcal{CN}(0,1)$ distribution. Our comprehensive numerical analysis, which performs 10^6 Monte-Carlo trials for each $R_x \times T_x$ configuration, indicates that the elements of the composite $\mathbf{C}$ matrix are complex Gaussian random variables with $\mathcal{CN}(N\mu, N)$ distribution, where μ is numerically calculated, in terms of T_x and R_x, as

$$\mu = \frac{1.8}{(1+2T_x)(1+2R_x)}. \tag{6.9}$$

For supporting the accuracy of this estimation, in Figure 6.2, (6.9) is compared to the the channel statistics of $\mathbf{C}$ for $N = 1$, which is obtained through the Monte Carlo simulations performing at least 10^6 trials for each $R_x \times T_x$ set-up. The results show that the estimated μ in (6.9) perfectly fit the computer simulations per $R_x \times T_x$.

Then, (6.9) is utilized to determine the ABEP of the system in the following subsection.

6.2.2 ABEP analysis

In this subsection, after obtaining a numerical approximation for the statistics of the channel matrix $\mathbf{C}$, an upper bound expression for the ABEP of the proposed system is

given as follows [102]:

$$P_e \leq \frac{1}{\eta 2^{\eta}} \sum_{\mathbf{x}} \sum_{\hat{\mathbf{x}}} P_r(\mathbf{x} \to \hat{\mathbf{x}}) e(\mathbf{x}, \hat{\mathbf{x}}) \tag{6.10}$$

where η is the number of incoming information bits, $P_r(\mathbf{x} \to \hat{\mathbf{x}})$ is the unconditional PEP and $e(\mathbf{x}, \hat{\mathbf{x}})$ is the number of error bits for the corresponding PEP event.

To obtain the PEP expression, first, the CPEP of the system is derived, using the Q-function, as follows

$$P_r(\mathbf{x} \to \hat{\mathbf{x}}|\mathbf{C}) = Q\Big(\sqrt{\frac{\Lambda}{2\sigma^2}}\Big) \tag{6.11}$$

where Ω is given, for $\mathbf{\Delta} = (\mathbf{x} - \hat{\mathbf{x}})(\mathbf{x} - \hat{\mathbf{x}})^H$, as

$$\Lambda = ||\mathbf{C}\big(\mathbf{x} - \hat{\mathbf{x}}\big)||^2 \tag{6.12}$$

$$= \mathrm{vec}(\mathbf{C}^{\mathrm{H}})^{\mathrm{H}} (\mathbf{\Delta} \otimes \mathbf{I}_{R_x}) \mathrm{vec}(\mathbf{C}^{\mathrm{H}}). \tag{6.13}$$

Therefore, considering $Q(x) = \frac{1}{\pi} \int_0^{\pi/2} e^{-x^2/2\sin^2\theta} d\theta$, the CPEP (6.11) can be rewritten as

$$P_r\left(\mathbf{x} \to \hat{\mathbf{x}}|\mathbf{C}\right) = \frac{1}{\pi} \int_0^{\pi/2} \exp\Big(-\gamma \frac{\mathrm{vec}(\mathbf{C}^{\mathrm{H}})^{\mathrm{H}} (\mathbf{\Delta} \otimes \mathbf{I}_{R_x}) \mathrm{vec}(\mathbf{C}^{\mathrm{H}})}{4\sin^2\theta}\Big) d\theta \tag{6.14}$$

where $\gamma = 1/N_0$. Then, averaging (6.14) over the matrix $\mathbf{C}$ through MGF approach results in the following PEP expression

$$P_r\left(\mathbf{x} \to \hat{\mathbf{x}}\right) = \frac{1}{\pi} \int_0^{\pi/2} \mathcal{M}_{\Lambda}\left(\frac{-\gamma}{4\sin^2\theta}\right) d\theta. \tag{6.15}$$

In [103], the MGF of $\mathbf{z}^{\mathrm{H}}\mathbf{Q}\mathbf{z}$, for any Hermitian $\mathbf{Q}$ matrix, is given by

$$\mathcal{M}(s) = \exp\left(\frac{s\bar{\mathbf{z}}^{\mathrm{H}}\mathbf{Q}(\mathbf{I} - s\mathbf{K}_{\mathbf{z}}\mathbf{Q})^{-1}\bar{\mathbf{z}}}{\det(\mathbf{I} - s\mathbf{K}_{\mathbf{z}}\mathbf{Q})}\right) \tag{6.16}$$

where $\bar{\mathbf{z}}$ is the mean vector and $\mathbf{K}_{\mathbf{z}}$ is the covariance matrix of the vector $\mathbf{z}$.

Clearly, in our system $\mathbf{Q} = \mathbf{\Delta} \otimes \mathbf{I}_{R_x}$ and $\mathbf{z} = \mathrm{vec}(\mathbf{C}^{\mathrm{H}})$. Using the numerically obtained channel statistics given in the previous subsection, $\bar{\mathbf{z}} = \overline{\mathrm{vec}(\mathbf{C}^{\mathrm{H}})} = \mu N \mathbf{1}$ and $\mathbf{K}_{\mathbf{z}} = N\mathbf{I}$ are respectively defined as the mean vector and the covariance matrix for the Gaussian vector $\mathbf{z} = \mathrm{vec}(\mathbf{C}^{\mathrm{H}})$. Therefore, the PEP of the system becomes

$$P_r\left(\mathbf{x} \to \hat{\mathbf{x}}\right) = \frac{1}{\pi} \int_0^{\pi/2} \frac{\exp\left(-\bar{\mathbf{z}}^{\mathrm{H}} \frac{\gamma}{4\sin^2\theta} \mathbf{Q} \left(\mathbf{I} + \frac{\gamma}{4\sin^2\theta} \mathbf{K}_{\mathbf{z}} \mathbf{Q}\right)^{-1} \bar{\mathbf{z}}\right)}{\det\left(\mathbf{I} + \frac{\gamma}{4\sin^2\theta} \mathbf{K}_{\mathbf{z}} \mathbf{Q}\right)} d\theta. \tag{6.17}$$

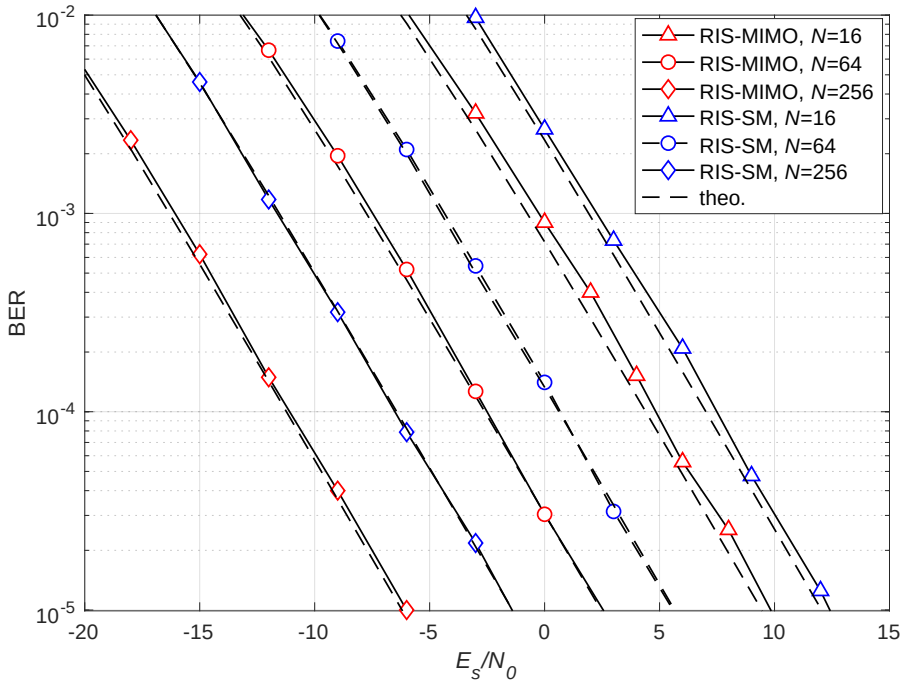

Figure 6.3 : Theoretical and simulation results of the RIS-MIMO ve RIS-SM schemes.

6.3 Simulation Results

In this section, the BER performance of the proposed RIS-MIMO and RIS-SM schemes are investigated through theoretical analysis and comprehensive computer simulations. All results are performed as a function of transmitted signal energy to noise ratio (E_s/N_0) and for different $R_x \times T_x$ MIMO configurations and BPSK modulation ($M = 2$).

In Figure 6.3, for 4×2 MIMO and various N reflecting elements, the theoretical BER performance of RIS-MIMO and RIS-SM schemes are compared with the computer simulation results. It is obvious from this figure that the derived semi-analytic results perfectly match with the simulation results as N increases.

In Figure 6.4, for 4×4 system configuration, the BER performance of the RIS-MIMO and RIS-SM schemes using the proposed cosine similarity theorem-based algorithm and pseudoinverse (pinv)-based algorithm [109] is compared. The results show that compared to [109], the BER performance of both RIS-MIMO and RIS-SM schemes using the proposed algorithm, which requires significantly lower computational complexity, improves better as N increases.

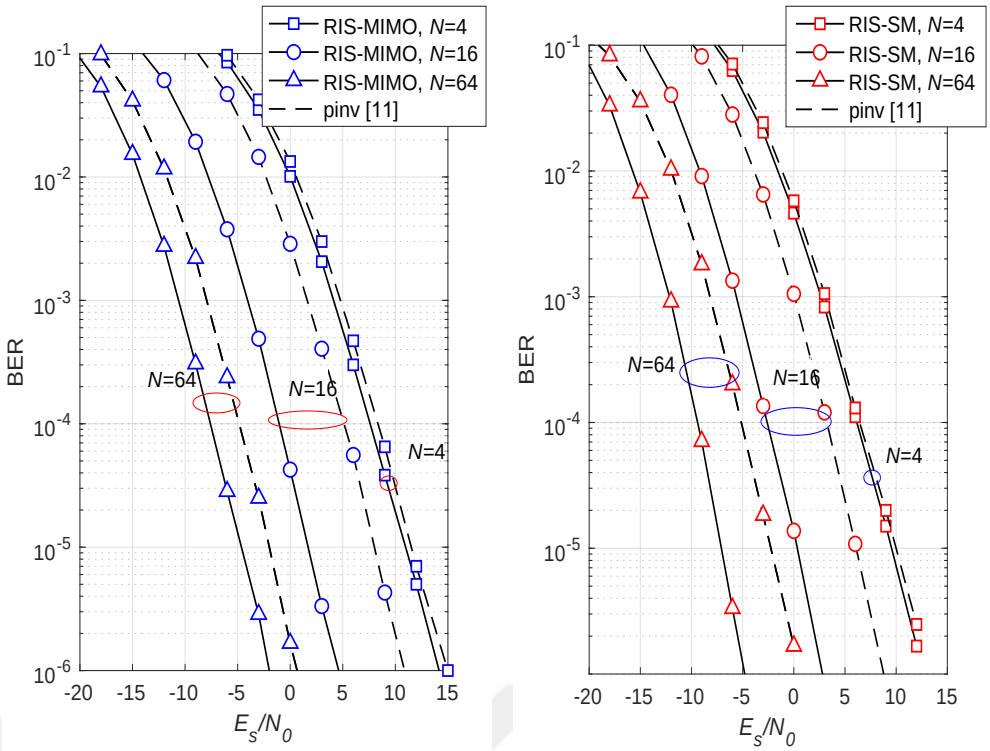

Figure 6.4 : Comparison of the proposed algorithm to the pinv algorithm on the BER performance of the a) RIS-MIMO and b) RIS-SM schemes.

As an illustration, the proposed algorithm with $\mathcal{O}(6N(T_x+R_x))$ complexity performs 3072 real multiplications for $N=64$, while the reference pinv algorithm [109] with $\mathcal{O}(N^3)$ complexity performs 262144 real multiplications. This means, the proposed algorithm provides 98.8% reduction in computational complexity over the reference algorithm [109] for $N=64$.

In Figure 6.5, the impact of the imperfect channel knowledge and the use of discrete phase shifts on the BER performance of the 4×4 RIS-MIMO scheme is investigated for N reflecting elements.

For the discrete phase shifts model, we assume that each reflecting element at the RIS takes a finite number of discrete phase values. Therefore, a set of discrete phase shifts is constructed by uniformly quantizing $[0,\pi]$[1] interval into N levels as $\mathcal{F}=\{0,\,\Delta\phi,\,\ldots,\,(N-1)\Delta\phi\}$, where $\Delta\phi=\pi/N$. Then, the continuous phase shift of each reflecting element, which is obtained via the proposed algorithm, is rounded to the nearest discrete level. The simulation results demonstrate that discrete phase reflection causes a minor BER performance degradation compared to the continuous

[1]In Algorithm I, for $\arccos(\cdot)$ operation, MATLAB function *acos*() is used, which returns phase values between the interval $[0,\pi]$.

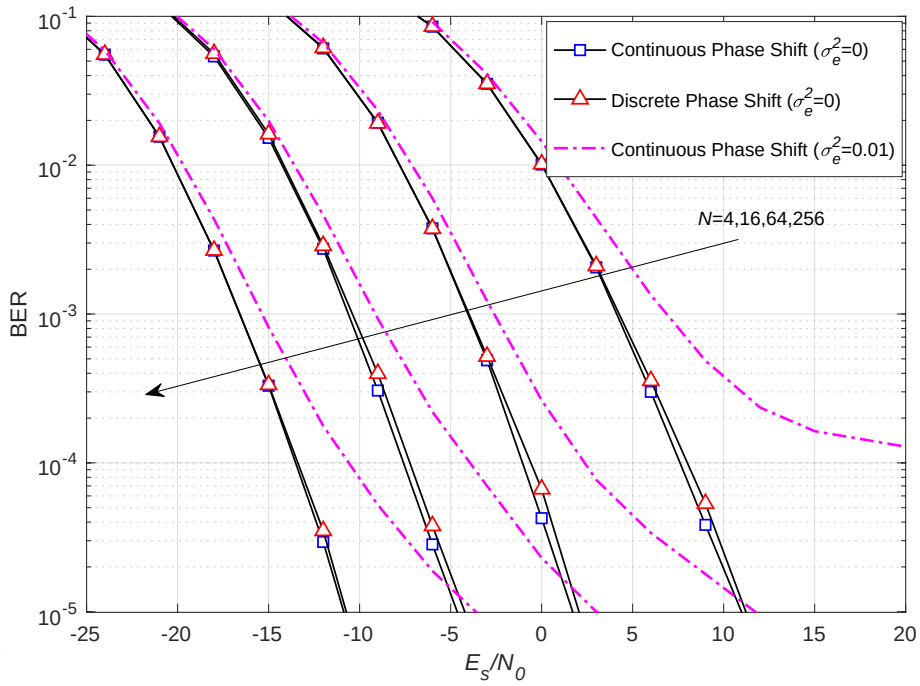

Figure 6.5 : BER Performance of RIS-MIMO scheme with discrete and continuous phase reflection for the channel estimation error variance σ_e^2.

phase reflection. However, this performance difference gradually disappears as N increases.

Moreover, to analyze the effect of the channel estimation error, the imperfect CSI is assumed at both the RIS and the receiver. Therefore, we consider that both the RIS and the receiver erroneously estimate $\mathbf{H}$ and $\mathbf{G}$ channel matrices as $\bar{\mathbf{H}} \in \mathbb{C}^{N \times T_x} = \mathbf{H} + \mathbf{E_t}$ and $\bar{\mathbf{G}} \in \mathbb{C}^{N \times R_x} = \mathbf{G} + \mathbf{E_r}$, respectively, where $\mathbf{E_t}$ and $\mathbf{E_r}$ are the matrices of the channel estimation errors whose each entry is i.i.d. and distributed as $\mathcal{CN}(0, \sigma_e^2)$. Therefore, after the proposed algorithm determines the diagonal reflection matrix $\bar{\mathbf{\Phi}} \in \mathbb{C}^{N \times N}$ considering the imperfect channels $\bar{\mathbf{H}}$ and $\bar{\mathbf{G}}$, the overall estimated channel matrix becomes $\bar{\mathbf{C}} \in \mathbb{C}^{R_x \times T_x} = \bar{\mathbf{G}}^{\mathrm{H}} \bar{\mathbf{\Phi}} \bar{\mathbf{H}}$. The simulation results reveal that the assumption of the imperfect CSI at both the RIS and the receiver significantly degrades the BER performance of the RIS-MIMO scheme. However, increasing the number of reflecting elements at the RIS reduces this performance degradation.

Figure 6.6 demonstrates the BER performance of the proposed RIS-MIMO scheme with 4×4 when path loss effect [64] is considered. Denoting the distances from the transmitter to the RIS and from the RIS to the receiver as d_1 and d_2, respectively, the path loss P_L of the overall system is calculated as [64]

$$P_L^{-1} = \frac{\lambda^4}{256\pi^2} \frac{1}{d_1^2 d_2^2} \tag{6.18}$$

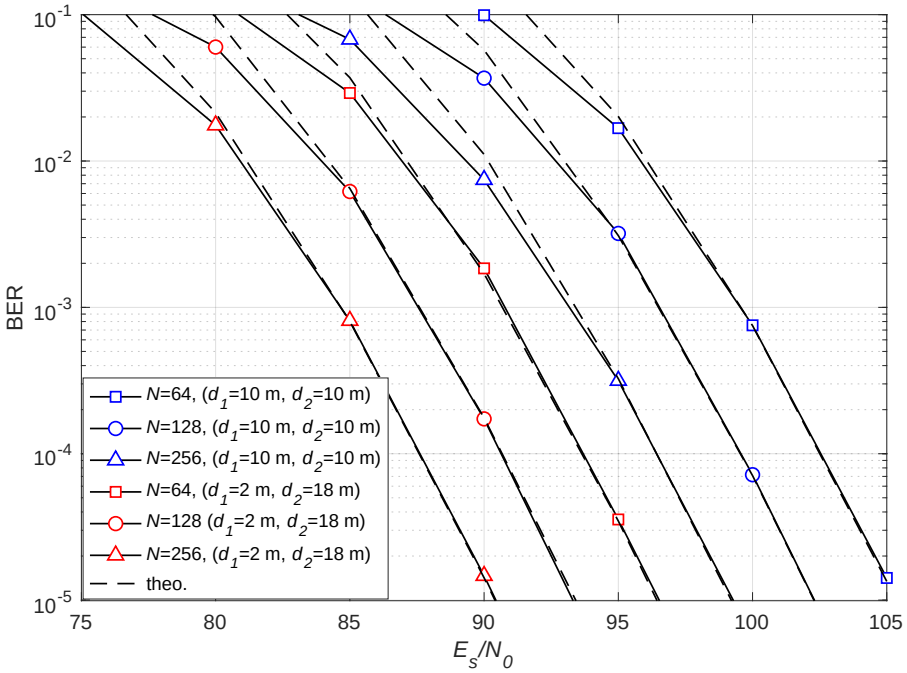

Figure 6.6 : BER Performance of RIS-MIMO scheme in case of the path loss effect.

where λ is the wavelength at 2.4 GHz operating frequency. The simulations are performed for $d_1 = d_2 = 10$ m and $d_1 = 2$ m, $d_2 = 18$ m. It can be deduced from the results that compared to the performance in the absence of the path loss given in Figure 6.4, the error performance of the RIS-MIMO scheme significantly degrade with the path loss effect. On the other hand, since the P_L is proportional to $d_1^2 d_2^2$, the BER performance of the system fairly improves when the RIS is closer to the transmitter or the receiver ($d_1 = 2$ m and $d_2 = 18$ m).

6.4 Summary

In this chapter, a low-complexity algorithm has been developed exploiting the cosine similarity theorem for RIS aided MIMO transmission schemes to enhance the overall path gain of the communication channel. Moreover, performing a semi-analytic approach, the ABEP of the system has been derived. Furthermore, through the comprehensive computer simulations the BER performance of RIS aided MIMO schemes for different circumstances including discrete phase reflection, path loss effect and imperfect CSI has been investigated.

7. HYBRID REFLECTION MODULATION

This chapter presents a novel IM scheme called *hybrid reflection modulation* (HRM) that utilizes a hybrid RIS which consists of both active and passive elements to support the transmission of a SISO system. In other words, the main motivation of this study is to combine the attractive advantages of IM and active RIS systems in a clever scheme in which the RIS operates as a part of the transmitter and directly transmits information. This makes the proposed scheme fundamentally different from the recent hybrid RIS-aided designs that consider the classical SISO signaling over a hybrid RIS architecture employing a certain number of active reflecting elements [86, 110]. In the proposed HRM scheme, we assume that the RIS elements are equipped with electronically controllable phase shifters and reflection-type amplifiers [83], which enable to simultaneously perform reflection and amplification functions. While the integrated phase shifters are dynamically adjusted to supply convenient phase shifts, the available power amplifiers can be turned ON and OFF according to incoming information bits to avoid excessive power consumption. Therefore, in the HRM scheme, in accordance with the incoming information bits, an RIS element can plainly reflect the incident signal without any amplification as a passive reflecting element or further amplify the reflected signal at the expense of increasing power consumption as an active reflecting element. On the other hand, by adapting the IM principle, the RIS is split into sub-groups, and the information is transmitted through different channel realizations created by various combinations of active and passive reflecting elements in these groups. Moreover, we perform a detailed theoretical analysis to obtain achievable rate expressions using an information theoretic approach and derive an upper bound for the ABEP of the system. Furthermore, we carry out a comprehensive numerical analysis under spatially correlated and uncorrelated channel conditions to illustrate the performance improvement of the HRM scheme over the prior RIS-aided benchmark schemes considering fully active [83] and fully passive [80, 95] RISs.

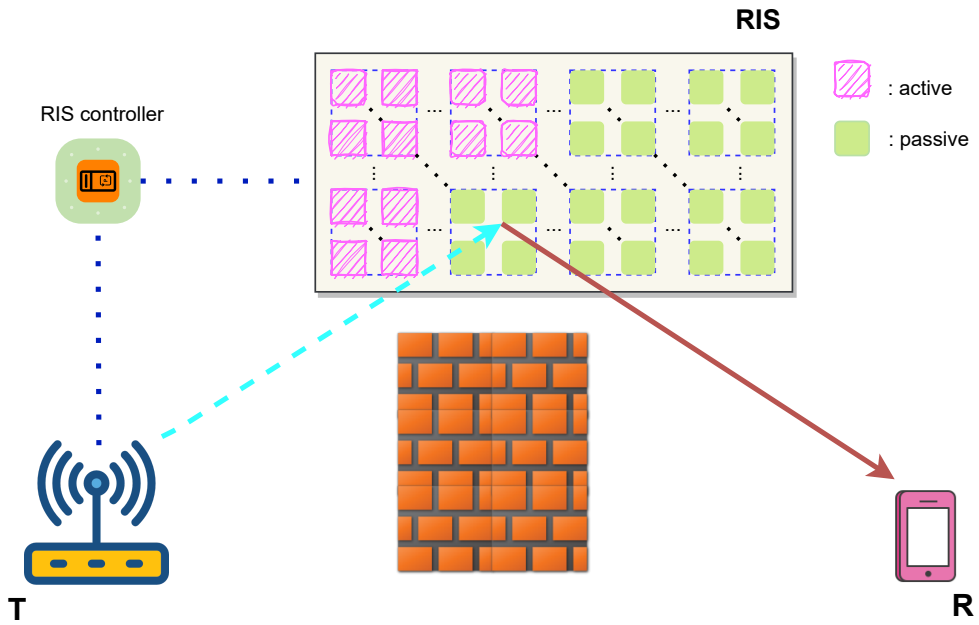

Figure 7.1 : System model of the HRM scheme.

The remaining of the chapter proceeds as follows. The system model of the proposed HRM scheme is given in Section 7.1. Section 7.2 provides theoretical performance analyses of the HRM scheme including ABEP, achievable rate and energy efficiency. In Section 7.3, computer simulation results are presented, and the conclusions are given in Section 7.4.

7.1 Hybrid Reflection Modulation

In this section, after giving the review of the classical passive and active RIS, we present the system model and the detection algorithm of the proposed HRM scheme.

7.1.1 Passive and active RIS

Most of the current literature on RIS-aided systems pays particular attention on RIS with passive reflecting elements in various research fields [7, 46–55, 94, 95]. By smartly inducing convenient phase shifts without any transmit power consumption [46], the passive RIS elements do not directly modify the magnitude of the incident signal. On the other hand, the active reflecting elements are capable of generating reflection gains of greater than unity at the cost of additional power consumption [83, 84]. This amplification functionality of a reflecting element can be achieved by integrating additional power amplifier circuitry such as tunnel diode [84] or low-noise amplifier (LNA) [83]. Therefore, unlike a passive reflecting element, each active

element introduces a non-negligible thermal noise. For instance, let $\xi_p = |\xi_p|e^{j\phi_p}$ and $\xi_a = |\xi_a|e^{j\phi_a}$ respectively represent the reflection gains of a passive and an active element whose magnitudes, ($|\xi_p|$, $|\xi_a|$) and phases (ϕ_p, ϕ_a) can be defined as follows

$$\phi_p \in [-\pi, \pi], \quad |\xi_p| \leq 1 \tag{7.1}$$

$$\phi_a \in [-\pi, \pi], \quad |\xi_a| > 1. \tag{7.2}$$

Nevertheless, although the active reflecting elements exploit power supplies in order to amplify the reflected signal, their hardware constructions are completely different from amplify-and-forward (AF) relays that utilize high-cost signal processing units.

7.1.2 HRM scheme

Adopting the IM principle, in the HRM scheme, we aim to modulate a single-tone carrier signal through RIS with reflective and power-controllable elements. As illustrated in Fig. 7.1, in the proposed HRM scheme, we consider a SISO system that employs an RIS with N reflecting elements to boost the communication link between the transmitter (T) and the receiver (R) in an outdoor environment.[1] In practical conditions, since it is unlikely to maintain a constant direct link between T-R link due to severe signal blockage in an outdoor environment, we assume that the direct link is blocked by the obstacles. Moreover, an RIS controller is incorporated with the RIS to dynamically adjust the phase shifts and the amplification gains of each reflecting element considering the information provided from the transmitter via a wireless control channel. For the sake of simplicity, we assume that perfect channel state information (P-CSI) of all nodes are available at the transmitter [46], which are conveyed to the RIS controller via the control link, and to the receiver through pilot-based transmission [111]. However, since the reflection amplitudes and phases are controlled separately, compared to fully passive RIS [82], the RIS controller requires additional variable resistor loads [112]. Subsequently, unlike the conventional passive elements that only utilize low-cost PIN diodes or varactors [94] to simply reflect signals without any amplification, the HRM scheme additionally includes a reflection-type power amplifier per RIS element to amplify the reflected signals in

[1]Since the MIMO extension of the proposed HRM scheme requires the development of a computationally intensive algorithm for optimization of reflection coefficients of the RIS elements, this paper considers a SISO transmission to avoid an additional computational burden at the RIS.

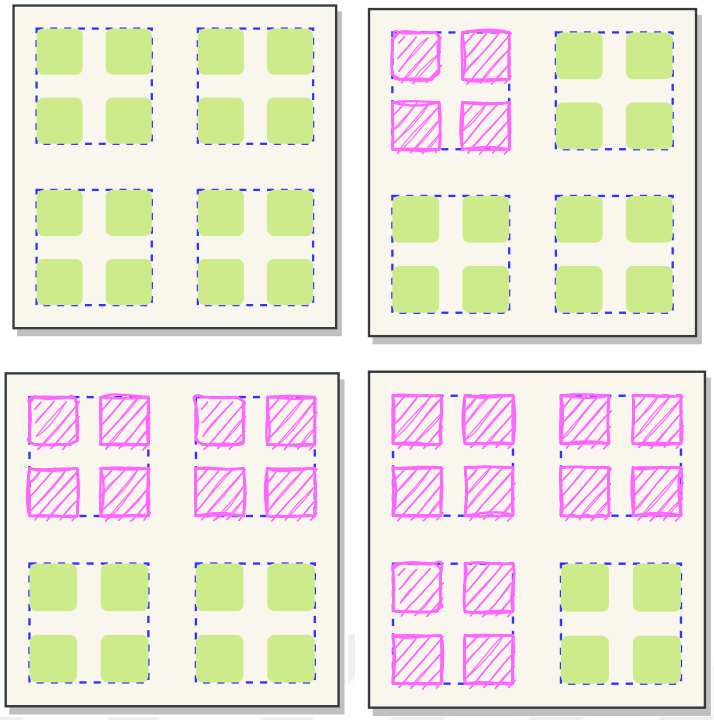

Figure 7.2 : An example of the proposed HRM scheme with an RIS of $N = 16$ elements and $G = 4$ sub-groups (active / passive).

order to attain further channel capacity gains [83]. In the HRM scheme, a phase shifter per each RIS element is employed to generate optimum phase shift for maximizing the signal-to-noise ratio (SNR), while reflection-type power amplifiers are dynamically turned ON/OFF according to the transmitted information bits. Therefore, similar to conventional RIS architecture, when the power amplification option is disabled, an RIS element can merely reflect the incident signal without any amplification, or when enabled, it can further amplify the signal with a convenient phase shift. Notably, the RIS element corresponds to a conventional *passive* reflecting element in the former case, while it is converted to an *active* reflecting element in the latter case.

In the proposed HRM scheme, the RIS with N reflecting elements is divided into G sub-groups, each having $S = N/G$ number of RIS elements. Then, applying the IM concept, the HRM scheme transmitting a single tone carrier signal requires $\log_2(G)$ information bits to employ the elements of l_A out of G groups as active reflecting elements while the remaining ones are used as passive reflecting elements, where $l_A \in \{0, 1, \ldots, G-1\}$. Therefore, the numbers of active and passive reflecting elements become $N_A = l_A \times S$ and $N_P = N - N_A$, respectively. In particular, for $l_A = 0$, since the power amplifiers of all reflecting elements are disabled, the RIS elements simply

Table 7.1 : Bit mapping of the HRM scheme with an RIS of $N = 16$ and $G = 4$ groups.

Information Bits	$\{00\}$	$\{01\}$	$\{10\}$	$\{11\}$
Number of active RIS groups (l_A)	0	1	2	3
HRM symbol ($\mathcal{H}_{l_A}$)	$\mathcal{H}_0$	$\mathcal{H}_1$	$\mathcal{H}_2$	$\mathcal{H}_3$

reflect signals without any amplification. In that case, the RIS serves as a conventional fully passive RIS.

Indeed, since active RIS elements further amplify the incident signal compared to the conventional passive reflecting elements, in the HRM scheme, exploiting a different number of active RIS elements in each time instant generates multi-level HRM symbols $\mathcal{H}_{l_A}$, like a virtual amplitude shift keying (ASK) modulator. Moreover, unlike the classical ASK modulator that utilizes a fully digital RF chain with high hardware complexity and implementation cost, in the proposed HRM scheme, employing an unmodulated cosine carrier at the transmitter, different combinations of active and passive reflecting elements are used to create a virtual ASK constellation. This also facilitates the HRM receiver to differentiate the perceived signal with a high accuracy.

To better illustrate, the HRM transmission scheme is explained with following example. In order to achieve a spectral efficiency of $\eta = 2$ bits/s/Hz, we assume that the proposed HRM transmission scheme employs an RIS with $N = 16$ elements divided into $G = 2^{\eta} = 4$ sub-groups, each of which consisting $S = 4$ RIS elements. While the active/passive RIS element combinations for the corresponding HRM symbols H_{l_A} are presented in Figure 7.2, the considered bit mapping is listed in Table 7.1, where $l_A \in \{0, 1, 2, 3\}$. As clearly seen from Figure 7.2, unlike the conventional fully passive [95] and fully active RISs [83] whose elements continuously operate in the same manner, in the proposed HRM scheme, via adjusting power amplifiers, different RIS configurations consisting of active and passive elements are formed in each time instant, which creates distinct variations in the amplitude of the over-the-air HRM symbols. Accordingly, for incoming $\{00\}$ bits, since the number of active RIS sub-groups is $l_A = 0$, $\mathcal{H}_0$ symbol is created by a fully passive RIS, while for the other incoming bit streams of $\{01\}$, $\{10\}$ and $\{11\}$, the HRM symbols are generated from hybrid RIS configurations consisting of both active and passive reflecting elements.

Clearly, the larger number of active sub-groups, the further RIS amplifies the incident signal.

Let $\xi_i = |\xi_i| e^{j\phi_i}$ be the reflection coefficient of the i-th reflecting element of the HRM scheme with magnitude $|\xi_i|$ and phase shift $\phi_i \in [-\pi, \pi]$, where $i \in \{1, 2, \cdots, N\}$. Then, for active and passive elements, the reflection coefficient ξ_i becomes

$$\xi_i = \begin{cases} p_i e^{j\phi_i} & i \in \{1, 2, \ldots, N_A\} \\ e^{j\phi_i} & \text{otherwise.} \end{cases} \tag{7.3}$$

It is worth noting that for the passive reflecting elements, the reflection gain is assumed to be $|\xi_i| = 1$ [95] while for the active reflecting elements, it is $|\xi_i| = p_i > 1$ [83–86, 110]. For simplicity, we assume that all active reflecting elements have the same reflection gain, i.e., $p_i = p$ for $\forall i \in \{1, 2, \ldots, N_A\}$. Accordingly, the reflection matrices including the phases of the active and passive elements can be respectively given as $\mathbf{\Phi} \in \mathbb{C}^{N_A \times N_A} = \text{diag}\left\{e^{j\phi_1}, e^{j\phi_2}, \ldots, e^{j\phi_{N_A}}\right\}$ and $\mathbf{\Psi} \in \mathbb{C}^{N_P \times N_P} = \text{diag}\left\{e^{j\phi_{N_A+1}}, e^{j\phi_{N_A+2}}, \ldots, e^{j\phi_N}\right\}$.

Let $\mathbf{h} \in \mathbb{C}^{1\times N} = \sqrt{L_t}\tilde{\mathbf{h}}$ and $\mathbf{g} \in \mathbb{C}^{1\times N} = \sqrt{L_r}\tilde{\mathbf{g}}$ be the channel vectors between the T-RIS and RIS-R links, respectively, where L_t and L_r are the path attenuation in the corresponding links. Here, the path loss terms are obtained for the T-RIS distance d_t and the RIS-R distance d_r as $L_t = \beta_0 d_t^{-\alpha_t}$ and $L_r = \beta_0 d_r^{-\alpha_r}$, where β_0 is the path loss at the reference distance of 1 meter (m), and α_t and α_r are the path loss exponents at the T-RIS and RIS-R links, respectively. Please note that T and R are located sufficiently away and operate independently, thus, the T-RIS and RIS-R links are statistically independent, where $\tilde{\mathbf{h}}$ and $\tilde{\mathbf{g}}$ are modeled as independent Rician fading channels and generated as

$$\tilde{\mathbf{h}} = \sqrt{\frac{K_t}{K_t+1}}\tilde{\mathbf{h}}_{\text{LOS}} + \sqrt{\frac{1}{K_t+1}}\tilde{\mathbf{h}}_{\text{NLOS}} \tag{7.4}$$

$$\tilde{\mathbf{g}} = \sqrt{\frac{K_r}{K_r+1}}\tilde{\mathbf{g}}_{\text{LOS}} + \sqrt{\frac{1}{K_r+1}}\tilde{\mathbf{g}}_{\text{NLOS}} \tag{7.5}$$

where $\tilde{\mathbf{h}}_{\text{LOS}}$ and $\tilde{\mathbf{g}}_{\text{LOS}}$ are the line-of-sight (LOS) components and $\tilde{\mathbf{h}}_{\text{NLOS}}$ and $\tilde{\mathbf{g}}_{\text{NLOS}}$ are non-LOS (NLOS) components of their corresponding channel vectors, while K_t and K_r are the Rician fading coefficients of the T-RIS and RIS-R links, respectively. Here, both the LOS and NLOS components are assumed to consist of complex Gaussian random variables, whose each entry is independent and identically distributed (i.i.d.) and follows $\mathcal{CN}(0, 1)$ distribution.

For a better illustration, the channel vectors between the T-RIS and RIS-R links can be given as $\mathbf{h} = [\mathbf{h}_a, \mathbf{h}_p]^{\mathrm{T}}$ and $\mathbf{g} = [\mathbf{g}_a, \mathbf{g}_p]$, respectively, where $\mathbf{h}_a \in \mathbb{C}^{1\times N_A}$ and $\mathbf{g}_a \in \mathbb{C}^{1\times N_A}$ are the channel vectors corresponding to the active elements, while the channel vectors $\mathbf{h}_p \in \mathbb{C}^{1\times N_P}$ and $\mathbf{g}_p \in \mathbb{C}^{1\times N_P}$ correspond to the passive reflecting elements at the RIS. Therefore, for P_{BS} being the total transmit power, the overall received complex baseband signal at the receiver becomes [83]:

$$y = \underbrace{\sqrt{P_{\mathrm{BS}}}\left(p\mathbf{g}_a\mathbf{\Phi}\mathbf{h}_a^{\mathrm{T}} + \mathbf{g}_p\mathbf{\Psi}\mathbf{h}_p^{\mathrm{T}}\right)}_{\text{reflected signal}} + \underbrace{p\mathbf{g}_a\mathbf{\Phi}\mathbf{v}^{\mathrm{T}}}_{\text{dynamic noise}} + n_s. \tag{7.6}$$

where $n_s \sim \mathcal{CN}(0, \sigma_{\mathrm{st}}^2)$ is the static noise term, while $\mathbf{v} \in \mathbb{C}^{1\times N_A} \sim \mathcal{CN}(\mathbf{0}, \mathbf{I}_{N_A}\sigma_{\mathrm{dy}}^2)$ is the additional noise vector composing the thermal noise terms generated by power amplifiers of active elements that cannot be neglected as in the passive elements.

In the HRM scheme, the phase shifts of the all reflection elements and the amplification gain of the active RIS elements p can be optimized in order to achieve the maximum SNR. Then, for P_A being the maximum amplification power at the RIS, which corresponds to the power budget of active reflecting elements [86], the maximum instantaneous received SNR can be formulated as

$$\max_{p,\mathbf{\Phi},\mathbf{\Psi}} \quad \gamma = \frac{P_{\mathrm{BS}}\left\|p\mathbf{g}_a\mathbf{\Phi}\mathbf{h}_a^{\mathrm{T}} + \mathbf{g}_p\mathbf{\Psi}\mathbf{h}_p^{\mathrm{T}}\right\|^2}{p^2\left\|\mathbf{g}_a\mathbf{\Phi}\right\|^2\sigma_{\mathrm{dy}}^2 + \sigma_{\mathrm{st}}^2} \tag{7.7}$$

$$\text{s.t.} \qquad p^2 P_{\mathrm{BS}}\left\|\mathbf{\Phi}\mathbf{h}_a^{\mathrm{T}}\right\|^2 + p^2\left\|\mathbf{\Phi}\right\|^2\sigma_{\mathrm{dy}}^2 \leq P_A. \tag{7.8}$$

Then, applying the triangle and Cauchy-Schwarz inequalities [108], since $p\|\mathbf{g}_a\|\|\mathbf{h}_a\| + \|\mathbf{g}_p\|\|\mathbf{h}_p\| \geq \|p\mathbf{g}_a\mathbf{\Phi}\mathbf{h}_a^{\mathrm{T}} + \mathbf{g}_p\mathbf{\Psi}\mathbf{h}_p^{\mathrm{T}}\|$, the optimum phase shift of the i-th reflecting element, ϕ_i, which completely eliminates the phases of the corresponding channel coefficients, and the reflection gain p are simply obtained as

$$\phi_i = -(\varphi_i + \chi_i) \quad \forall i \in \{1, 2, \ldots, N\} \tag{7.9}$$

$$p \leq \sqrt{\frac{P_A}{P_{\mathrm{BS}}\left\|\mathbf{h}_a\right\|^2 + \sigma_{\mathrm{dy}}^2}}. \tag{7.10}$$

Therefore, for $h_i = |h_i|\, e^{j\varphi_i}$ and $g_i = |g_i|\, e^{j\chi_i}$ respectively being the i-th component of the channel vectors $\mathbf{h}$ and $\mathbf{g}$, for the optimum phase shifts in (7.9) and an arbitrary amplification gain p, the received signal (7.6) can be rewritten as

$$y = \sqrt{P_{\mathrm{BS}}}\left(p\sum_{i=1}^{N_A}|h_i|\,|g_i| + \sum_{i=N_A+1}^{N}|h_i|\,|g_i|\right) + p\sum_{i=1}^{N_A}|g_i|\,\tilde{v}_i + n_s \tag{7.11}$$

where $\tilde{v}_i = v_i e^{-j\varphi_i}$, and v_i is the i-th complex element of the dynamic noise vector $\mathbf{v}$. Therefore, for $\mathcal{H}_{l_A} = p\sum_{i=1}^{N_A} |h_i|\,|g_i| + \sum_{i=N_A+1}^{N} |h_i|\,|g_i|$ being the HRM symbol for the corresponding l_A, the received signal can be rewritten as

$$y = \sqrt{P_{\text{BS}}}\mathcal{H}_{l_A} + n \tag{7.12}$$

where $n = p\sum_{i=1}^{N_A} |g_i|\,\tilde{v}_i + n_s$ is the overall noise term. It is worthy to note that applying the central limit theorem (CLT) for increasing N_A, n is approximated to a complex Gaussian random variable with $\sim \mathcal{CN}(0, N_0)$ distribution, where $N_0 = p^2 N_A L_r \sigma_{dy}^2 + \sigma_{\text{st}}^2$[2].

7.1.3 HRM receiver

In the HRM scheme, since exploiting different number of active reflecting elements creates virtual amplitude variations in the received signal, different signal levels of the HRM symbols can be easily distinguished at the receiver. Moreover, the HRM receiver with perfect knowledge of the overall channel considers ML detection algorithm to choose the most likely estimate of l_A, as follows

$$\hat{l}_A = \arg\max_{l_A} p(y|\mathcal{H}_{l_A}) \tag{7.13}$$

where $p(y|\mathcal{H}_{l_A})$ is the conditional probability density function (pdf) of the received signal y given $\mathcal{H}_{l_A}$, which can be given as

$$p(y|\mathcal{H}_{l_A}) = \frac{1}{\pi N_0} e^{\frac{-\left|y-\sqrt{P_{\text{BS}}}\mathcal{H}_{l_A}\right|^2}{N_0}}. \tag{7.14}$$

Here, the overall noise power N_0, where it is obtained as $N_0 = p^2 N_A L_r \sigma_{dy}^2 + \sigma_{\text{st}}^2$ in the previous subsection, and the HRM symbol H_{l_A} vary with the number of active sub-groups of RIS (l_A) and the total number of active reflecting elements N_A. However, since the thermal noise of each active element experiences the path attenuation of the RIS-R link (L_r) while the RIS-R distance of d_r is sufficiently large, the varying N_A hardly affects the decision of minimum metrics in (7.14). Therefore, the HRM receiver can simply detect l_A as follows

$$\hat{l}_A = \arg\min_{l_A} \left|y - \sqrt{P_{\text{BS}}}\mathcal{H}_{l_A}\right|^2 \tag{7.15}$$

[2]For X and Y being independent random variables, the variance of the product $Z = XY$ is calculated as $\sigma_Z^2 = \sigma_X^2\sigma_Y^2 + \mu_X^2\sigma_Y^2 + \mu_Y^2\sigma_X^2$ and the mean of Z is $\mu_Z = \mu_X\mu_Y$. In addition, the mean and variance of the sum $W = X + Y$ are $\mu_W = \mu_X + \mu_Y$ and $\sigma_W^2 = \sigma_X^2 + \sigma_Y^2$, respectively.

which gives as almost the same estimate as the ML algorithm given in (7.13). Here, we consider all combinations of active and passive elements and simply select the closest virtual constellation point with respect to received signal.

7.1.4 Fully hybrid reflection modulation (F-HRM)

In this subsection, a special case of the proposed HRM scheme, fully hybrid reflection modulation (F-HRM), is introduced. In the F-HRM scheme, the same RIS, transmitter and receiver hardware architectures of the HRM scheme are considered. However, unlike HRM, in the F-HRM scheme, whole RIS elements without grouping are assumed to manipulate the incident signal in the same manner. Specifically, in the F-HRM scheme, 1-bit information ($\eta = 1$ bits/s/Hz) is transmitted over the RIS to control the amplification gains of the RIS elements. In the F-HRM scheme, by properly adjusting the power amplifier of each reflecting element, for the incoming $\{0\}$ bit, all reflecting elements perform a plain passive reflection with the optimum phase shifts of (7.9), while for the incoming bit $\{1\}$, all elements function as active reflecting elements that amplify and reflect the incident signal with additional thermal noise. Please note that, in the F-HRM scheme, since RIS elements operate in the same manner as a whole, the number of the overall active reflection elements is $N_A = l_A \times N$ for $_A \in \{0, 1\}$. Accordingly, in the F-HRM scheme, for the corresponding l_A and N_A values, the received signal, the optimum estimate of l_A at the receiver and the maximum received SNR can be obtained from (7.11), (7.15) and (7.7)-(7.10), respectively.

7.2 Performance Analyses

In this section, we investigate the performance of the proposed HRM in terms of ABEP, achievable rate and energy efficiency.

7.2.1 ABEP analysis

In this subsection, the ABEP of the proposed HRM scheme is analyzed. Since the simple HRM detection algorithm in (7.15) gives exactly the same error performance as the true ML detector in (7.13), we build our theoretical analysis based on it in the following way.

After the PEP of the HRM scheme is obtained, we derive the ABEP of the system using an MGF-based approach [102]. For this purpose, first of all, in order to determine the CPEP of the HRM scheme, we assume that the number of sub-groups of active elements l_A and its corresponding total number of active elements $N_A = l_A \times S$ are erroneously detected as $\hat{l}_A$ and $\hat{N}_A = \hat{l}_A \times S$, respectively. Therefore, considering the detection rule in (7.15), the CPEP of the HRM scheme can be given as

$$P_r\left(l_A \to \hat{l}_A|\mathbf{h},\mathbf{g},\Phi,\Psi\right) = P_r\left(\left|y-\sqrt{P_{\text{BS}}}(\mathcal{H}_{l_A})\right|^2 - \left|y-\sqrt{P_{\text{BS}}}(\mathcal{H}_{\hat{l}_A})\right|^2 > 0\right) \tag{7.16}$$

where $\mathcal{H}_{\hat{l}_A} = p\sum_{j=1}^{\hat{N}_A}|h_j||g_j| + \sum_{j=\hat{N}_A+1}^{N}|h_j||g_j|$ is the HRM symbol for the corresponding $\hat{l}_A$. Therefore, the CPEP in (7.16) can be simplified to:

$$\begin{aligned}
&P_r\left(l_A \to \hat{l}_A|\mathbf{h},\mathbf{g},\Phi,\Psi\right) = \\
&P_r\Big(P_{\text{BS}}\left|\mathcal{H}_{l_A}\right|^2 - 2\sqrt{P_{\text{BS}}}\Re\left\{\left(\sqrt{P_{\text{BS}}}\mathcal{H}_{l_A}+n\right)^{\text{H}}\mathcal{H}_{l_A}\right\} \\
&\qquad > P_{\text{BS}}\left|\mathcal{H}_{\hat{l}_A}\right|^2 - 2\sqrt{P_{\text{BS}}}\Re\left\{\left(\sqrt{P_{\text{BS}}}\mathcal{H}_{l_A}+n\right)^{\text{H}}\mathcal{H}_{\hat{l}_A}\right\}\Big).
\end{aligned} \tag{7.17}$$

After some mathematical manipulations, the CPEP expression in (7.17) can be rewritten as

$$P_r\left(l_A \to \hat{l}_A|\mathbf{h},\mathbf{g},\Phi,\Psi\right) = P_r\Big(-P_{\text{BS}}\left|\mathcal{H}_{l_A}-\mathcal{H}_{\hat{l}_A}\right|^2 - 2\Re\left\{\sqrt{P_{\text{BS}}}n^{\text{H}}\left|\mathcal{H}_{l_A}-\mathcal{H}_{\hat{l}_A}\right|\right\} > 0\Big). \tag{7.18}$$

Therefore, for D being a Gaussian random variable with $D = -P_{\text{BS}}\left|\mathcal{H}_{l_A}-\mathcal{H}_{\hat{l}_A}\right|^2 - 2\Re\left\{\sqrt{P_{\text{BS}}}n^{\text{H}}\left|\mathcal{H}_{l_A}-\mathcal{H}_{\hat{l}_A}\right|\right\}$, the CPEP expression yields in

$$P_r\left(l_A \to \hat{l}_A|\mathbf{h},\mathbf{g},\mathbf{\Phi},\mathbf{\Psi}\right) = P_r(D>0) \tag{7.19}$$

where the mean and the variance of D are calculated as $\mu_D = -P_{\text{BS}}\left|\mathcal{H}_{l_A}-\mathcal{H}_{\hat{l}_A}\right|^2$ and $\sigma_D^2 = 2P_{\text{BS}}N_0\left|\mathcal{H}_{l_A}-\mathcal{H}_{\hat{l}_A}\right|^2$. After deriving the statistical distributions, the CPEP expression can be given, using Q-function, as

$$P_r\left(l_A \to \hat{l}_A|\mathbf{h},\mathbf{g},\Phi,\Psi\right) = Q\left(\sqrt{\frac{P_{\text{BS}}\left|\mathcal{H}_{l_A}-\mathcal{H}_{\hat{l}_A}\right|^2}{2N_0}}\right). \tag{7.20}$$

In the HRM scheme, the channel magnitudes of $|h_i|$ and $|g_i|$ are independent Rician distributed random variables with the means of $\mu_{|h_i|} = \frac{1}{2}\sqrt{\frac{L_t\pi}{K_t+1}}L_{1/2}(-K_t)$ and

$\mu_{|g_i|} = \frac{1}{2}\sqrt{\frac{L_r\pi}{K_r+1}}L_{1/2}(-K_r)$, and the variances of $\sigma^2_{|h_i|} = L_t - \frac{L_t\pi}{4(K_t+1)}L^2_{1/2}(-K_t)$ and $\sigma^2_{|g_i|} = L_r - \frac{L_r\pi}{4(K_r+1)}L^2_{1/2}(-K_r)$, where $L_{1/2}(\cdot)$ is the Laguerre polynomial [113]. Then, defining $\Sigma = \mathcal{H}_{l_A} - \mathcal{H}_{\hat{l}_A}$, which is another Gaussian random variable with the following statistics

$$\begin{aligned}\mu_\Sigma &= \sqrt{L_tL_r}\frac{\pi}{4}\sqrt{\frac{1}{(K_t+1)(K_r+1)}} \\ &\qquad \times L_{1/2}(-K_t)L_{1/2}(-K_r)\times(p\delta-\delta) \\ \sigma^2_\Sigma &= \left(L_tL_r-\mu^2_\Sigma\right)\times\left(p^2\delta-\delta\right)\end{aligned} \tag{7.21}$$

for $\delta = (N_A - \hat{N}_A)$ the average error probability of the system is calculated in the following way. Considering the following alternative representation of Q-function

$$Q(t) = \frac{1}{\pi}\int_0^{\pi/2}\exp\left(\frac{-t^2}{\sin^2(\theta)}\right)d\theta \tag{7.22}$$

and using the MGF of $\Pi = |\Sigma|^2$, which follows non-central chi-square distribution, the average PEP can be calculated as follows

$$P_r\left(l_A\to\hat{l}_A\right) = \frac{1}{\pi}\int_0^{\pi/2}\mathcal{M}_\Pi\left(-\frac{P_t}{2N_0\sin^2(\theta)}\right)d\theta. \tag{7.23}$$

Here, the MGF of non-central chi-square distribution is given as [114]

$$\mathcal{M}_\Pi(s) = \frac{1}{\sqrt{1-\sigma^2_\Sigma s}}\exp\left(\frac{\mu^2_\Sigma s}{1-\sigma^2_\Sigma s}\right). \tag{7.24}$$

Therefore, substituting the MGF expression (7.24) into (7.25), the PEP is obtained as

$$\begin{aligned}&P_r\left(l_A\to\hat{l}_A\right) = \\ &\frac{1}{\pi}\int_0^{\pi/2}\frac{1}{\sqrt{1+\frac{\sigma^2_\Sigma P_t}{4N_0\sin^2(\theta)}}}\exp\left(\frac{-\frac{\mu^2_\Sigma P_t}{4N_0\sin^2(\theta)}}{1+\frac{\sigma^2_\Sigma P_t}{4N_0\sin^2(\theta)}}\right)d\theta.\end{aligned} \tag{7.25}$$

To gain further insights, since a function of $z(\theta) = 1/\sin^2(\theta)$ has a single minimum at $\theta = \pi/2$, where $z(\pi/2) = 1$, by letting $\theta = \pi/2$, (7.25) can be upper bounded as follows [102]

$$P_r\left(l_A\to\hat{l}_A\right) \le \frac{1}{2}\frac{1}{\sqrt{1+\frac{\sigma^2_\Sigma P_t}{4N_0}}}\exp\left(\frac{-\frac{\mu^2_\Sigma P_t}{4N_0}}{1+\frac{\sigma^2_\Sigma P_t}{4N_0}}\right). \tag{7.26}$$

Moreover, for high P_t/N_0 regime, an asymptotic PEP expression can be approximated as:

$$P_r\left(l_A \to \hat{l}_A\right) \approx \frac{P_t}{4N_0} L_r L_t (p^2\delta - \delta) \times \left[1 - \left(\frac{\pi^2/16}{(K_t+1)(K_r+1)} L_{1/2}^2(-K_t) L_{1/2}^2(-K_r)\right)\right]^{-\frac{1}{2}} \times \exp\left(\frac{-\pi^2 L_{1/2}^2(-K_t) L_{1/2}^2(-K_r)(p-1)^2\delta}{16(K_t+1)(K_r+1) - \pi^2 L_{1/2}^2(-K_t) L_{1/2}^2(-K_r)(p^2-1)}\right). \tag{7.27}$$

It is worth noting that for $G = 2$, the PEP results the ABEP of the HRM scheme, while for $G \geq 2$ the following well-known upper bound is considered [102]:

$$P_b \leq \frac{1}{m} \sum_{l_A} \frac{1}{2^m} \left[\sum_{\hat{l}_A} P_r\left(l_A \to \hat{l}_A\right) e(l_A, \hat{l}_A)\right] \tag{7.28}$$

where $e(l_A, \hat{l}_A)$ is the number of bit errors in each PEP event.

7.2.2 Achievable rate analysis

In this subsection, considering an information theoretic approach, we perform achievable rate analysis of the HRM scheme by deriving the mutual information between its transmit and received signals.

In the HRM scheme, since the an unmodulated carrier signal is transmitted and the information bits are modulated to generate a spatial constellation symbol $\mathcal{H}_{l_A}$, the mutual information of the HRM scheme corresponds to the information conveyed between the received signal vector space $\mathbf{Y}$ and spatial constellation space $\mathcal{H}$. Therefore, the achievable rate of the proposed HRM scheme becomes [114]

$$I(\mathcal{H}; \mathbf{Y}) = \int_{-\infty}^{\infty} p(y|\mathcal{H}_{l_A}) p(\mathcal{H}_{l_A}) \times \log_2 \left(\frac{p(y|\mathcal{H}_{l_A})}{\sum_{\hat{l}_A} p(y|\mathcal{H}_{\hat{l}_A}) p(\mathcal{H}_{l_A})}\right) dy. \tag{7.29}$$

Here, since each HRM symbol $\mathcal{H}_{l_A}$ is equiprobable, i.e., $p(\mathcal{H}_{l_A}) = 1/G$, substituting the conditional pdf of $p(y|\mathcal{H}_{l_A})$ given in (7.14) into (7.29), the achievable rate of the HRM scheme is rewritten as

$$I(\mathcal{H}; \mathbf{Y}) = = \log_2(G) - \frac{1}{G}\left\{\frac{1}{\pi N_0} \sum_{l_A} \int e^{\frac{-\left|y - \sqrt{P_{\text{BS}}}\mathcal{H}_{l_A}\right|^2}{N_0}} \times \log_2\left(\sum_{\hat{l}_A} e^{\frac{\left|y - \sqrt{P_{\text{BS}}}\mathcal{H}_{l_A}\right|^2 - \left|y - \sqrt{P_{\text{BS}}}\mathcal{H}_{\hat{l}_A}\right|^2}{N_0}}\right) dy\right\}. \tag{7.30}$$

Therefore, after some algebraic manipulations, (7.30) can be simplified to [115]

$$I(\mathcal{H};\mathbf{Y}) = \log_2(G) - \log_2(e) - \frac{1}{G}\sum_{l_A}\mathbb{E}\left\{\log_2\left(\sum_{\hat{l}_A} e^{\frac{-\left|\sqrt{P_{\text{BS}}}(\mathcal{H}_{l_A}-\mathcal{H}_{\hat{l}_A})+n\right|^2}{N_0}}\right)\right\}. \quad (7.31)$$

7.2.3 Energy efficiency

In this subsection, the power consumption model and energy efficiency of the proposed HRM scheme are evaluated. In the HRM scheme, for τ_t being the transmit power efficiency, its average power consumption can be calculated as

$$P_T = \frac{P_{\text{BS}}}{\tau_t} + P_{\text{RIS}} + P_c \quad (7.32)$$

where P_c represents the overall power dissipated in transmitter and receiver circuit blocks while P_{RIS} denotes the total power consumption of the RIS that can be given, for ϵ_1 and ϵ_2 respectively denoting the average number of active and passive reflecting elements, as follows:

$$P_{\text{RIS}} = \frac{P_A}{\tau_a} + \epsilon_1 P_{\text{dy}} + \epsilon_2 P_p + P_{\text{st}} \quad (7.33)$$

In (7.33), P_{dy} and P_{st} correspond to dynamic and static power consumption of the active reflecting elements, respectively, while P_p is the required power per passive reflecting element [86], and τ_a is amplifier efficiency of the active reflecting elements for $\tau_a, \tau_t \in (0, 1]$ [86]. On the other hand, when a conventional RIS of N passive reflecting elements is considered, P_{RIS} corresponds to the power consumed by the adaptive phase shifters, i.e. $P_{\text{RIS}} = NP_p$ [48], while for fully active RIS, whose elements include both reflection and amplification circuitry, the overall power consumed by the RIS becomes $P_{\text{RIS}} = \frac{P_A}{\tau_a} + NP_{\text{dy}} + P_{\text{st}}$ [86]. Comparing the power consumption of the proposed hybrid, fully active and fully passive RIS configurations, with the note that $P_p \ll P_{dy}$, it is obvious that fully passive RIS architectures with only reflection capabilities are the most power-efficient constructions. On the other hand, in the proposed HRM scheme, the hybrid RIS architectures save a significant amount of power compared to the fully active RIS designs.

Further, the energy efficiency in bits per Joule (bits/J) of the HRM system results, in terms of instantaneous received SNR γ given in (7.7), can be obtained as

$$E_e = \frac{B_W}{P_T}\log_2(1+\gamma) \quad (7.34)$$

where B_W represents the system bandwidth.

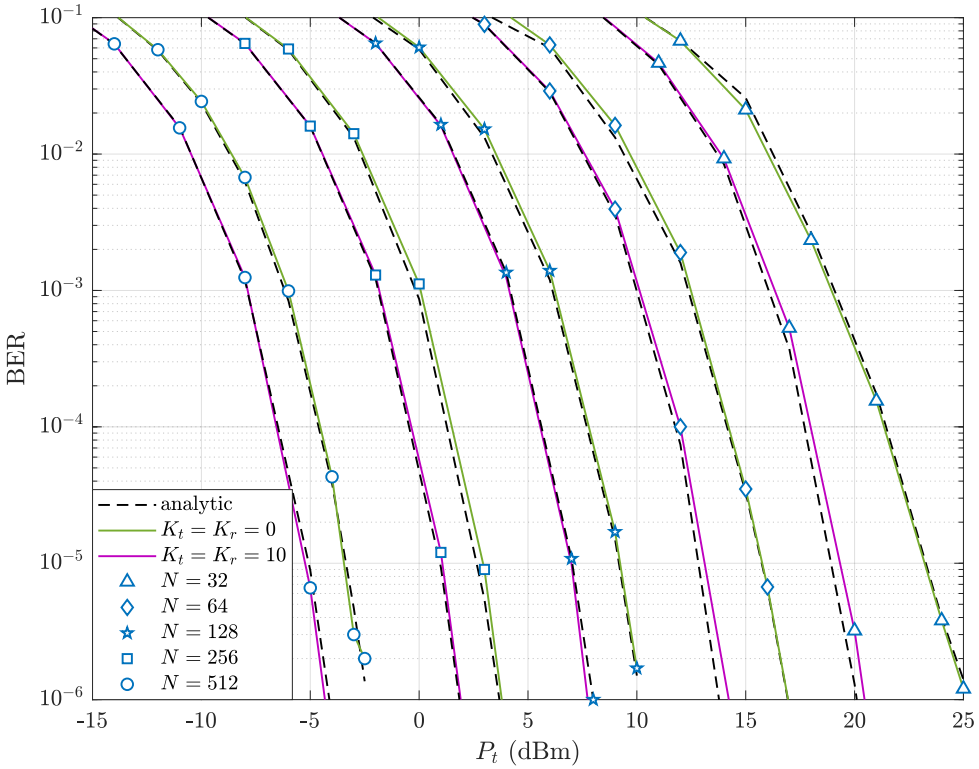

Figure 7.3 : Analytical and simulation results of the HRM scheme for different N values.

7.3 Numerical Results

In this section, the BER, achievable rate and energy efficiency performance of the proposed HRM scheme is investigated through extensive computer simulations. For the different number of RIS sub-groups and reflecting elements, the superior performance of the proposed HRM scheme over the existing fully active [83], fully passive [95] and RM [80] schemes is demonstrated. Unless otherwise indicated, in all simulations, the following system parameters are assumed: the distances $d_t = 20$ m and $d_r = 50$ m, the path loss exponents $\alpha_t = 2.2$ and $\alpha_r = 2.8$, the noise variances $\sigma^2_{\text{dy}} = \sigma^2_{\text{st}} = -90$ dBm, the Rician shape parameters $K_t = K_r = \{0\}$ and the reference path loss value of $\beta_0 = -30$ dB.

7.3.1 BER performance in ideal channel conditions

In this subsection, the BER performance of the proposed HRM scheme under the ideal channel conditions is carried out.

In Figure 7.3, the analytical and numerical results of the BER performance of the HRM scheme with $p = 10$, which achieves a spectral efficiency of $\eta = 1$ bits/s/Hz

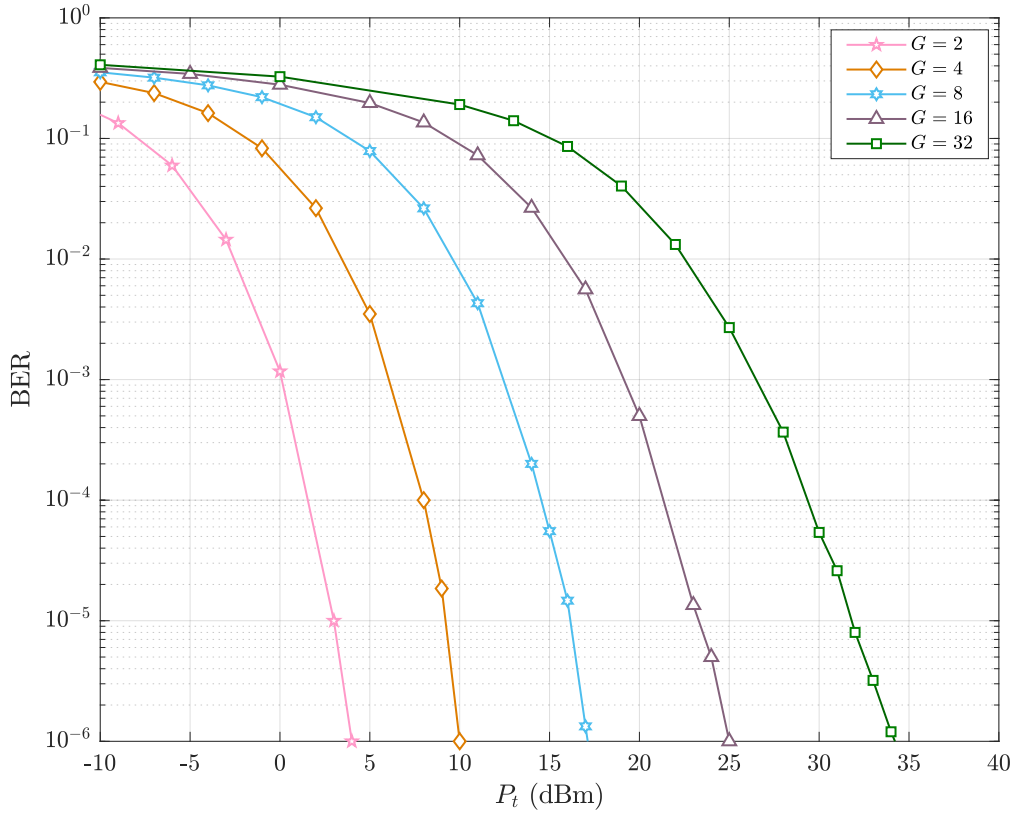

Figure 7.4 : BER results of the HRM scheme with $N = 256$ divided into G sub-groups.

for $G = 2$ and Rician scale factors of $K_t = K_R \in \{0, 10\}$, is demonstrated. As it can be clearly seen from Figure 7.3, the analytical results applying the CLT for increasing N perfectly match to computer simulations for $N \in \{32, 64, 128, 256, 512\}$. Moreover, it is observed that for each $K_t = K_r$, doubling the reflection elements provides approximately 7.5 dBm improvement in the required transmit power P_{BS} at the BER value of 10^{-6}.

In Figure 7.4, the BER performance of the HRM scheme is given for $N = 256$ reflecting elements divided into $G = 2, 4, 8, 16$ and 32 sub-groups. It is observed that like the ordinary multi-level digital modulation techniques, as the number of sub-groups is increased the signal levels of the HRM symbols get closer, and this deteriorates the BER performance of the HRM scheme. In particular, it is apparent that the HRM scheme achieving $m = 5$ bits/s/Hz ($m = \log_2(G)$) with an RIS of $G = 32$ sub-groups exhibits remarkably worse error performance compared to the lower G cases, which shows an interesting trade-off between the error performance and the spectral efficiency. Moreover, as in the classical ASK modulation, considering the reflection power constraint in (8), since the same p and N values are considered in Fig.

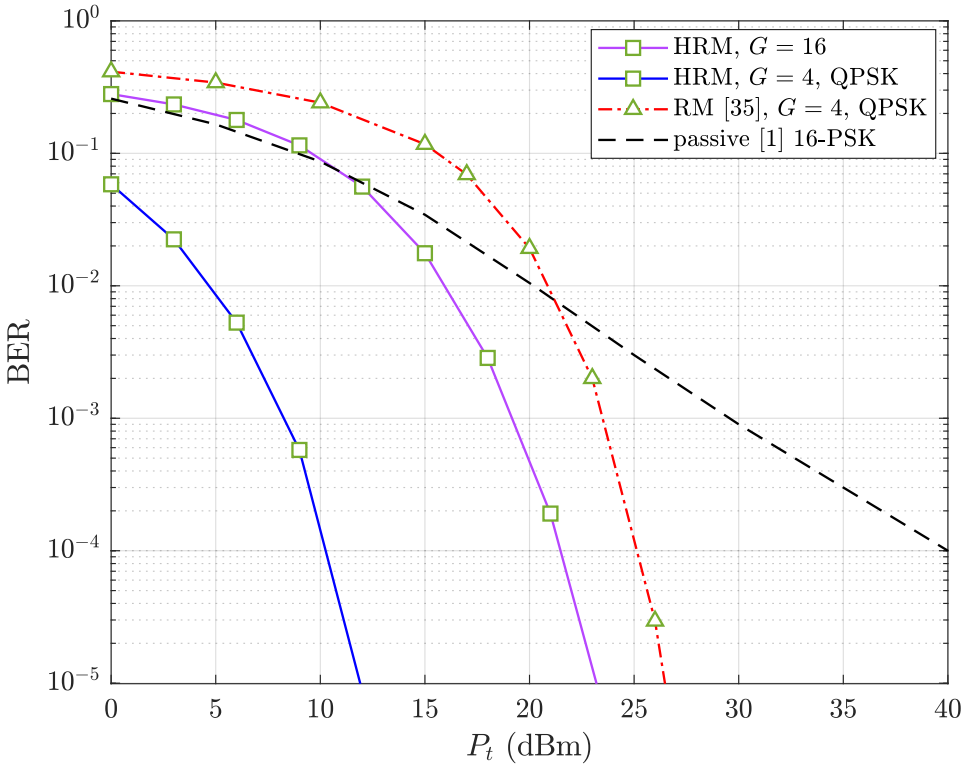

Figure 7.5 : BER performance comparison of the HRM, RM and conventional fully passive RIS-aided schemes for optimum phase shifts.

4, the systems with larger G necessitate a higher power consumption. Therefore, it can be concluded that besides their superior error performance, the HRM systems with a smaller G save more energy than the systems with a larger G.

In Figure 7.5, the BER performance comparison of HRM, RM [80] and conventional fully passive RIS-aided systems is investigated for $N = 256$. In the reference RM scheme [80], similar to HRM, an RIS with fully passive reflecting elements, is split into G sub-groups whose indices are used to convey additional information bits. However, contrary to HRM and conventional fully passive RIS-aided systems, adjusting ON/OFF keying states of each group, the whole RIS elements are not utilized in the reference RM transmission scheme [80]. Moreover, in the reference RM scheme [80], an RF source is used to transmit an optimized M-PSK constellation per each RIS configuration to achieve a spectral efficiency of $\eta = \log_2(G) + \log_2(M)$. Then, in Figure 7.5, to attain $\eta = 4$ bits/s/Hz, considering the optimum phase shifts in (7.9), the HRM scheme with $G = 16$ sub-groups and the amplification gain of $p = 10$ is compared to the reference fully passive RIS-aided system with 16-PSK, and the RM scheme with $G = 4$ sub-groups employing the rotated quadrature PSK (QPSK) [80]. The results show that although the HRM scheme with $G = 16$ enlarges the HRM

signal constellation considerably, it still achieves significant performance over the RM [80] and conventional fully passive RIS-aided system. Furthermore, in Figure 7.5, at $\eta = 4$ bits/s/Hz, as an extension of the HRM scheme, the BER performance of HRM that jointly encodes information in the transmit signal and RIS sub-groups is also evaluated. In this case, while preserving the RIS and receiver architecture of the proposed HRM, instead of an unmodulated signal, a QPSK modulated signal is employed at the transmitter of the HRM scheme. For the case of the HRM scheme with M-PSK modulation, the spectral efficiency becomes $\eta = \log_2(M) + \log_2(G)$ bits/s/Hz. Therefore, in order to achieve a spectral efficiency of $\eta = 4$ bits/s/Hz, for $p = 10$ and QPSK signaling, the RIS is clustered into $G = 4$ sub-groups. The results exhibit that the HRM scheme with $G = 4$ and QPSK signal transmission achieves 16 dB P_{BS} gain at the BER value of 10^{-5} over the reference RM scheme [80]. It is clear from the Figure 7.5 that using an additional RF chain at the transmitter alleviates the burden of RIS transmission by reducing the required number of RIS sub-groups. In that case, since the benefits of a lower HRM signal level are retained, the BER performance improves, but it brings an additional hardware cost.

7.3.2 BER Performance in non-ideal channel conditions

In this subsection, the BER performance of the ideal and non-ideal channel conditions is compared for different RIS configurations.

Further, for more realistic settings, we investigate the performance of the HRM scheme under the spatially correlated RIS elements whose impact on the BER performance is given in Figure 7.6. For this aim, we consider a square RIS and assume that the channel vectors $\mathbf{h}$ and $\mathbf{g}$, representing T-RIS and RIS-R links, respectively, are modeled as spatially correlated Rayleigh fading channels, i.e., $K_t = K_r = 0$ in (7.4) and (7.5), and generated as

$$\mathbf{h} = \sqrt{L_t}\tilde{\mathbf{h}}_{\text{NLOS}}\mathbf{R}^{1/2} \tag{7.35}$$

$$\mathbf{g} = \sqrt{L_r}\tilde{\mathbf{g}}_{\text{NLOS}}\mathbf{R}^{1/2} \tag{7.36}$$

where $\mathbf{R} \in \mathbb{C}^{N\times N}$ is the correlation matrix due to spatially correlated RIS elements, whose (k,l)-th component is $[\mathbf{R}]_{k,l} = \text{sinc}(2\left\|\mathbf{c}_k - \mathbf{c}_l\right\|/\lambda)$ [116, 117], for $k,l \in \{1,2,\cdots,N\}$ and λ being the wavelength at 2.4 GHz operating frequency. Here, the horizontal width and vertical height of a single reflecting element

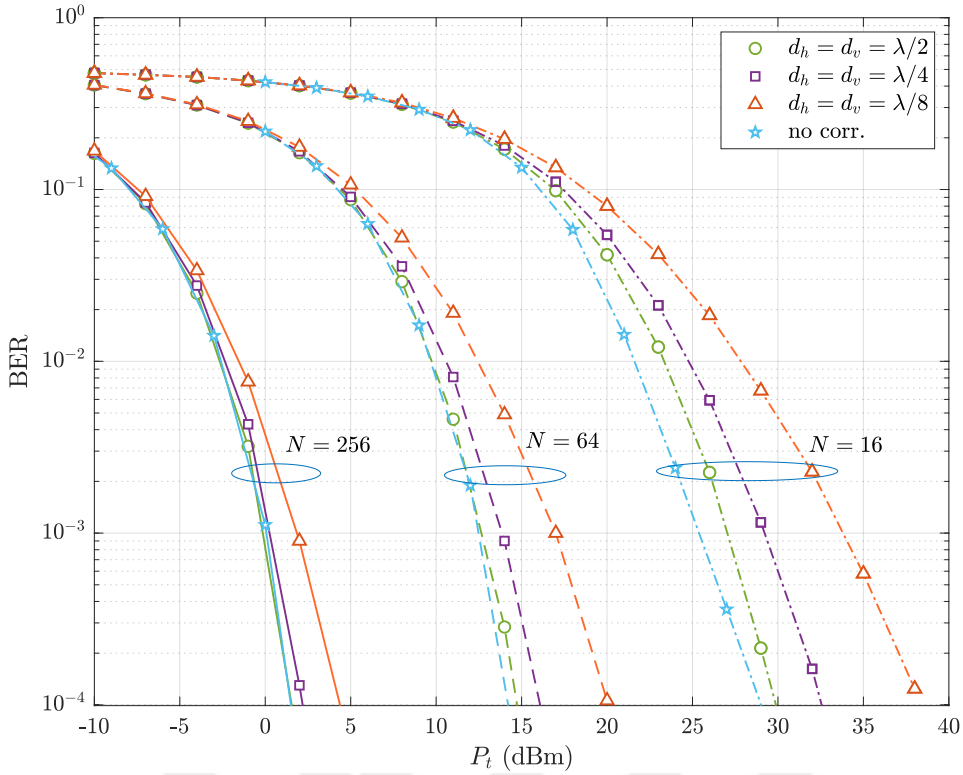

Figure 7.6 : BER results of the HRM scheme for correlated channel conditions.

are represented by d_h and d_v, respectively, and for $i \in \{k, l\}$, the vector $\mathbf{c}_i = [0, \mod(i-1, N_h)d_h, \lfloor (i-1)/N_h \rfloor d_v]^{\mathrm{T}}$, where N_h is the number of reflecting elements in each row or column of the square RIS, i.e., $N = N_h \times N_h$.

In Fig 7.6, the BER performance of HRM scheme under spatially correlated and spatially independent channel conditions is given for the squared RIS elements with different dimensions of $d_h = d_v \in \{\lambda/2, \lambda/4, \lambda/8\}$ at the spectral efficiency of $\eta = 1$ bits/s/Hz. The results show that the configuration of the RIS has a great impact on the degree of correlation. Therefore, as the horizontal and vertical sizes of the RIS elements enlarge, the HRM system becomes more robust to the bit errors. Moreover, it can also be deduced that increasing number of reflecting elements significantly facilitates the BER performance degradation of channel correlation. As it can be clearly seen from the Figure 7.6, the HRM scheme with $N = 256$ exhibits almost the same BER performance in both spatially correlated RIS with $d_h = d_v = \lambda/2$ and spatially independent RIS cases. However, for the lower N values, i.e., $N = 16$ and $N = 64$, the spatial correlation causes a considerable deterioration in the BER performance.

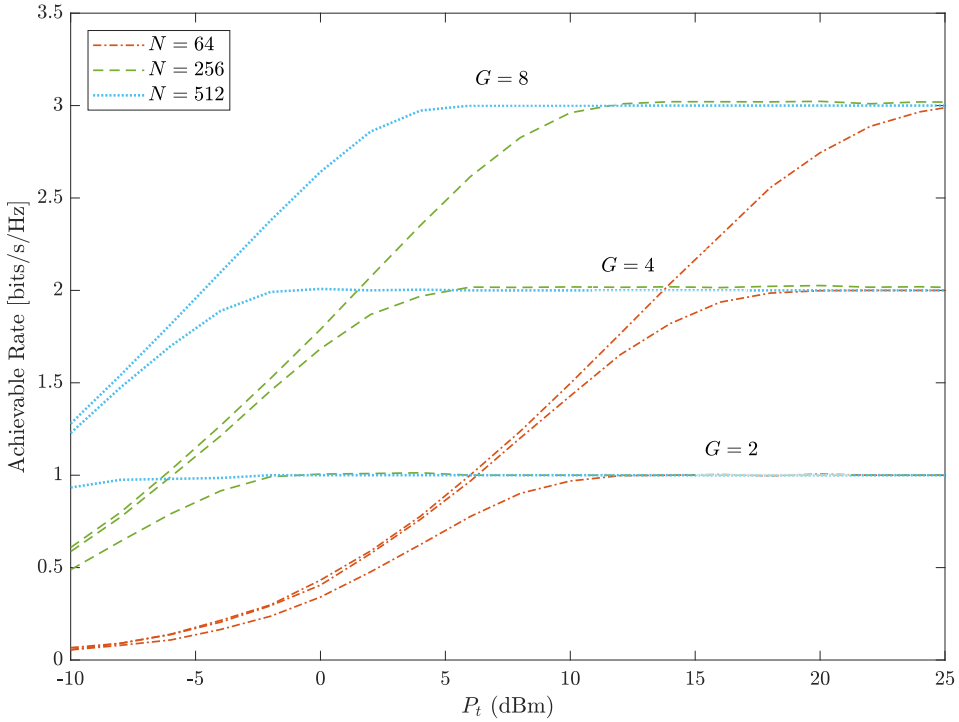

Figure 7.7 : Achievable rate of the HRM scheme for different N and G values.

7.3.3 Achievable rate and energy efficiency performance

In this subsection, the achievable rate and the energy efficiency performances of the proposed HRM scheme and the fully passive and fully active RIS-aided systems are compared through extensive computer simulations.

Figure 7.7 provides the achievable rate of the HRM scheme with the amplification gain of the active elements being $p = 10$. In this figure, the RIS with $N = 64, 256$ and 512 reflecting elements are divided into $G = 2, 4$ and 8 sub-groups that achieve the spectral efficiency values of $\eta = 1, 2$ and 3 bits/s/Hz, respectively. These information-theoretic results illustrate that increasing number of reflecting elements, N, enables a more rapid convergence to the target data rate.

Furthermore, in Figure 7.8, we investigate the energy efficiency and power consumption of F-HRM, fully active [83] and fully passive RIS-aided schemes [95] at the spectral efficiency of 1 bits/s/Hz. At the transmitter, while in the F-HRM scheme, an unmodulated carrier signal is considered, binary PSK (BPSK) modulation is employed in the fully passive and fully active RIS-aided systems. Notably, in the F-HRM scheme, the average number of active and passive elements are equal as

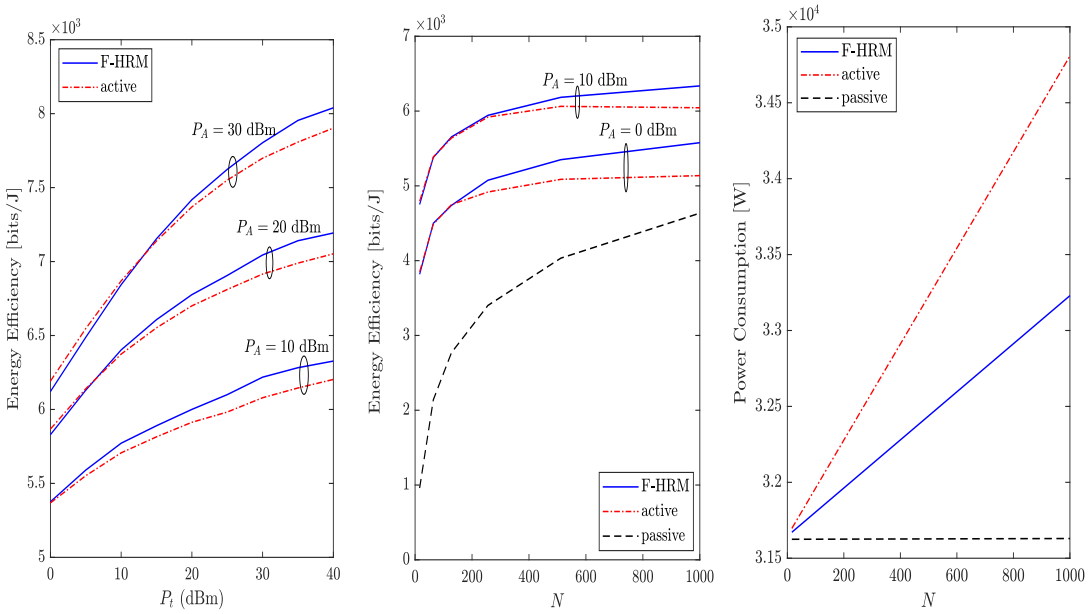

Figure 7.8 : Comparison of the HRM, active and passive RIS schemes in terms of (a)-(b) energy efficiency and (c) power consumption.

$\epsilon_1 = \epsilon_2 = N/2$. Therefore, to evaluate the total power consumption in (7.33), we set $P_c = 75$ dBm, $P_p = 5$ mW, $P_{\text{st}} = 35$ dBm, $P_{\text{dy}} = 30$ dBm, and $\tau_a = \tau_t = 0.5$ [86], and assume $B_W = 10$ MHz [48] to determine the energy efficiency of (7.34) by 10^6 number of iterations.

In Figure 7.8(a), the energy efficiency of F-HRM and active RIS-aided transmission schemes, all employing $N = 512$ reflecting elements at the RIS, is measured as a function of P_{BS}. The results indicate a considerable energy efficiency improvement for the F-HRM scheme over the active RIS-aided system for $P_A = 10, 20$ and 30 dBm. These results can be explained by the fact that although a fully active RIS-aided system achieves substantial capacity gains [83, 85], it requires larger amount of power compared to the more environment-friendly F-HRM scheme.

In addition, in Figure 7.8(b), the energy efficiency of the F-HRM and active and passive RIS-aided systems are further investigated for varying N values and the amplification power of $P_A = 0$ and 10 dBm, as well as for the transmit power $P_{\text{BS}} = 30$ dBm. Consistent with the results in Figure 7.8(a), the F-HRM scheme achieves a noticeable improvement in the energy efficiency compared to fully active RIS-aided system, and exceeds the conventional passive RIS-aided system with a substantial margin. To support these results, in Figure 7.8(c), the power consumption of the proposed

F-HRM scheme and the reference RIS-aided systems are depicted as a function of N for $P_A = 10$ dBm and $P_{\text{BS}} = 30$ dBm. Obviously, increasing N hardly changes the power consumption of the passive RIS-aided systems, while further opens the power consumption gap between the F-HRM and active RIS-aided systems.

The results presented in Figure 7.8 are in accordance with the earlier studies [83, 85, 86] that an interesting trade-off exists between the achievable rate and power consumption. Therefore, the RIS-aided systems with partially or fully active reflecting elements are capable to achieve ultimate capacity gains compared to the conventional reflection-based transmission schemes such as fully passive RIS-aided systems. On the other hand, although the HRM and fully active RIS-aided systems have the same hardware capabilities, i.e., all reflecting elements are integrated with additional power amplifiers, since constantly driving active RIS elements requires a tremendous power consumption, more energy-efficient communication systems with high data rate can be constructed using HRM transmission concepts that limit the overall power consumption. In summary, it can be deduced from the results that the HRM scheme offers an intermediate solution between a fully passive and fully active RIS-aided transmission scheme, and achieves noticeable performance gains with a high data rate in a more energy-efficient manner.

7.4 Summary

In this chapter, we have introduced the novel scheme of HRM, which offers a promising solution for RIS-aided transmission systems that experience high path attenuation. In the proposed HRM scheme, the target RIS has been split into sub-groups through which the conventional IM technique has been applied to transmit information. While the active/passive combinations of the reflecting elements in those sub-groups have been determined according to incoming information bits, the phases have been optimally adjusted for achieving maximum SNR gains. Therefore, the RIS has been configured to perform amplification and reflection functions at the same time. Besides, the analytical BER performance and the achievable rate of the HRM scheme have been derived. Furthermore, comprehensive computer simulations have been conducted to illustrate the performance achievement of the HRM scheme over the existing fully active, fully passive and RM systems.

8. OVER-THE-AIR BEAMFORMING WITH RECONFIGURABLE INTELLIGENT SURFACES

In this chapter, unlike the conventional precoding techniques that employ power-hungry and hardware-complex devices [118], for RIS-aided multi-user downlink transmission systems, we propose a novel *over-the-air beamforming* technique with the aid of an active RIS to exploit its capability of manipulating the magnitude of the incident wave. In other words, the main motivation of the over-the-air beamforming scheme is to simplify the transmitter and receiver ends of the overall network while transferring inter-user interference elimination tasks completely to an active RIS. Therefore, this paper proposes two novel over-the-air beamforming schemes that mitigate the burden of signal processing on the transmitter and receiver sides. In the proposed over-the-air beamforming-based transmission scheme, it is assumed that a multi-antenna transmitter serves K single-antenna users through an active RIS without utilizing any other signal processing tasks at the transmitter and the receiver sides. Then, the reflection coefficients of the active RIS are properly adjusted to maximize the sum-rate of the overall system. Moreover, taking inspiration from this over-the-air beamforming concept, a new receive IM scheme that transmits additional information bits to specify the index of the effective received antenna is also proposed. Contrary to the traditional receive IM systems [119,120], in the proposed system, since no precoding is applied at the transmitter, the reflection coefficients of the active RIS are rectified to steer the incident signal into the intended receive antenna. On the other hand, since the receive IM scheme benefits from the multi-antenna transmission at the user side and IM system design at the receiver side, it shows the favourable features of both, such as high spectral efficiency and improved performance. In these proposed over-the-air downlink beamforming and over-the-air uplink receive IM schemes, to optimize reflection coefficients of the active RISs, two distinct semidefinite relaxation (SDR)-based optimization problems are formulated, which can be effectively solved through the CVX convex optimization toolbox [121]. Furthermore, the achievable rate

and BER performance of the proposed over-the-air beamforming-based transmission schemes are investigated through extensive computer simulations.

The rest of the chapter is organized as follows. In Section 8.1, after giving a short review of the conventional zero-forcing (ZF) precoding, we introduce the system model of the proposed over-the-air beamforming-based multi-user multi-antenna transmission scheme. In Section 8.2, the over-the-air beamforming-based receive IM scheme and its low-complexity receiver detection are introduced. Section 8.3 provides the sum-rate and BER results of the proposed over-the-air beamforming-based transmission systems, and the conclusions are drawn in Section 8.4.

8.1 Over-the-Air Beamforming with RIS

In this section, after a review of conventional transmit precoding, the over-the-air beamforming concept is introduced for MISO downlink transmission systems.

8.1.1 Conventional transmit precoding

Considering a typical multi-user downlink transmission system without an RIS, a base station (BS) transmitter (T) with T_x antennas is assumed to perform ZF precoding to alleviate interference between K single-antenna users [122]. Let $\mathbf{F} \in \mathbb{C}^{K \times T_x} = \sqrt{L_D}\bar{\mathbf{F}}$ represents the channel matrix of the direct links between the T and the users, where $\bar{\mathbf{F}} \in \mathbb{C}^{K \times T_x}$ is modeled as independent Rayleigh fading channel matrix with $\sim \mathcal{CN}(\mathbf{0}, \mathbf{I})$ and L_D is the corresponding path attenuation, which is calculated as $L_D = C_0 d_D^{-\beta_D}$, where C_0 is the reference path attenuation at a distance of 1 meter (m) and d_D is the distance between T and the users. Then, the received signal of the k-th user (U$_k$), for $k \in \{1, 2, \cdots, K\}$, becomes

$$y_k = \mathbf{f}_k \mathbf{w}_k^{\mathrm{H}} x_k + \sum_{i \neq k}^{K} \mathbf{f}_k \mathbf{w}_i^{\mathrm{H}} x_i + c_k \tag{8.1}$$

where x_k being an M-PSK signal to be transmitted over the k-th transmit antenna. Here, $\mathbf{f}_k \in \mathbb{C}^{1 \times T_x}$ is the k-th row of the channel matrix $\mathbf{F}$ corresponding to the channel vector between T-U$_k$, $\mathbf{w}_k \in \mathbb{C}^{1 \times T_x}$ is the precoding vector for U$_k$ and $c_k \sim \mathcal{CN}(0, \sigma_s^2)$ is the static noise at U$_k$. Therefore, the signal-to-interference-plus-noise-ratio (SINR)

at U_k can be calculated as

$$\gamma_k = \frac{\left\|\mathbf{f}_k \mathbf{w}_k^{\mathrm{H}}\right\|^2}{\sum_{i \neq k}^{K} \left\|\mathbf{f}_k \mathbf{w}_i^{\mathrm{H}}\right\|^2 + \sigma_s^2}. \tag{8.2}$$

Moreover, the overall transmit ZF precoding matrix, exploiting the perfect CSI, can be obtained as [122]

$$\mathbf{W} = \sqrt{\zeta}(\mathbf{F}^{\mathrm{H}}\mathbf{F})^{-1}\mathbf{F}^{\mathrm{H}}. \tag{8.3}$$

where $\mathbf{W} \in \mathbb{C}^{T_x \times K} = [\mathbf{w}_1^{\mathrm{H}}, \cdots, \mathbf{w}_K^{\mathrm{H}}]$ and ζ is a scaling constant to meet the total power constraint P_T, such that $\mathbb{E}\left\{\mathbf{W}\mathbf{W}^{\mathrm{H}}\right\} = P_T$.

8.1.2 System model of over-the-air beamforming with RIS

In this subsection, after a review of conventional transmit precoding, the over-the-air beamforming concept is introduced for MISO downlink transmission systems.

8.1.2.1 Active RIS

The principal drawback of RIS-aided communication systems is the inherent multiplicative path attenuation along the RIS-aided indirect link, which is hardly compensated by the RIS with passive reflecting elements [83, 85]. Therefore, to overcome this challenge, an RIS architecture with active reflecting elements that enable to configure both the magnitude and phase of the incident wave at the expense of additional power consumption, is recently proposed [83, 123]. Therefore, unlike the passive RISs, the active RISs reflect incident signals with amplification via employing additional power circuitry. Although the active reflecting elements have a similar capability of amplifying the incident signal as in the full-duplex amplify-and-forward (AF) relays, their hardware constructions are completely different from each other. While the AF relays embody a circuitry for amplification in their hardware constructions and they are also externally equipped with high power-consuming RF chains to transmit and receive signals [55], the active reflecting elements employ reflective-type power amplifiers to simultaneously rectify the magnitude and phase of the incident wave [83].

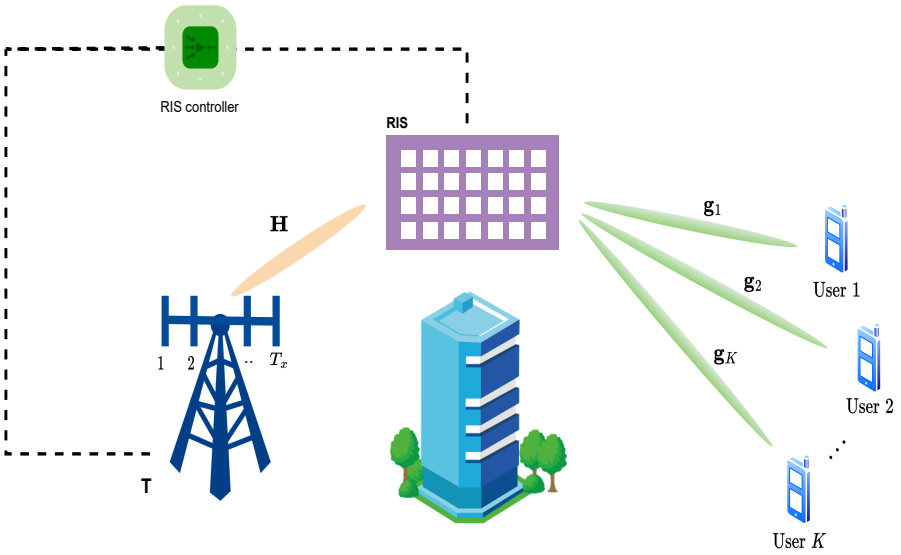

Figure 8.1 : Over-the-air beamforming-based multi-user downlink transmission system.

8.1.2.2 System model

An overwhelming literature on passive RIS-aided multi-user transmission deploys the RIS as a passive beamformer, after a preprocessing is conducted at the transmitter [55, 124]. However, in the proposed over-the-air beamforming concept, contrary to this traditional perspective, both the active and the passive beamforming are carried out only at the RIS with active reflecting elements.

As given in Fig. 8.1, in the proposed scheme, the direct transmission links between T with T_x antennas and K single-antenna users are neglected due to obstacles, thus, the communication is established through an active RIS with N reflecting elements. In the proposed over-the-air beamforming-based multi-user transmission, it is assumed that T and the users have the perfect CSI about T-RIS and RIS-users channels, which is conveyed to a smart RIS controller via a feedback control link [55]. Moreover, at the transmitter side, without requiring any additional signal processing approaches for interference mitigation, the overall signal is conveyed to the users through the RIS. Hence, unlike the traditional beamforming techniques that employ complex and power-hungry signal processing hardware [118, 125], the RIS is designed as a beamformer to alleviate multi-user interference by adjusting the amplitude and phase of each reflecting element. Towards this aim, the RIS elements are assumed to be equipped with additional power circuitry to modify both the magnitude and the

phase of the incident signal [12, 83, 86]. Furthermore, in the proposed system, since all transmit antennas simultaneously convey their own M-PSK modulated signals, a spectral efficiency of $\eta_{\text{MU}} = T_x \log_2(M)$ [bits/s/Hz] is achieved.

Let us assume that the channels between T-RIS are presented by the matrix $\mathbf{H} \in \mathbb{C}^{N \times T_x} = \sqrt{L_T}\bar{\mathbf{H}}$ and $\mathbf{g}_k \in \mathbf{C}^{1 \times N} = \sqrt{L_k}\bar{\mathbf{g}}_k$ represents the vector of channel coefficients between the RIS and U$_k$, where L_T and L_k correspond to path attenuation between T-RIS and RIS-U$_k$ links for $k \in \{1, 2, \cdots, K\}$, respectively. Here, for d_T and d_k being the corresponding distances, using a well-known distance-dependent model, the path attenuations are obtained as $L_T = C_0 d_T^{-\beta_T}$ and $L_k = C_0 d_k^{-\beta_k}$, where β_T and β_k are the path loss exponents at T-RIS and RIS-U$_k$, respectively. In the proposed system, the matrix $\bar{\mathbf{H}} \in \mathbb{C}^{N \times T_x}$ and the vector $\bar{\mathbf{g}}_k \in \mathbb{C}^{1 \times N}$ are both modeled as Rayleigh fading channels, whose each element is an independent and identically distributed (i.i.d.) Gaussian random variable with $\sim \mathcal{CN}(0, 1)$. In addition, the RIS architecture that is equipped with additional power circuitry to operate as an active RIS [83], is represented in a diagonal matrix $\mathbf{\Psi} \in \mathbb{C}^{N \times N} = \text{diag}\left\{\xi_1 e^{j\phi_1}, \xi_2 e^{j\phi_2}, \cdots, \xi_N e^{j\phi_N}\right\}$, where $\xi_n > 1$ and $\phi_n \in [-\pi, \pi]$ being the amplitude and phase of the n-th reflecting element for $n \in \{1, 2, \cdots, N\}$. Therefore, for the overall transmit signal being $\mathbf{x} \in \mathbb{C}^{T_x \times 1} = [x_1, x_2, \cdots, x_K]^T$, the received signal at U$_k$ is obtained as

$$y_k = \sqrt{P_k}\mathbf{g}_k \mathbf{\Psi} \mathbf{H} \mathbf{x} + \mathbf{g}_k \mathbf{\Psi} \mathbf{v}^{\text{T}} + n_k \tag{8.4}$$

where $\mathbb{E}\left\{\mathbf{x}^{\mathbf{H}}\mathbf{x}\right\} = 1$. Here, P_k is the power introduced by the k-th transmit antenna, the vector $\mathbf{v} \in \mathbb{C}^{1 \times N}$ represents the thermal noise generated from power amplifier circuits of active reflecting elements [83] and n_k is the static noise term at U$_k$, where $\mathbf{v} \sim \mathcal{CN}(\mathbf{0}, \mathbf{I}_N \sigma_v^2)$ and $n_k \sim \mathcal{CN}(0, \sigma_s^2)$ for σ_v^2 and σ_s^2 being the corresponding noise variances of dynamic and static noise figures, respectively. Moreover, at the user side, since the received superposed signal at U$_k$ (8.4) includes the targeted and interference signals, it can be rewritten as

$$y_k = \sqrt{P_k}\mathbf{g}_k \mathbf{\Psi} \mathbf{h}_k x_k + \sqrt{P_k} \sum_{i \neq k}^{K} \mathbf{g}_k \mathbf{\Psi} \mathbf{h}_i x_i + \mathbf{g}_k \mathbf{\Psi} \mathbf{v}^{\text{T}} + n_k \tag{8.5}$$

where $\mathbf{h}_k \in \mathbb{C}^{N \times 1}$ is the k-th column of the channel matrix $\mathbf{H}$ corresponding to the channel vector between the k-th transmit antenna and the RIS. At this point, the SINR

at U_k can be calculated as:

$$\gamma_k = \frac{P_k \left\|\mathbf{g}_k \mathbf{\Psi} \mathbf{h}_k\right\|^2}{P_k \sum_{i \neq k}^{K} \left\|\mathbf{g}_k \mathbf{\Psi} \mathbf{h}_i\right\|^2 + \left\|\mathbf{g}_k \mathbf{\Psi} \mathbf{v}^{\mathrm{T}}\right\|^2 + \sigma_s^2}. \tag{8.6}$$

Accordingly, the sum-rate of the overall system becomes:

$$R_c = \sum_{k=1}^{K} \log_2(1+\gamma_k). \tag{8.7}$$

Then, to maximize this sum-rate, the reflection coefficients of the active RIS elements are optimized. In what follows, the corresponding problem formulation and the proposed solution are presented.

8.1.3 Problem formulation and proposed solution

In the over-the-air beamforming-based multi-user transmission scheme, interference cancellation is performed at the RIS without employing any additional integrated high-cost signal processing circuitry, such as multiple RF chains, either at T or user sides. For this purpose, the reflection coefficients of the RIS are adjusted to maximize the SINR of the intended U_k. Therefore, to deal with this problem, the following QCQP problem is formulated

$$(\mathrm{P1}): \max_{\mathbf{\Psi}} \quad \gamma_k \tag{8.8}$$

$$\text{s.t.} \quad P_k \left\|\mathbf{g}_k \mathbf{\Psi} \mathbf{H}_k\right\|^2 \geq \Gamma_k \Big(P_k \sum_{i \neq k}^{K} \left\|\mathbf{g}_k \mathbf{\Psi} \mathbf{H}_i\right\|^2 + \left\|\mathbf{g}_k \mathbf{\Psi} \mathbf{v}^{\mathrm{T}}\right\|^2 + \sigma_s^2 \Big) \tag{8.9}$$

$$P_{\mathrm{BS}} \left\|\mathbf{\Psi} \mathbf{H}\right\|^2 + \left\|\mathbf{\Psi}\right\|^2 \sigma_s^2 \leq P_A \tag{8.10}$$

where Γ_k is the minimum SINR requirement of U_k, $P_{\mathrm{BS}} = K P_k$, and P_A is the maximum reflection power introduced by the active reflecting elements. Please note that for the over-the-air beamforming-based multi-user systems, the total power P_T is the sum of power dissipated at the transmitter (P_{BS}) and the RIS (P_A), that is $P_T = P_A + P_{\mathrm{BS}}$, while for the conventional transmission without RIS, P_T denotes to total power consumed at the transmitter.

Then, using the Cauchy-Schwarz inequality, the constraint in (8.10) can be rewritten as

$$\left\|\mathbf{\Psi}\right\|^2 \leq \frac{P_A}{P_{\mathrm{BS}} \left\|\mathbf{H}\right\|^2 + \sigma_s^2}. \tag{8.11}$$

Therefore, since the problem (P1) is non-convex and it is difficult to obtain an optimal solution, we resort to the SDR technique and define new variables $\mathbf{A}_k \in \mathbb{C}^{N\times N} = \mathbf{H}_k\mathbf{H}_k^{\mathrm{H}}$, $\mathbf{B}_k \in \mathbb{C}^{N\times N} = \mathbf{g_k}^{\mathrm{H}}\mathbf{g}_k$ and $\mathbf{V} = \mathbf{v}\mathbf{v}^{\mathbf{H}}$. In light of these, the SINR of the k-th user in (8.6) can be rewritten as

$$\gamma_k = \frac{P_k \mathrm{Tr}(\mathbf{Q}_k\mathbf{Z})}{\sum_{i\neq k} P_k \mathrm{Tr}(\mathbf{Q}_i\mathbf{Z}) + \mathrm{Tr}(\mathbf{Q}_m\mathbf{Z}) + \sigma_s^2} \geq \Gamma_k \tag{8.12}$$

where $\mathbf{Q}_k \in \mathbb{C}^{N\times N} = \mathbf{A}_k \circ \mathbf{B}_k$, $\mathbf{Q}_i \in \mathbb{C}^{N\times N} = \mathbf{A}_i \circ \mathbf{B}_k$ and $\mathbf{Q}_m \in \mathbb{C}^{N\times N} = \mathbf{V}_k \circ \mathbf{B}_k$, while $\mathbf{Z} \in \mathbb{C}^{N\times N} = \mathbf{z}\mathbf{z}^{\mathrm{H}}$ for $\mathbf{z} \in \mathbb{C}^{N\times 1}$ being a vector consisting the non-zero diagonal elements of the reflection matrix $\mathbf{\Psi}$, i.e., $\mathbf{z} = [\alpha_1 e^{j\phi_1}, \alpha_2 e^{j\phi_2}, \cdots, \alpha_N e^{j\phi_N}]^{\mathrm{H}}$ [50, 126]. Therefore, the maximization problem (P1) is equivalently defined as

$$(\mathrm{P2}): \max_{\mathbf{\Psi}} \quad \gamma_k \tag{8.13}$$

$$\text{s.t.} \quad P_k \mathrm{Tr}(\mathbf{Q}_k\mathbf{Z}) - \Gamma_k\big(\sum_{i\neq k} P_k \mathrm{Tr}(\mathbf{Q}_i\mathbf{Z}) + \mathrm{Tr}(\mathbf{Q}_m\mathbf{Z}) + \sigma_s^2\big) \geq 0 \tag{8.14}$$

$$\mathrm{Tr}(\mathbf{Z}) \leq \frac{P_A}{P_{\mathrm{BS}}\mathrm{Tr}(\mathbf{H}\mathbf{H}^{\mathrm{H}}) + \sigma_s^2}. \tag{8.15}$$

Here, $\mathbf{Z}$ is a positive semidefine matrix and $\mathrm{rank}(\mathbf{Z}) = 1$. However, since the rank-one constraint is non-convex, we remove this constraint and reformulate (P2) as a convex feasibility problem as follows

$$(\mathrm{P3}): \text{ Find } \mathbf{Z} \tag{8.16}$$

$$\text{s.t.} \quad P_k \mathrm{Tr}(\mathbf{Q}_k\mathbf{Z}) - \Gamma_k\big(\sum_{i\neq k}^{K} P_k \mathrm{Tr}(\mathbf{Q}_i\mathbf{Z}) + \mathrm{Tr}(\mathbf{Q}_m\mathbf{Z}) + \sigma_s^2\big) \geq 0 \tag{8.17}$$

$$\mathrm{Tr}(\mathbf{Z}) \leq \frac{P_A}{P_{\mathrm{BS}}\mathrm{Tr}(\mathbf{H}\mathbf{H}^{\mathrm{H}}) + \sigma_s^2}. \tag{8.18}$$

Finally, through the existing solvers of CVX toolbox [121], a feasible solution of (P3) satisfying the inequality constraints in (8.17) and (8.18) is obtained. However, after the relaxation, the optimal solution of (P3) cannot always ensure the rank-one solution. Therefore, for $\tilde{\mathbf{Z}}$ being the optimal solution of the problem (P3), using the eigenvalue decomposition of $\tilde{\mathbf{Z}} = \mathbf{U}\mathbf{\Sigma}\mathbf{U}^{\mathrm{H}}$, the estimated $\mathbf{z}$ is sub-optimally obtained as

$$\tilde{\mathbf{z}} = \mathbf{U}\mathbf{\Sigma}^{1/2}\mathbf{e}^{\mathrm{H}} \tag{8.19}$$

where $\mathbf{e} \in \mathbb{C}^{1\times N}$ is a Gaussian random vector with $\sim \mathcal{CN}(\mathbf{0}, \mathbf{I})$, where $\mathbf{U} \in \mathbb{C}^{N\times N}$ is a unitary matrix of eigenvectors and $\mathbf{\Sigma} \in \mathbb{C}^{N\times N}$ is a diagonal matrix of eigenvalues. Then, after determining optimized reflection matrix, the RIS performs over-the-air beamforming in order to alleviate the user interference.

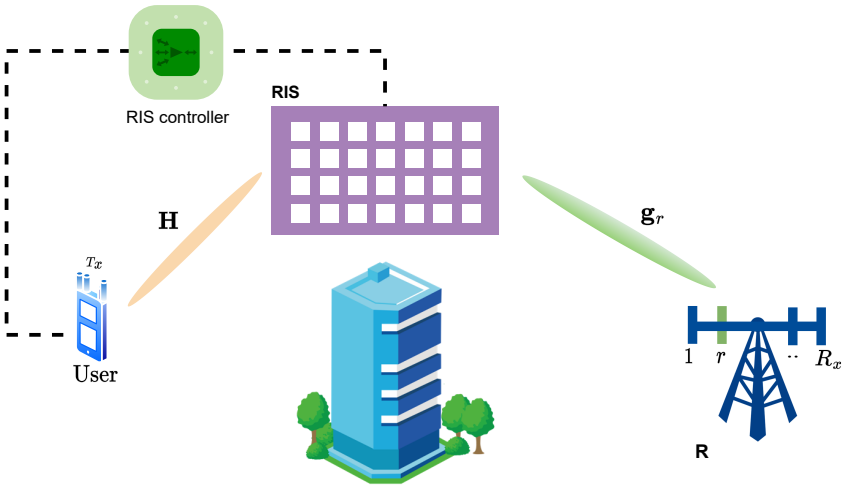

Figure 8.2 : Over-the-air receive IM scheme.

8.2 Over-the-Air Receive Index Modulation

In this section, the proposed over-the-air beamforming concept is adopted to a novel receive IM transmission scheme. Considering the over-the-air beamforming approach given in Section 8.1, a single-user uplink transmission of an active RIS-aided IM transmission system is developed.

8.2.1 System model of over-the-air receive IM

As given in Figure 8.2, in the proposed IM system, due to presence of the obstacles over the direct links, a multi-antenna user communicates with an R_x-antenna receiver (R) through an RIS with N reflecting elements. Besides, an RIS controller is attached to the RIS that exchanges the information through a feedback control link. In the proposed system, considering the IM transmission principle [72], an over-the-air receive IM scheme is developed. Unlike traditional receive IM schemes [119,120,127] that deploy transmit precoding techniques via high-cost hardware devices for preprocessing the transmit signal before its transmission, the proposed receive IM scheme employs the RIS as a signal processing unit and apply an over-the-air beamforming at the RIS. In the over-the-air receive IM scheme, at the user side, the conventional multi-antenna transmission is considered. Moreover, in order to attain higher data rates, extra information bits are conveyed via indicating the active receive antenna index. Therefore, the incoming information bits are used to determine the modulated M-PSK symbols for each of the available T_x transmit antennas, as well as to specify

the active receive antenna index, one out of R_x receive antennas. Therefore, the spectral efficiency achieved by this novel receive IM scheme is calculated as

$$\eta_{\text{IM}} = T_x \log_2(M) + \log_2(R_x) \qquad \text{[bits/s/Hz]}. \tag{8.20}$$

In this system, the information of the active receive antenna index and perfect channel knowledge of user-RIS and RIS-R links is shared by the user to the RIS through the smart controller. Then, the reflection coefficient of the RIS elements are adjusted to ensure that the target receive antenna has the strongest received signal power. In other words, by the means of active reflecting elements, the RIS acts as a kind of digital beamformer and steers the overall signal along the desired receive antenna direction.

Let the multi-path fading channels between user-RIS and RIS-R links are modeled as the independent Rayleigh fading channels, which are denoted by the channel matrices of $\mathbf{H} \in \mathbb{C}^{N \times T_x}$ and $\mathbf{G} \in \mathbb{C}^{R_x \times N} = [\mathbf{g}_1^{\mathrm{T}}, \mathbf{g}_2^{\mathrm{T}}, \cdots, \mathbf{g}_{R_x}^{\mathrm{T}}]^{\mathrm{T}}$, respectively, where $\mathbf{g}_r \in \mathbb{C}^{1 \times N}$ is the r-th row of the the channel matrix $\mathbf{G}$ corresponding to the channel vector between the RIS and the r-th receive antenna for $r \in \{1, 2, \cdots, R_x\}$. Therefore, for x_t being the M-PSK modulated signal transmitted from the t-th transmit antenna, the overall transmit signal becomes $\mathbf{x} \in \mathbb{C}^{T_x \times 1} = [x_1, \cdots, x_{T_x}]^{\mathrm{T}}$, where $\mathbb{E}\{\mathbf{x}^{\mathrm{H}}\mathbf{x}\} = 1$ and $t \in \{1, 2, \cdots, T_x\}$. Then, the received signal at the target receive antenna r is obtained as

$$y_r = \sqrt{P_{\text{BS}}}\mathbf{g}_r \mathbf{\Psi}_r \mathbf{H}\mathbf{x} + \mathbf{g}_r \mathbf{\Psi}_r \mathbf{v} + n_r \tag{8.21}$$

where $\mathbf{\Psi}_r \in \mathbb{C}^{N \times N}$ is the optimized diagonal reflection matrix for the corresponding r-th receive antenna. It is worth noting that according to incoming spatial bits, if the r-th receive antenna is activated, it is ensured that the signal power of the r-th received antenna is much stronger than the others:

$$\|\mathbf{g}_r \mathbf{\Psi}_r \mathbf{H}\|^2 \gg \sum_{i \neq r}^{R_x} \|\mathbf{g}_i \mathbf{\Psi}_r \mathbf{H}\|^2 . \tag{8.22}$$

Therefore, to address this problem, for $\mathbf{\Theta}_r = \text{diag}(\mathbf{g}_r)\mathbf{H}$ and $\mathbf{z} \in \mathbb{C}^{1 \times T_x} = \text{diag}(\mathbf{\Psi}_r)$, a QCQP optimization problem is formulated as

$$(\text{P4}): \max_{\mathbf{\Psi}} \ \mathbf{z}^{\mathrm{H}} \mathbf{\Theta}_r \mathbf{\Theta}_r^{\mathrm{H}} \mathbf{z} \tag{8.23}$$

$$\text{s.t.} \quad P_{\text{BS}} \|\mathbf{\Psi}_r \mathbf{H}\|^2 + \|\mathbf{\Psi}_r\|^2 \sigma_s^2 \leq P_A. \tag{8.24}$$

Then, resorting to SDR, the problem (P4) is expressed as

$$(\text{P5}): \max_{\mathbf{\Psi}} \ \text{Tr}(\mathbf{\Delta}_r \mathbf{Z}) \tag{8.25}$$

$$\text{s.t.} \quad \text{Tr}(\mathbf{\Delta}_r \mathbf{Z}) - \delta_r \sum_{i \neq r}^{R_x} \text{Tr}(\mathbf{\Delta}_i \mathbf{Z}) \geq 0 \tag{8.26}$$

$$\text{Tr}(\mathbf{Z}) \leq \frac{P_A}{P_{\text{BS}} \text{Tr}(\mathbf{H}\mathbf{H}^{\text{H}}) + \sigma_s^2}. \tag{8.27}$$

Here, for $\delta_r \gg 1$, $\mathbf{\Delta}_r \in \mathbb{C}^{N \times N} = \mathbf{\Theta}_r \mathbf{\Theta}_r^{\text{H}}$ and $\mathbf{Z} = \mathbf{z}\mathbf{z}^{\text{H}}$, the problem (P5) is solved using CVX solvers [121]. Then, following the same processes as in the multi-user downlink transmission in Section II, the sub-optimal estimate of $\mathbf{z}$, is obtained as given in (8.19). Then, the resulting RIS reflection matrix enables that the overall signal is oriented in the direction of the target receive antenna.

8.2.2 Low-complexity successive greedy detector

In the subsection that follows, a sub-optimal successive detection algorithm for the proposed receive IM scheme is proposed. In the proposed system, after the optimization of the reflection matrix $\mathbf{\Psi}_r$ for the specified r-th receive antenna, it is straightforward to exploit a ML detector that jointly estimates the "spatial symbol" r and the overall transmit signal vector $\mathbf{x}$ as follows

$$[\hat{r}, \hat{\mathbf{x}}] = \arg \min_{r, \mathbf{x}} \sum_{j=1}^{R_x} \left| y_j - \sqrt{P_{\text{BS}}} \mathbf{g}_j \mathbf{\Psi}_r \mathbf{H} \mathbf{x} \right|^2. \tag{8.28}$$

However, in the proposed receive IM scheme, in order to save the computational complexity, instead of considering joint detection, the receiver reconstructs the transmit information via a low-complexity greedy detector that perform the successive detection in the following way. First, using amplitude detectors, the index of the active receive antenna is detected as

$$\hat{r} = \arg \max_{j \in \{1, \cdots, R_x\}} |y_j| \,. \tag{8.29}$$

Then, exploiting the ML detector, the transmit signal vector $\mathbf{x}$ is estimated, by considering all possible $\mathbf{x}$ realizations, as follows

$$\hat{\mathbf{x}} = \arg \min_{\mathbf{x}} \left| y_{\hat{r}} - \sqrt{P_{\text{BS}}} \mathbf{g}_r \mathbf{\Psi}_r \mathbf{H} \mathbf{x} \right|^2. \tag{8.30}$$

Moreover, from the computational complexity standpoint, we note that since the complexity of SDR problem (P5) is $\mathcal{O}(N^{4.5})$ [128], the overall complexity of the greedy detector approximates to $\sim \mathcal{O}(M^{T_x} + T_x)$, while the complexity for the joint ML detector is $\sim \mathcal{O}((M^{T_x} + T_x + N^{4.5})R_x^2)$, which grows exponentially with increasing N and R_x. Therefore, comparing to the joint ML detection, the proposed greedy detector offers a significant reduction in computational burden.

However, in the proposed receive IM scheme, in order to save the computational complexity, instead of considering joint detection, the receiver reconstructs the transmit information via a low-complexity greedy detector that perform the successive detection in the following way. First, using amplitude detectors, the index of the active receive antenna is detected as

$$\hat{r} = \arg \max_{j \in \{1,\cdot,R_x\}} |y_j| . \tag{8.31}$$

Then, exploiting the maximum likelihood (ML) detector, the transmit signal vector $\mathbf{x}$ is estimated, by considering all possible $\mathbf{x}$ realizations, as follows

$$\hat{\mathbf{x}} = \arg \min_{\mathbf{x}} \left| y_{\hat{r}} - \sqrt{P_{\text{BS}}} \mathbf{g}_r \mathbf{\Psi}_r \mathbf{H} \mathbf{x} \right|^2 . \tag{8.32}$$

Moreover, from the computational complexity standpoint, we note that since the complexity of SDR problem (P5) is $\mathcal{O}(N^{4.5})$ [128], the overall complexity of the greedy detector approximates to $\sim \mathcal{O}(M^{T_x} + T_x)$, while the complexity for the joint ML detector is $\sim \mathcal{O}((M^{T_x} + T_x + N^{4.5})R_x^2)$, which grows exponentially with increasing N and R_x. Therefore, comparing to the joint ML detection, the proposed greedy detector offers a significant reduction in computational burden.

8.3 Numerical Results

In this section, the sum-rate and BER performance of the proposed over-the-air beamforming-based single-user and multi-user downlink transmission, and uplink receive IM schemes are presented through the Monte Carlo simulations. Moreover, comparing to the ZF-based conventional transmission [120, 122] and the state-of-the-art RIS-aided joint beamforming schemes [55], the improved performance of the over-the-air beamforming-based systems are illustrated.

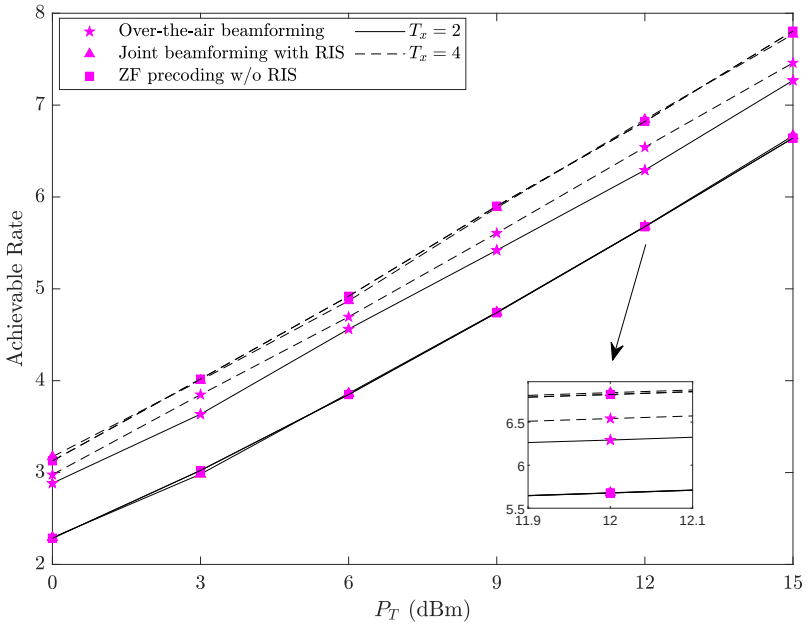

Figure 8.3 : Comparison of the achievable rate performance of the proposed over-the-air beamforming with traditional ZF precoding and joint beamforming with RIS for single-user system configurations.

In all computer simulations, the following system setups are considered: the reference path loss value is $C_0 = -30$ dBm, the noise variances are $\sigma_v^2 = \sigma_s^2 = -90$ dBm , the path loss exponents for the RIS-aided systems are $\beta_T = 2.2$ and $\beta_k = 2.8$ and for the conventional direct transmission, it is $\beta_D = 3.5$ [86], the distances are $d_T = 20$, $d_R = 30$ m and $d_D = 50$ m.

8.3.1 Downlink transmission

In this subsection, the numerical results of the proposed over-the-air beamforming and the benckmark schemes for single-user and multi-user downlink systems are demonstrated.

8.3.1.1 Single-user

The following computer simulation results are performed for single-user MISO transmission schemes.

In Figure 8.3, for a single-user downlink transmission ($K = 1$) with $T_x \in \{2, 4\}$ and $N = 16$, the achievable rate performance of the proposed over-the-air beamforming scheme as a function of total transmit power P_T is compared to the traditional ZF precoding [122] and the passive RIS-aided joint active and passive beamforming

techniques [55]. Here, while P_T is the overall power consumed at the transmitters of the traditional ZF precoding and joint beamforming transmission schemes, it corresponds to the total power dissipated between the transmitter (P_{BS}) and the RIS (P_A) for the proposed over-the-air transmission, where $P_T = P_{\text{BS}} + P_A$ for $P_{\text{BS}} = 0$ dBm. Moreover, as discussed in Section 8.1, the reference ZF precoding considers a traditional single-hop transmission without RIS that performs transmit precoding before the signal transmission [122]. On the other hand, in the joint active and passive beamforming scheme, a passive RIS-aided single-user transmission with the existence of direct links between the transmitter and the user, is considered, where the digital beamforming at the transmitter and analog beamforming at a passive RIS via phase shifters are jointly optimized to enhance the received SNR of the user [55]. For this purpose, similar to our proposed beamforming technique, a QCQP-based non-convex optimization problem is formulated and an SDR-based solution is performed via CVX solvers [55]. The results show that although a direct link between the transmitter and the user does not exist in the proposed active RIS-aided over-the-air beamforming scheme, a considerably better performance achievement is observed for $T_x = 2$ compared to the traditional ZF and joint beamforming with passive RIS-aided transmission schemes. Moreover, it is shown that increasing T_x results in enhancement of the achievable rate of all systems. However, in the proposed active RIS-aided over-the-air beamforming scheme, as given in (8.11), since the magnitude of reflection matrix $\mathbf{\Psi}$ is restricted with the magnitude of transmission matrix $\mathbf{H}$, i.e., increasing T_x, a slighter performance improvement is achieved compared to the benchmark schemes. Furthermore, since a small-scale passive RIS is considered, i.e. $N = 16$, an additional performance improvement due to the indirect RIS-aided link is hardly observed in the passive RIS-aided joint beamforming scheme compared to the conventional ZF precoding scheme.

8.3.1.2 Multi-user downlink transmission

In this subsection, the sum-rate results of an active RIS-aided multi-user downlink system with the proposed over-the-air-beamforming is demonstrated.

In Figure 8.4, the sum rate of the downlink multi-antenna transmission scheme based on the conventional transmit ZF precoding [122] and the novel over-the-air

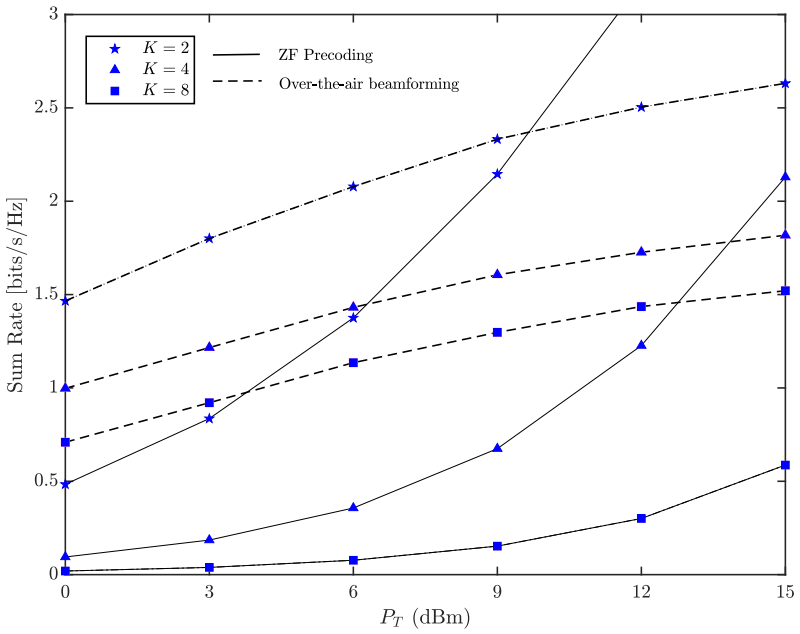

Figure 8.4 : Sum-rate comparison of the proposed over-the-air beamforming and the classical transmit ZF precoding for $K \in \{2, 4, 8\}$.

beamforming has been carried out for $K \in \{2, 4, 8\}$ and quadrature PSK (QPSK), i.e., $M = 4$. Here, for the over-the-air beamforming with $N = 16$, the transmitter power is assumed to be $P_{\text{BS}} = 0$ dBm, while, for a fair comparison, the transmit power of the conventional ZF precoder is equated to the total power P_T, where $P_T = P_{\text{BS}} + P_A$ for the RIS-aided system. Comparing these two schemes, it is obvious that at lower P_T values, the over-the-air beamforming based multi-user transmission scheme attains higher sum-rate than the classical transmit ZF precoding technique [122]. However, for $K = 2$ and $K = 4$, as P_T increases, the performance of ZF gradually begins to exceed the performance of the proposed beamforming scheme. Nevertheless, for $K = 4$, the ZF precoder achieves only a slight gain over the proposed beamforming concept at $P_T = 15$ dBm. It can be also deduced from Figure 8.4 that an increase in the total number of users rapidly decreases ZF sum-rate, however, such a severe performance loss is not observed in the proposed over-the-air beamforming-based system. Moreover, when the number of users further increases to $K = 8$, it is observed that the system with the proposed over-the-air beamforming-based scheme outperforms the system with the traditional ZF technique with a significant performance gain.

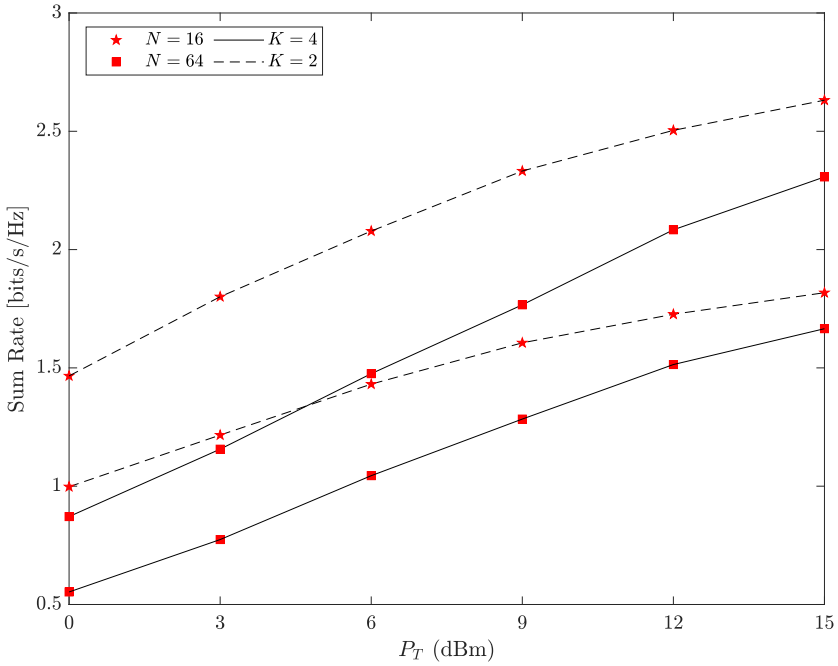

Figure 8.5 : Sum-rate performance of the proposed over-the-air beamforming-based multi-user systems for different system configurations.

In Figure 8.5, the sum-rate of the proposed over-the-air beamforming-based downlink multi-user system is evaluated for different system configurations. In this case, for a constant P_T, the performance of the over-the-air beamforming based systems are investigated for different number of the reflecting elements N, $P_{\text{BS}} = 0$ dBm and QPSK signaling. It is observed that increasing RIS size has an adverse affect on the system performance. This results may be explained by the fact that in the over-the-air beamforming design, as given in (8.11), the power consumed by the reflecting elements is inversely proportional with the magnitude of the channel matrix $\mathbf{H}$. Therefore, when a constant P_A is considered for $N = 16$ and $N = 64$, it reveals that the proposed beamforming-based systems with the lower N values show considerably better performance than the ones with the higher N values.

In Figure 8.6, the effect of increasing reflection power P_A on the sum-rate of the proposed beamforming based systems with QPSK and $P_T = 30$ dBm is investigated for $N = 16$. The results show that in all cases, the increasing P_A improves the system performance up to a certain P_A value, after which the performance begins to degrade. These results indicates the relation between the reflection power constraint P_A and transmitter power P_{BS} in (8.10). Indeed, in our system design, the overall

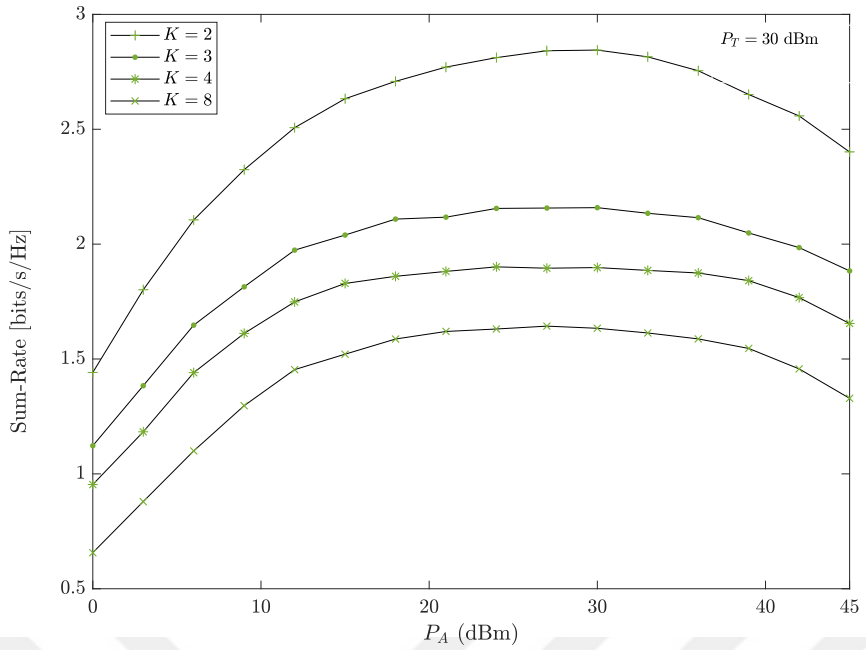

Figure 8.6 : Sum-rate of the proposed over-the-air beamforming-based systems for $N = 16$ and $K \in \{2, 3, 4, 8\}$.

consumed power P_T is dissipated to the transmitter (P_{BS}) and the RIS (P_A), where $P_T = P_{\text{BS}} + P_A$, and for a constant $P_T = 30$ dBm, P_{BS} decreases with increasing P_A. However, it is clear from (8.6) that the minimizing P_{BS} directly affects the SINR value. Surely, the investigation of this interesting trade-off points out the importance of the power allocation between the transmitter and the RIS, which is an open problem to be addressed in future studies.

8.3.2 Single-user uplink transmission

In this subsection, the BER performance of the proposed receive IM scheme is evaluated.

In Figure 8.7, the BER performance of the proposed receive IM scheme with sub-optimal greedy detector is investigated for different RIS-aided MIMO configurations with $N = 16$ and binary PSK (BPSK). Similar to the conventional receive IM schemes [120, 129], the performance results of the corresponding high-rate systems that employ (a) $T_x = 2$ and (b) $T_x = 4$ transmit antennas reveal a certain trade-off between system performance and data-rate.

In Figure 8.8, the BER performance of the transmit ZF precoded receive spatial modulation (RSM) [120] and the proposed over-the-air receive IM schemes are

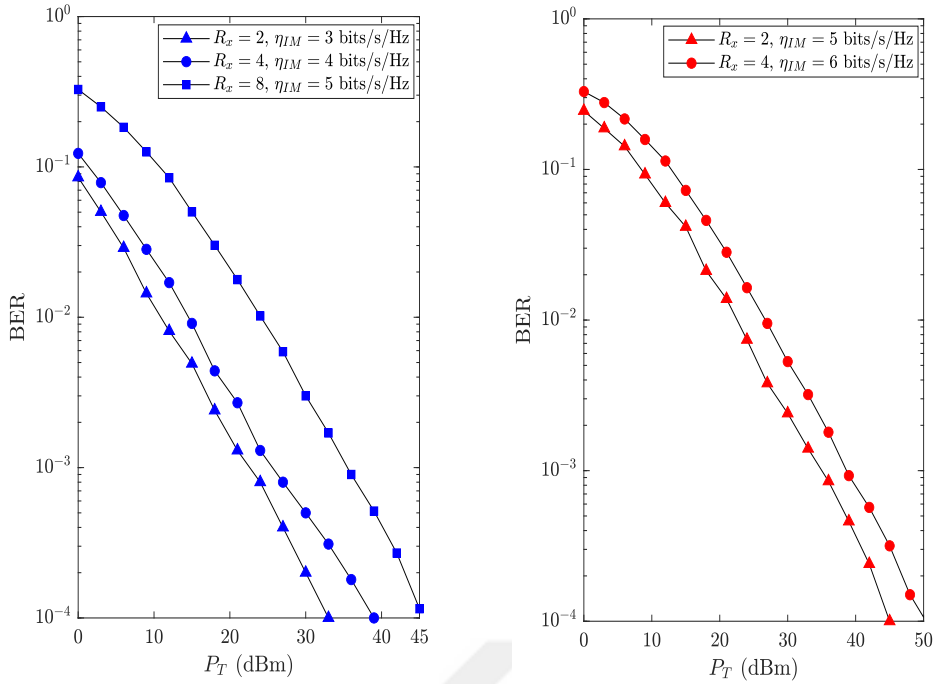

(a) (b)

Figure 8.7 : BER performance of the novel receive IM scheme with greedy detector for $N = 16$ and (a) $T_x = 2$, (b) $T_x = 4$.

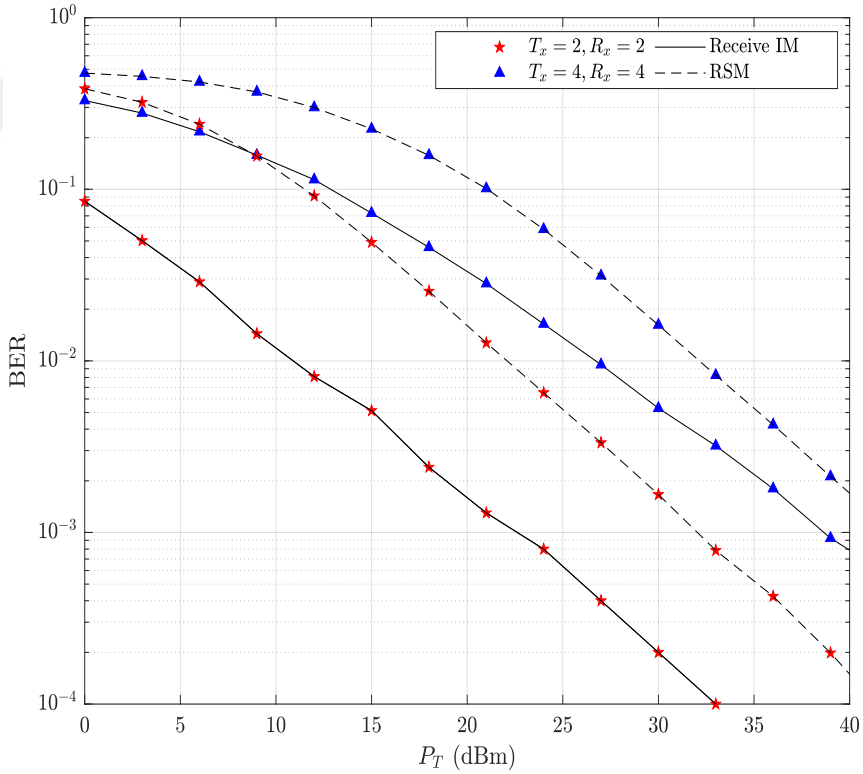

Figure 8.8 : BER performance comparison of the proposed receive IM and RSM schemes.

compared. For $R_x = T_x = 2$, the receive IM and the RSM schemes respectively exploit BPSK and QPSK modulations to achieve $\eta_{\text{IM}} = 3$ bits/s/Hz. On the other hand, for $R_x = T_x = 4$ configuration, the receive IM with BPSK and the RSM with 16-PSK assess $\eta_{\text{IM}} = 6$ bits/s/Hz. The results demonstrate the significant performance improvement of the proposed receive IM scheme over the traditional ZF precoded RSM [120].

8.4 Summary

In this chapter, first, deploying an active RIS, a novel beamforming approach has been proposed for RIS-aided multi-user systems. In the proposed concept, without employing any other signal processing units at the transmitter and/or receiver sides, the reflection coefficients of the active RIS have been customized to mitigate the user interference. To meet this challenge, we have obtained SDR-based solutions via CVX software toolbox. Moreover, taking the proposed over-the-air beamforming concept one step further, a low-complexity receive IM scheme has been developed for single-user uplink transmission. Through computer simulations, the enhanced performance of the over-the-air beamforming-based systems over the traditional precoding-based systems have been indicated.

9. CONCLUSIONS

IM-based systems with their simplified transceiver designs have a substantial potential to address the demanding high data-rate and high energy efficiency requirements of future networks. Hence, in light of the recent development in wireless technology and the growing IM literature, we have presented new IM-based physical layer solutions for today's and next generation networks.

As the first study in this thesis, we have implemented the classical MBM system in realistic indoor and outdoor IMT-Advanced channel conditions exploiting the statistics of a real RA with four radiation patterns. Then, we have extended the considered IMT-Advanced channel model, when a passive RIS is allocated between the transmitter and the receiver. Moreover, through Monte Carlo simulations, we have extensively investigated the channel capacity of the proposed scheme for different MIMO and RIS configurations.

In the subsequent two studies, utilizing its inherent capacity achieving feature of MBM, to provide transmit diversity gains, we have introduced two distinct STBC-based MBM schemes that are integrated with the traditional STBC technique of the Hurwitz-Radon family of matrices and a new circular matrix-based STBC design, respectively. In both studies, the various orders of transmit diversity gains have been attained via exploiting single RF chains at the transmitters. Furthermore, the improved performance of the systems have been compared with the reference contemporary studies.

Recently, with the emerging of the RIS technology, hardware construction designs of the next generation networks have gained promising new perspectives. In that sense, in the next studies, we have considered RIS-aided transmission schemes, and explored the new RIS-aided IM solutions. Towards this aim, we have introduced a cosine similarity-based low-complexity algorithm to optimize the reflection phases of the corresponding passive RIS elements to maximize composite channel gains of the RIS-aided MIMO transmission schemes. Moreover, we have extended our analysis, and developed a new RIS-aided IM scheme that leverages the introduced

low-complexity algorithm to optimize the reflection phases. Therefore, a challenging paradigm that has attempted to be solved via computationally complex optimization methods in the existing literature has been addressed in a more efficient manner.

More recent studies have highlighted that in passive RIS-aided systems, the contribution of the passive RIS is almost negligible, if a strong direct link exists between transmitter and receiver. Therefore, to achieve substantial performance gains, active RIS-aided transmission schemes have been recently introduced. In the next study of this thesis, considering the RM approaches, which are recently developed IM designs that leverage RIS itself for transmitting information, we have developed a novel RM scheme utilizing both active and passive reflecting elements at RIS to further improve performance gains. In this system, an unmodulated carrier has been exploited at the transmitter and the overall information bits have been embedded into the indices of the RIS sub-groups which are able to be altered to act as active or passive reflecting elements. Through this study, we have performed extensive computer simulations to indicate the performance improvement of the proposed system over the existing RM systems. Moreover, we have provided exhaustive analyses to investigate its theoretical ABEP, capacity and energy efficiency performances.

As the last study of this thesis, a novel over-the-air beamforming concept, which burdens an active RIS with eliminating inter-user interference tasks of a multiuser downlink transmission scheme, has been proposed. In the proposed scheme, the reflection coefficients of the active RIS are optimized to maximize sum-rate gains. Towards this aim, an SDP-based convex feasibility optimization problem is formulated, which has been solved through the CVX convex optimization toolbox. Moreover, to exhibit its reliability, we have compared the sum-rate performance of the proposed beamforming concept with the traditional ZF transmit beamforming method through extensive computer simulations. Inspired form this over-the-air beamforming concept, we have also proposed a novel single-user receive IM scheme that conveys additional information by indicating the index of the specified received antenna of a multi-antenna receiver in each time instant. However, in this case, the over-the-air beamforming at the RIS operates to steer the overall reflected signal in the direction of the effective received antenna. Further, the improved BER performance

of the proposed scheme over the classical receive IM systems has been exhibited via computer simulations.

As a result, this thesis has presented novel IM solutions for future generation networks in a broad range of application areas. Each chapter has investigated a different problem and offerred an effective solution. Moreover, each of proposed solution has been published in an international journal or an international conference proceeding.

REFERENCES

[1] **Series, M.** (2017). Guidelines for evaluation of radio interface technologies for IMT-2020, Report ITU-R M.2412-0.

[2] **Basar, E.** (2016). Index modulation techniques for 5G wireless networks, *IEEE Commun. Mag.*, *54*(7).

[3] **Mesleh, R.**, **Haas, H.**, **Sinanovic, S.**, **Ahn, C.W. and Yun, S.** (2008). Spatial modulation, *IEEE Trans. Veh. Technol.*, *57*(4), 22–28.

[4] **Mesleh, R.**, **Ikki, S.S. and Aggoune, H.M.** (2015). Quadrature spatial modulation, *IEEE Trans. Veh. Technol.*, *64*(6), 2738–2742.

[5] **Khandani, A.K.** (2013). Media-based modulation: A new approach to wireless transmission, *IEEE Int. Symp. Inf. Theory*, pp.3050–3054.

[6] **Sugiura, S.**, **Chen, S. and Hanzo, L.** (2010). Space-time shift keying: A unified MIMO architecture, *Proc. IEEE Global Telecommun. Conf. (GLOBECOM)*, pp.1–5.

[7] **Di Renzo, M.**, **Zappone, A.**, **Debbah, M.**, **Alouini, M.S.**, **Yuen, C.**, **De Rosny, J. and Tretyakov, S.** (2020). Smart radio environments empowered by reconfigurable intelligent surfaces: How it works, state of research, and the road ahead, *IEEE J. Sel. Areas Commun.*, *38*(11), 2450–2525.

[8] **Yigit, Z.**, **Basar, E. and Altunbas, I.** (2021). SimMBM channel simulator for media-based modulation systems, *2021 IEEE 32nd Annual Inter. Symp. Pers. Indoor and Mobile Radio Commun. (PIMRC)*, pp.531–536.

[9] **Yigit, Z. and Basar, E.** (2019). Space-time media-based modulation, *IEEE Trans. Signal Process.*, *67*(9), 2389–2398.

[10] **Yigit, Z.**, **Basar, E. and Altunbas, I.** (2019). Circular space-time block code design for ultra-reliable index modulation schemes, *IEEE 30th Annual Inter. Symp. Pers. Indoor and Mobile Radio Commun. (PIMRC)*, pp.1–6.

[11] **Yigit, Z. and Basar, E.** (2016). Low-complexity detection of quadrature spatial modulation, *Electron. Lett.*, *52*(20), 1729–1731.

[12] **Yigit, Z.**, **Basar, E.**, **Wen, M. and Altunbas, I.** (Nov. 2022). Hybrid reflection modulation, *IEEE Trans. Wireless Comm. (to appear)*.

[13] **Yigit, Z.**, **Basar, E. and Altunbas, I.** (2022). Over-the-air beamforming with reconfigurable intelligent surfaces, *Frontiers in Communications and Networks (to appear)*.

[14] **Foschini, G.J.** (1996). Layered space-time architecture for wireless communication in a fading environment when using multi-element antennas, *Bell Lab. Tech. J.*, *1*(2), 41–59.

[15] **Basar, E.**, **Wen, M.**, **Mesleh, R.**, **Di Renzo, M.**, **Xiao, Y. and Haas, H.** (2017). Index modulation techniques for next-generation wireless networks, *IEEE Access*, *5*, 16693–16746.

[16] **Jeganathan, J.**, **Ghrayeb, A.**, **Szczecinski, L. and Ceron, A.** (2009). Space shift keying modulation for MIMO channels, *IEEE Trans. Wireless Commun.*, *8*(7), 3692–3703.

[17] **Younis, A.**, **Serafimovski, N.**, **Mesleh, R. and Haas, H.** (2010). Generalised spatial modulation, *Proc. IEEE Forty Fourth ASILOMAR Conf. Signals, Systems and Computers*, pp.1498–1502.

[18] **Wang, J.**, **Jia, S. and Song, J.** (2012). Generalised spatial modulation system with multiple active transmit antennas and low complexity detection scheme, *IEEE Trans. Wireless Commun.*, *11*(4), 1605–1615.

[19] **Başar, E.**, **Aygölü, Ü.**, **Panayırcı, E. and Poor, H.V.** (2013). Orthogonal frequency division multiplexing with index modulation, *IEEE Trans. Signal Process.*, *61*(22), 5536–5549.

[20] **Basar, E.** (2016). On multiple-input multiple-output OFDM with index modulation for next generation wireless networks, *IEEE Trans. Signal Process.*, *64*(15).

[21] **Kaddoum, G.**, **Ahmed, M.F. and Nijsure, Y.** (2015). Code index modulation: A high data rate and energy efficient communication system, *IEEE Commun. Lett.*, *19*(2), 175–178.

[22] **Mesleh, R.**, **Elgala, H. and Haas, H.** (2011). Optical spatial modulation, *IEEE/OSA J. Optical Commun. and Netw.*, *3*(3), 234–244.

[23] **Yesilkaya, A.**, **Basar, E.**, **Miramirkhani, F.**, **Panayirci, E.**, **Uysal, M. and Haas, H.** (2017). Optical MIMO-OFDM with generalized LED index modulation, *IEEE Trans. Commun.*, *65*(8), 3429–3441.

[24] **Liu, P.**, **Di Renzo, M. and Springer, A.** (2016). Line-of-sight spatial modulation for indoor mmWave communication at 60 GHz, *IEEE Trans. Wireless Commun.*, *15*(11), 7373–7389.

[25] **Li, Q.**, **Wen, M.**, **Basar, E. and Chen, F.** (2018). Index modulated OFDM spread spectrum, *IEEE Trans. Wireless Commun.*, *17*(4), 2360–2374.

[26] **Başar, E. and Panayırcı, E.** (2015). Optical OFDM with index modulation for visible light communications, *2015 4th Inter. Workshop Optical Wireless Commun. (IWOW)*, pp.11–15.

[27] **Khandani, A.K.** (2014). Media-based modulation: Converting static Rayleigh fading to AWGN, *IEEE Int. Symp. Inf. Theory*, pp.1549–1553.

[28] **Basar, E. and Altunbas, I.** (2017). Space-time channel modulation, *IEEE Trans. Veh. Technol.*, *66*(8), 7609–7614.

[29] **Shamasundar, B.**, **Jacob, S.**, **Theagarajan, L.N. and Chockalingam, A.** (2018). Media-based modulation for the uplink in massive MIMO systems, *IEEE Trans. Veh. Technol.*, *67*(9), 8169 – 8183.

[30] **Naresh, Y. and Chockalingam, A.** (2017). On media-based modulation using RF mirrors, *IEEE Trans. Veh. Technol.*, *66*(6), 4967–4983.

[31] **Yildirim, I.**, **Basar, E. and Altunbas, I.** (2017). Quadrature channel modulation, *IEEE Wireless Commun. Lett.*, *6*(6), 790–793.

[32] **Pillay, N. and Xu, H.** (2018). Uncoded space-time labeling diversity—Application of media-based modulation with RF mirrors, *IEEE Commun. Lett.*, *22*(2), 272–275.

[33] **Alamouti, S.M.** (1998). A simple transmit diversity technique for wireless communications, *IEEE J. Sel. Areas Commun.*, *16*(8), 1451–1458.

[34] **Pillay, N. and Xu, H.** (2017). Uncoded space-time labeling diversity—Application of media-based modulation with RF mirrors, *IEEE Commun. Lett.*, *22*(2), 272–275.

[35] **Yüzgeçcioğlu, M. and Jorswieck, E.** (2017). Performance of media-based modulation in multi-user networks, *Proc. the Int. Symp. Wireless Commun. Systems*.

[36] **Shamasundar, B. and Chockalingam, A.** (2017). Multiuser media-based modulation for massive MIMO systems, *Proc. Signal Process. Advances in Wireless Commun. (SPAWC), IEEE 18th Int. Workshop*, pp.1–5.

[37] **Zhang, L.**, **Zhao, M. and Li, L.** (2018). Low-complexity multi-user detection for MBM in uplink large-scale MIMO systems, *IEEE Commun. Lett.*, *22*, 1568 – 1571.

[38] **Naresh, Y. and Chockalingam, A.** (2017). A low-complexity maximum-likelihood detector for differential media-based modulation, *IEEE Commun. Lett.*, *21*(10), 2158–2161.

[39] **Jacob, S.**, **Chockalingam, A.** *et al.*. Detection of generalized media-based modulation signals using multi-layered message passing, *Proc. 2018 IEEE 87th Veh. Technol. Conf.(VTC Spring)*, pp.1–5.

[40] **Naresh, Y. and Chockalingam, A.** (2018). Performance analysis of media-based modulation with imperfect channel state information, *IEEE Trans. Veh. Technol.*, *67*, 4192 – 4207.

[41] **Naresh, Y. and Chockalingam, A.** (2017). Full-duplex media-based modulation, *Proc. IEEE Globecom Workshops (GC Wkshps)*, pp.1–6.

[42] **Yildirim, I.**, **Basar, E. and Kurt, G.** (2018). Media-based modulation for secrecy communications, *IET Electron. Lett.*, *54*, 789–791.

[43] **Zhang, L. and Zhao, M.** (2018). Secrecy enhancement for media-based modulation via probabilistic optimization, *IEEE Commun. Lett.*, *23*(7), 1149–1152.

[44] **Seifi, E.**, **Atamanesh, M. and Khandani, A.K.** (2015). Media-based MIMO: A new frontier in wireless communications, *arXiv preprint arXiv:1507.07516*.

[45] **Tang, W.**, **Dai, J.Y.**, **Chen, M.**, **Li, X.**, **Cheng, Q.**, **Jin, S.**, **Wong, K.K. and Cui, T.J.** (2019). Programmable metasurface-based RF chain-free 8PSK wireless transmitter, *Electronics Letters*, *55*(7), 417–420.

[46] **Huang, C.**, **Zappone, A.**, **Alexandropoulos, G.C.**, **Debbah, M. and Yuen, C.** (2019). Reconfigurable intelligent surfaces for energy efficiency in wireless communication, *IEEE Trans. Wireless Commun.*, *18*(8), 4157–4170.

[47] **Yang, Z.**, **Chen, M.**, **Saad, W.**, **Xu, W.**, **Shikh-Bahaei, M.**, **Poor, H.V. and Cui, S.** (2022). Energy-efficient wireless communications with distributed reconfigurable intelligent surfaces, *IEEE Trans. Wireless Commun.*, *21*(1), 665–679.

[48] **Björnson, E.**, **Özdogan, Ö. and Larsson, E.G.** (2019). Intelligent reflecting surface versus decode-and-forward: How large surfaces are needed to beat relaying?, *IEEE Wireless Commun. Lett.*, *9*(2), 244–248.

[49] **Liu, R.**, **Li, H.**, **Li, M. and Liu, Q.** (2019). Symbol-level precoding design for intelligent reflecting surface assisted multi-user MIMO systems, *Proc. IEEE 11th Int. Conf. Wireless Commun. Signal Process. (WCSP)*, Xi'an, China, pp.1–6.

[50] **Ye, J.**, **Guo, S. and Alouini, M.S.** (2020). Joint reflecting and precoding designs for SER minimization in reconfigurable intelligent surfaces assisted MIMO systems, *IEEE Trans. Wireless Commun.*, *19*(8), 5561–5574.

[51] **Ferreira, R.C.**, **Facina, M.S.**, **De Figueiredo, F.A.**, **Fraidenraich, G. and De Lima, E.R.** (2020). Bit error probability for large intelligent surfaces under double-Nakagami fading channels, *IEEE Open J. Commun. Soc.*, *1*, 750–759.

[52] **Jung, M.**, **Saad, W.**, **Jang, Y.**, **Kong, G. and Choi, S.** (2020). Performance analysis of large intelligent surfaces (LISs): Asymptotic data rate and channel hardening effects, *IEEE Trans. Wireless Commun.*, *19*(3), 2052–2065.

[53] **Zhang, S. and Zhang, R.** (2020). Capacity characterization for intelligent reflecting surface aided MIMO communication, *IEEE J. Sel. Areas Commun.*, *38*(8), 1823–1838.

[54] **Di, B.**, **Zhang, H.**, **Song, L.**, **Li, Y.**, **Han, Z. and Poor, H.V.** (2020). Hybrid beamforming for reconfigurable intelligent surface based multi-user communications: Achievable rates with limited discrete phase shifts, *IEEE J. Sel. Areas Commun.*, *38*(8), 1809–1822.

[55] **Wu, Q. and Zhang, R.** (2019). Intelligent reflecting surface enhanced wireless network via joint active and passive beamforming, *IEEE Trans. Wireless Commun.*, *18*(11), 5394–5409.

[56] **Cui, M.**, **Zhang, G. and Zhang, R.** (2019). Secure wireless communication via intelligent reflecting surface, *IEEE Wireless Commun. Lett.*, *8*(5), 1410–1414.

[57] **Hong, S.**, **Pan, C.**, **Ren, H.**, **Wang, K. and Nallanathan, A.** (2020). Artificial-noise-aided secure MIMO wireless communications via intelligent reflecting surface, *IEEE Trans. Commun.*, *68*(12), 7851–7866.

[58] **Chen, J.**, **Liang, Y.C.**, **Pei, Y. and Guo, H.** (2019). Intelligent reflecting surface: A programmable wireless environment for physical layer security, *IEEE Access*, *7*, 82599–82612.

[59] **Taha, A.**, **Alrabeiah, M. and Alkhateeb, A.** (2019). Deep learning for large intelligent surfaces in millimeter wave and massive MIMO systems, *Proc. IEEE Global Commun. Conf. (GLOBECOM)*, Waikoloa, HI, USA, pp.1–6.

[60] **Huang, C.**, **Mo, R. and Yuen, C.** (2020). Reconfigurable intelligent surface assisted multiuser MISO systems exploiting deep reinforcement learning, *IEEE J. Sel. Areas Commun.*, *38*(8), 1839–1850.

[61] **Huang, C.**, **Alexandropoulos, G.C.**, **Yuen, C. and Debbah, M.** (2019). Indoor signal focusing with deep learning designed reconfigurable intelligent surfaces, *Proc. IEEE 20th Int. Workshop Signal Process. Advances Wireless Commun. (SPAWC)*, Cannes, France, pp.1–5.

[62] **Basar, E.**, **Yildirim, I. and Kilinc, F.** (2021). Indoor and outdoor physical channel modeling and efficient positioning for reconfigurable intelligent surfaces in mmWave bands, *IEEE Trans. Commun.*, *69*(12).

[63] **Basar, E. and Yildirim, I.** (2021). Reconfigurable intelligent surfaces for future wireless networks: A channel modeling perspective, *IEEE Wireless Commun.*, *28*(3), 108 – 114.

[64] **Ellingson, S.W.** (2021). Path loss in reconfigurable intelligent surface-enabled channels, *Proc. IEEE 32nd Int. Symp. Pers. Indoor and Mobile Radio Commun. (PIMRC)*, Helsinki, Finland, pp.1–6.

[65] **Tang, W.**, **Chen, M.Z.**, **Chen, X.**, **Dai, J.Y.**, **Han, Y.**, **Di Renzo, M.**, **Zeng, Y.**, **Jin, S.**, **Cheng, Q. and Cui, T.J.** (2020). Wireless communications with reconfigurable intelligent surface: Path loss modeling and experimental measurement, *IEEE Trans. Wireless Commun.*, *20*(1), 421–439.

[66] **Basar, E.**, **Yildirim, I. and Kilinc, F.** (2021). Indoor and outdoor physical channel modeling and efficient positioning for reconfigurable intelligent surfaces in mmWave bands, *IEEE Transactions on Communications*, *69*(12), 8600–8611.

[67] **Basar, E. and Yildirim, I.** (2020). SimRIS channel simulator for reconfigurable intelligent surface-empowered communication systems, *2020 IEEE Latin-American Conf. Commun. (LATINCOM)*, pp.1–6.

[68] **Abeywickrama, S.**, **Zhang, R.**, **Wu, Q. and Yuen, C.** (2020). Intelligent reflecting surface: Practical phase shift model and beamforming optimization, *IEEE Trans. Commun.*

[69] **Dai, L.**, **Wang, B.**, **Wang, M.**, **Yang, X.**, **Tan, J.**, **Bi, S.**, **Xu, S.**, **Yang, F.**, **Chen, Z.**, **Di Renzo, M.** *et al.* (2020). Reconfigurable intelligent surface-based wireless communications: Antenna design, prototyping, and experimental results, *IEEE Access*, *8*, 45913–45923.

[70] **Trichopoulos, G.C.**, **Theofanopoulos, P.**, **Kashyap, B.**, **Shekhawat, A.**, **Modi, A.**, **Osman, T.**, **Kumar, S.**, **Sengar, A.**, **Chang, A. and Alkhateeb, A.** (2022). Design and evaluation of reconfigurable intelligent surfaces in real-world environment, *IEEE Open J. Commun. Soc.*, *3*, 462–474.

[71] **Fara, R.**, **Ratajczak, P.**, **Huy, D.T.P.**, **Ourir, A.**, **Di Renzo, M. and De Rosny, J.** (2022). A prototype of reconfigurable intelligent surface with continuous control of the reflection phase, *IEEE Wireless Commun.*, *29*(1), 70–77.

[72] **Basar, E.** (2020). Reconfigurable intelligent surface-based index modulation: A new beyond MIMO paradigm for 6G, *IEEE Trans. Commun.*, *68*(5), 3187–3196.

[73] **Canbilen, A.E.**, **Basar, E. and Ikki, S.S.** (2020). Reconfigurable intelligent surface-assisted space shift keying, *IEEE Wireless Commun. Lett.*, *9*(9), 1495–1499.

[74] **Ma, T.**, **Xiao, Y.**, **Lei, X.**, **Yang, P.**, **Lei, X. and Dobre, O.A.** (2020). Large intelligent surface assisted wireless communications with spatial modulation and antenna selection, *IEEE J. Sel. Areas Commun.*, *38*(11), 2562–2574.

[75] **Li, Q.**, **Wen, M.**, **Wang, S.**, **Alexandropoulos, G.C. and Wu, Y.C.** (2021). Space shift keying with reconfigurable intelligent surfaces: Phase configuration designs and performance analysis, *IEEE Open J. Commun. Soc.*, *2*, 322–333.

[76] **Singh, U.**, **Bhatnagar, M.R. and Bansal, A.** (2022). RIS-assisted SSK Modulation: Reflection phase modulation and performance analysis, *IEEE Commun. Lett.*, *26*(5), 1012–1016.

[77] **Dash, S.P.**, **Mallik, R.K. and Pandey, N.** (2022). Performance analysis of an index modulation-based receive diversity RIS-assisted wireless communication system, *IEEE Commun. Lett.*, *26*(4), 768–772.

[78] **Guo, S.**, **Lv, S.**, **Zhang, H.**, **Ye, J. and Zhang, P.** (2020). Reflecting modulation, *IEEE J. Sel. Areas Commun.*, *38*(11), 2548–2561.

[79] **Lin, S.**, **Zheng, B.**, **Alexandropoulos, G.C.**, **Wen, M.**, **Di Renzo, M. and Chen, F.** (2020). Reconfigurable intelligent surfaces with reflection pattern modulation: Beamforming design and performance analysis, *IEEE Trans. Wireless Commun.*, *20*(2), 741–754.

[80] **Hussein, Y.**, **Assaad, M. and Sari, H.** (2021). Reconfigurable intelligent surface index modulation with signature constellations, *Proc. IEEE Wireless Commun. Netw. Conf. (WCNC)*, Nanjing, China, pp.1–7.

[81] **Li, Q.**, **Wen, M. and Di Renzo, M.** (2021). Single-RF MIMO: From spatial modulation to metasurface-based modulation, *IEEE Wireless Commun.*, *28*(4), 88–95.

[82] **Lin, S.**, **Chen, F.**, **Wen, M.**, **Feng, Y. and Di Renzo, M.** (2022). Reconfigurable intelligent surface-aided quadrature reflection modulation for simultaneous passive beamforming and information transfer, *IEEE Trans. Wireless Commun.*, *21*(3), 1469–1481.

[83] **Zhang, Z.**, **Dai, L.**, **Chen, X.**, **Liu, C.**, **Yang, F.**, **Schober, R. and Poor, H.V.** (2021). Active RIS vs. passive RIS: Which will prevail in 6G?, *arXiv preprint arXiv:2103.15154*.

[84] **Long, R.**, **Liang, Y.C.**, **Pei, Y. and Larsson, E.G.** (2021). Active reconfigurable intelligent surface aided wireless communications, *IEEE Trans. Wireless Commun.*, *20*(8), 4962–4975.

[85] **Basar, E. and Poor, H.V.** (2021). Present and future of reconfigurable intelligent surface-empowered communications, *IEEE Signal Process. Mag.*, *38*(6), 146–152.

[86] **Nguyen, N.T.**, **Vu, D.**, **Lee, K. and Juntti, M.** (2022). Hybrid relay-reflecting intelligent surface-assisted wireless communications, *IEEE Trans. Veh. Technol.*, *71*(6), 6228–6244.

[87] **Gao, Y.**, **Wu, Q.**, **Zhang, G.**, **Chen, W.**, **Ng, D.W.K. and Di Renzo, M.** (2022). Beamforming optimization for active intelligent reflecting surface-aided SWIPT, *arXiv preprint arXiv:2203.16093*.

[88] **Nguyen, N.T.**, **Nguyen, V.D.**, **Wu, Q.**, **Tölli, A.**, **Chatzinotas, S. and Juntti, M.** (2022). Hybrid active-passive reconfigurable intelligent surface-assisted multi-user MISO systems, *IEEE 23rd Inter. Workshop on Signal Process. Advances in Wireless Commun. (SPAWC)*, pp.1–5.

[89] **Series, M.** (2009). Guidelines for evaluation of radio interface technologies for IMT-Advanced, **Technical Report**, Report ITU-R M.2135-1.

[90] **Basar, E.** (2019). Media-based modulation for future wireless systems: A tutorial, *IEEE Wireless Commun.*, *26*(5), 160–166.

[91] **Jin, G.**, **Li, M.**, **Liu, D. and Zeng, G.** (2018). A simple planar pattern-reconfigurable antenna based on arc dipoles, *IEEE Antennas and Wireless Propag. Lett.*, *17*(9), 1664–1668.

[92] **Rohatgi, A.** *WebPlotDigitizer*, `http://www.https://apps.automeris.io/wpd/`.

[93] **Naresh, Y. and Chockalingam, A.** (2016). On media-based modulation using RF mirrors, *IEEE Trans. Veh. Technol.*, *66*(6), 4967–4983.

[94] **Basar, E.**, **Di Renzo, M.**, **De Rosny, J.**, **Debbah, M.**, **Alouini, M.S. and Zhang, R.** (2019). Wireless communications through reconfigurable intelligent surfaces, *IEEE Access*, *7*, 116753–116773.

[95] **Basar, E.** (2019). Transmission through large intelligent surfaces: A new frontier in wireless communications, *IEEE European Conf. Netw. and Commun. (EuCNC)*, pp.112–117.

[96] **Yigit, Z.**, **Basar, E. and Altunbas, I.** (2020). Low complexity adaptation for reconfigurable intelligent surface-based MIMO systems, *IEEE Commun. Lett.*, *24*(12), 2946–2950.

[97] **Mesleh, R. and Alhassi, A.** (2018). *Space modulation techniques*, volume288, Wiley Online Library.

[98] **Narasimhan, T.L. and Chockalingam, A.** (2015). On the capacity and performance of generalized spatial modulation, *IEEE Commun. Lett.*, *20*(2), 252–255.

[99] **Jafarkhani, H.** (2005). *Space-time coding: Theory and practice*, Cambridge University Press.

[100] **Mesleh, R.**, **Hiari, O.**, **Younis, A. and Alouneh, S.** (2017). Transmitter design and hardware considerations for different space modulation techniques, *IEEE Trans. Wireless Commun.*, *16*(11), 7512–7522.

[101] **Paulraj, A.**, **Nabar, R. and Gore, D.** (2003). *Introduction to space-time wireless communications*, Cambridge University Press.

[102] **Simon, M.K. and Alouini, M.S.** (2005). *Digital communication over fading channels*, John Wiley & Sons.

[103] **Turin, G.L.** (1960). The characteristic function of Hermitian quadratic forms in complex normal variables, *Biometrika*, *47*(1/2), 199–201.

[104] **Herath, S.P.**, **Tran, N.H. and Le-Ngoc, T.** (2012). Rotated multi-D constellations in Rayleigh fading: Mutual information improvement and pragmatic approach for near-capacity performance in high-rate regions, *IEEE Trans. Commun.*, *60*(12), 3694–3704.

[105] **Basar, E.**, **Aygolu, U.**, **Panayirci, E. and Poor, H.V.** (2011). Space-time block coded spatial modulation, *IEEE Trans. Commun.*, *59*(3), 823–832.

[106] **Yigit, Z. and Basar, E.** (2017). Space-time quadrature spatial modulation, *Proc. IEEE 5th Int. Black Sea Conf. Commun. Netw. (BlackSeaCom)*, pp.1–5.

[107] **Phan-Huy, D.T.**, **Kokar, Y.**, **Rachedi, K.**, **Pajusco, P.**, **Mokh, A.**, **Magounaki, T.**, **Masood, R.**, **Buey, C.**, **Ratajczak, P.**, **Malhouroux-Gaffet, N.** *et al.* (2019). Single-carrier spatial modulation for the internet of things: Design and performance evaluation by using real compact and reconfigurable antennas, *IEEE Access*, *7*, 18978–18993.

[108] **Moon, T.K. and Stirling, W.C.** (2000). *Mathematical methods and algorithms for signal processing*, 621.39: 51 MON, Prentice Hall, New Jersey.

[109] **Hou, T.**, **Liu, Y.**, **Song, Z.**, **Sun, X.**, **Chen, Y. and Hanzo, L.** (2019). MIMO assisted networks relying on large intelligent surfaces: A stochastic geometry model, *arXiv preprint arXiv:1910.00959*.

[110] **Schroeder, R.**, **He, J. and Juntti, M.** (2021). Passive RIS vs. hybrid RIS: A comparative study on channel estimation, *Proc. IEEE 93rd Veh. Technol. Conf. (VTC2021-Spring)*, Helsinki, Finland, pp.1–7.

[111] **Karasik, R.**, **Simeone, O.**, **Di Renzo, M. and Shitz, S.S.** (2021). Adaptive coding and channel shaping through reconfigurable intelligent surfaces: An information-theoretic analysis, *IEEE Trans. Commun.*, *69*(11), 7320–7334.

[112] **Yang, H.**, **Chen, X.**, **Yang, F.**, **Xu, S.**, **Cao, X.**, **Li, M. and Gao, J.** (2016). Design of resistor-loaded reflectarray elements for both amplitude and phase control, *IEEE Antennas Wireless Propag. Lett.*, *16*, 1159–1162.

[113] **Primak, S.**, **Kontorovich, V. and Lyandres, V.** (2005). *Stochastic methods and their applications to communications: Stochastic differential equations approach*, West Sussex.

[114] **Proakis, J.G.** (2005). *Digital communications*, McGrawHill, New York, 5th edition.

[115] **An, Z.**, **Wang, J.**, **Wang, J.**, **Huang, S. and Song, J.** (2014). Mutual information analysis on spatial modulation multiple antenna system, *IEEE Trans. Commun.*, *63*(3), 826–843.

[116] **Björnson, E. and Sanguinetti, L.** (2020). Rayleigh fading modeling and channel hardening for reconfigurable intelligent surfaces, *IEEE Wireless Commun. Lett.*, *10*(4), 830–834.

[117] **Van Chien, T.**, **Ngo, H.Q.**, **Chatzinotas, S.**, **Di Renzo, M. and Ottersten, B.** (2021). Reconfigurable intelligent surface-assisted cell-free massive MIMO systems over spatially-correlated channels, *IEEE Trans. Wireless Commun.*

[118] **Sohrabi, F. and Yu, W.** (2016). Hybrid digital and analog beamforming design for large-scale antenna arrays, *IEEE J. Sel. Topics Signal Process.*, *10*(3), 501–513.

[119] **Luo, S.**, **Yang, P.**, **Che, Y.**, **Yang, K.**, **Wu, K.**, **Teh, K.C. and Li, S.** (2021). Spatial modulation for RIS-assisted uplink communication: Joint power

allocation and passive beamforming design, *IEEE Trans. Commun.*, *69*(10), 7017–7031.

[120] **Zhang, R.**, **Yang, L.L. and Hanzo, L.** (2013). Generalised pre-coding aided spatial modulation, *IEEE Trans. Wireless Commun.*, *12*(11), 5434–5443.

[121] **Grant, M. and Boyd, S.**, (2008). Graph implementations for nonsmooth convex programs, **V. Blondel**, **S. Boyd and H. Kimura**, editors, Recent Advances in Learning and Control, Lecture Notes in Control and Information Sciences, Springer-Verlag Limited, pp.95–110, `http://stanford.edu/~boyd/graph_dcp.html`.

[122] **Spencer, Q.H.**, **Swindlehurst, A.L. and Haardt, M.** (2004). Zero-forcing methods for downlink spatial multiplexing in multiuser MIMO channels, *IEEE Trans. Signal Process.*, *52*(2), 461–471.

[123] **Khoshafa, M.H.**, **Ngatched, T.M.**, **Ahmed, M.H. and Ndjiongue, A.R.** (2021). Active reconfigurable intelligent surfaces-aided wireless communication system, *IEEE Comm. Lett.*, *25*(11), 3699–3703.

[124] **Yan, W.**, **Yuan, X.**, **He, Z.Q. and Kuai, X.** (2020). Passive beamforming and information transfer design for reconfigurable intelligent surfaces aided multiuser MIMO systems, *IEEE J. Sel. Areas Commun.*, *38*(8), 1793–1808.

[125] **El Ayach, O.**, **Rajagopal, S.**, **Abu-Surra, S.**, **Pi, Z. and Heath, R.W.** (2014). Spatially sparse precoding in millimeter wave MIMO systems, *IEEE Trans. Wireless Commun.*, *13*(3), 1499–1513.

[126] **Zhang, X.** (2017). *Matrix analysis and applications*, Cambridge University Press.

[127] **Stavridis, A.**, **Sinanovic, S.**, **Di Renzo, M. and Haas, H.** (2012). Transmit precoding for receive spatial modulation using imperfect channel knowledge, *IEEE 75th Veh. Technol. Conf. (VTC Spring)*, pp.1–5.

[128] **Luo, Z.Q.**, **Ma, W.K.**, **So, A.M.C.**, **Ye, Y. and Zhang, S.** (2010). Semidefinite relaxation of quadratic optimization problems, *IEEE Signal Process. Mag.*, *27*(3), 20–34.

[129] **Wu, M.**, **Lei, X.**, **Zhou, X.**, **Xiao, Y.**, **Tang, X. and Hu, R.Q.** (2021). Reconfigurable intelligent surface assisted spatial modulation for symbiotic radio, *IEEE Trans. Veh. Technol.*, *70*(12), 12918–12931.

CURRICULUM VITAE

Name Surname: Zehra YİĞİT

EDUCATION:

B.Sc.: 2013, Gaziantep University, Engineering Faculty, Department of Electrical and Electronics Engineering.

M.Sc.: 2017, Istanbul Technical University, Graduate School of Science and Technology, Telecommunication Engineering Programme.

PROFESSIONAL EXPERIENCE AND REWARDS:

2015: - - Research Assistant at Istanbul Technical University, Department of Electronics and Communication Engineering.

PUBLICATIONS AND PRESENTATIONS ON THE THESIS:

Journals

1. **Yigit, Z.**, Basar, E., 2019. Space-time media-based modulation , *IEEE Transactions on Signal Processing*, 67(9), 2389–2398.
2. **Yigit, Z.**, Basar, E., Altunbas, I., 2020. Low complexity adaptation for reconfigurable intelligent surface-based MIMO systems. *IEEE Communication Letters* 24(12), 2946–2950.
3. **Yigit, Z.**, Basar, E., Wen, M., Altunbas, I. 2022. Hybrid reflection modulation. *IEEE Transactions on Wireless Communications* (accepted for publication)
4. **Yigit, Z.**, Basar, E., Altunbas, I., 2022. Over-the-air beamforming with reconfigurable intelligent surfaces. *Frontiers in Communications and Networks* (accepted for publication)

Conference Proceedings

1. **Yigit, Z.**, Basar, E., Altunbas, I., 2019. Circular space-time block code design for ultra-reliable index modulation schemes. *IEEE 30th Annual Inter. Symp. Personal, Indoor and Mobile Radio Commun. (PIMRC)*.
2. **Yigit, Z.**, Basar, E., Altunbas, I., 2021. SimMBM channel simulator for media-based modulation systems modulation schemes. *IEEE 30th Annual Inter. Symp. Personal, Indoor and Mobile Radio Commun. (PIMRC)*.

OTHER PUBLICATIONS, PRESENTATIONS AND PATENTS:

Journals

1. **Yigit, Z.**, Basar, E., Mesleh, R., 2018. Trellis coded quadrature spatial modulation. *Physical Communications*, 29, 147–155.
2. **Yigit, Z.**, Basar, E., 2017. Low-complexity detection of quadrature spatial modulation. *Electronics Letters*, 52(20), 1729–1731.
3. **Yigit, Z.**, Basar, E., 2017. Two-way quadrature spatial modulation. *EMO Bilimsel Dergi*, 7(14), 21–27.

Conference Proceedings

1. Dogukan, A. T., **Yigit, Z.**, Basar, E., 2020. Multidimensional media-based modulation. *IEEE Latin-American Conference on Communications (LATINCOM)*.
2. **Yigit, Z.**, Basar, E., 2017. Space-time quadrature spatial modulation. *IEEE Inter. Black Sea Conf. Commun. Netw. (BlackSeaCom)*
3. **Yigit, Z.**, Basar, E., 2016. Double spatial modulation: A high-rate index modulation scheme for MIMO systems. *IEEE Inter. Symp. Wireless Commun. Syst. (ISWCS)*
4. **Yigit, Z.**, Basar, E., 2017. Quadrature spatial modulation for large scale MIMO systems. *IEEE 25th Signal Process. Commun. Appl. Conf. (SIU)* (National conference)
5. **Yigit, Z.**, Basar, E., 2016. High-rate generalized spatial modulation. *IEEE 24th Signal Process. Commun. Appl. Conf. (SIU)* (National conference)